

**Measurement of the top quark pair differential cross-section at high top
quark transverse momentum in $\sqrt{s} = 8$ TeV proton-proton collision data
collected with the ATLAS detector at the LHC**

by

Ana Krasimirova Ovcharova

A dissertation submitted in partial satisfaction of the
requirements for the degree of
Doctor of Philosophy

in

Physics

in the

GRADUATE DIVISION
of the
UNIVERSITY OF CALIFORNIA, BERKELEY

Committee in charge:
Professor Marjorie Shapiro, Chair
Professor Robert Jacobsen
Professor Karl Van Bibber

Fall 2014

**Measurement of the top quark pair differential cross-section at high top
quark transverse momentum in $\sqrt{s} = 8$ TeV proton-proton collision data
collected with the ATLAS detector at the LHC**

Copyright 2014
by
Ana Krasimirova Ovcharova

Abstract

Measurement of the top quark pair differential cross-section at high top quark transverse momentum in $\sqrt{s} = 8$ TeV proton-proton collision data collected with the ATLAS detector at the LHC

by

Ana Krasimirova Ovcharova
Doctor of Philosophy in Physics
University of California, Berkeley
Professor Marjorie Shapiro, Chair

This dissertation presents the first measurement of the top quark pair differential cross-section as a function of the hadronic top candidate transverse momentum that uses boosted top quark identification techniques. This allows to extend the measurement into the TeV range, with the cross-section reported for top candidate transverse momentum between 300 GeV and 1.2 TeV. The measurement is performed using events reconstructed in the lepton+jets channel in 20.3 fb^{-1} of $\sqrt{s} = 8$ TeV proton-proton collision data collected by the ATLAS experiment. Previous measurements have reported the cross-section as a function of the top quark kinematics. To allow for a robust top candidate definition, independent of assumptions required to isolate the kinematics of individual partons, the cross-section presented here is reported at the stable particle level. The cross-section is reported within a fiducial region closely following the detector-level event selection to minimize uncertainties associated with extrapolations beyond the detector acceptance. To illustrate the evolution of the uncertainties associated with extrapolating the particle level results to the usual top parton definition, the results are also presented within the full phase-space at the parton level.

Contents

List of Figures	iii
List of Tables	vii
1 Introduction	1
2 Theory	3
2.1 Predictions for hadron collider processes	3
2.1.1 Concepts in Quantum Chromodynamics	5
2.1.2 Hadron collision simulation	8
2.2 Motivation	14
2.2.1 Open questions	15
2.2.2 Proposed solutions	15
2.2.3 Role of the top quark	16
3 Analysis strategy	20
4 The ATLAS Experiment	24
4.1 Large Hadron Collider	24
4.2 LHC Run I proton-proton collision dataset	25
4.3 ATLAS Detector	27
4.3.1 Inner Detector (ID)	29
4.3.2 Calorimeters	32
4.3.3 Muon System (MS)	34
4.3.4 Trigger System	36
5 Object definition and calibration	38
5.1 Track and vertex reconstruction	38
5.2 Muons	39
5.3 Electrons	41
5.4 Small- R jets	42
5.5 Large- R jets	44
5.6 B-tagging	46

5.7	Missing energy	47
6	Event selection	49
7	Detector-level modeling	54
7.1	Data-driven background predictions	54
7.1.1	$W+jets$	54
7.1.2	Multijet	56
7.2	MC-based predictions	57
7.3	Systematic uncertainties at detector level	58
7.4	Comparison of data to prediction	59
8	Unfolding strategy	65
8.1	Unfolding procedure	66
8.2	Bin optimization	67
8.3	Validation	68
9	Unfolding to particle level	70
9.1	Particle level objects	70
9.2	Fiducial region definition	71
9.3	Electron and muon channel combination	72
9.4	Unfolding ingredients	72
9.5	Uncertainty propagation	76
9.5.1	Experimental systematics	76
9.5.2	Signal modeling	77
9.5.3	Data and MC statistical uncertainties	79
9.6	Results	79
9.7	Cross-check	81
9.8	Discussion	84
10	Unfolding to parton level	86
10.1	Parton level phase-space	86
10.2	Unfolding method	86
10.3	Uncertainty propagation	87
10.4	Results	89
11	Conclusion	93
	Bibliography	94
	A Electron-jet overlap removal	99
	B Channel-to-channel comparison	103

List of Figures

2.1	Illustration of a top pair event generated using the Sherpa event generator. Red lines indicate the hard scatter, blue - the parton shower, green - the hadronization, yellow - the QED final state radiation and purple the underlying event [5].	4
2.2	Running of the strong coupling constant from the PDG QCD review [8].	6
2.3	Proton PDFs at $Q^2 = 10 \text{ GeV}^2$ (left) and $Q^2 = 10^4 \text{ GeV}^2$ (right) according to the NNPDF collaboration [8].	9
2.4	The same event clustered with the k_t (left) and the anti- k_t (right) algorithms [21].	12
2.5	Illustration of the jet trimming algorithm [23].	13
2.6	Illustration of the effect of jet trimming on light jets and top jets [23].	14
2.7	Gluino (left) and stop (right) pair production Feynman diagrams [25].	17
2.8	Dominant leading order top pair production Feynman diagrams at the LHC [26].	18
2.9	Effect on the gluon PDF from including top cross-section measurements in the global PDF fit by the NNPDF collaboration [27].	18
3.1	Illustrations of (a) the resolved topology and (b) the expected distance between the W boson and the b -quark as a function of top transverse momentum.	21
3.2	The boosted topology	22
3.3	Particle and parton level illustrated using the Sherpa generated event from Chapter 2.	23
4.1	CERN accelerator complex	25
4.2	Total integrated luminosity of the Run I dataset	26
4.3	Mean number of interactions per crossing in the 2012 LHC run	27
4.4	Overview of ATLAS	28
4.5	Overview of the Inner Detector	29
4.6	Inner Detector barrel and endcap components	31
4.7	Overview of the Calorimeter system	32
4.8	EM barrel module	33

4.9	Tile barrel module	33
4.10	Arrangement of calorimeters in one of the two endcap cryotats.	35
4.11	Overview of the Muon System	37
5.1	Muon trigger efficiency [34].	40
5.2	Electron reconstruction and identification efficiency [35].	41
5.3	Combined efficiency of the 24 GeV and 60 GeV electron triggers [38].	42
5.4	Relative small- R JES uncertainty [39].	44
5.5	Large- R JES uncertainty [23]	45
5.6	Large- R JMS uncertainty [23]	45
5.7	B-tagging efficiency [42].	48
7.1	Single-top production in the t -channel (1^{st} and 2^{nd} diagram from the left), the s -channel (3^{rd} diagram) and the Wt -channel (right-most diagram) [26].	57
7.2	Distributions of the p_T of the selected lepton, the missing transverse energy and the W transverse mass.	61
7.3	Distributions of the mass and the first splitting scale of the top-jet candidate.	62
7.4	Distributions of the η and the p_T of the hadronic top-jet candidate.	63
7.5	Distributions of η , p_T and multiplicity of the b -tagged small- R jets.	64
8.1	Results of (a) the closure test (unfolding the PowHEG+PYTHIA reconstructed spectrum with its own response and comparing to truth), and (b) the stress test (unfolding a reweighted PowHEG+PYTHIA reconstructed spectrum with the nominal response and comparing to the reweighted truth).	69
9.1	Acceptance correction, accounting for events that pass the detector level selection, but do not belong to the particle-level fiducial region. Shown separately for $e+jets$ (a) and $\mu+jets$ (b) events and combined over electrons and muons (c).	73
9.2	Detector response for the combined $\ell+jets$ sample. The z -axis shows the number of events in the bin in the nominal $t\bar{t}$ MC sample.	74
9.3	PowHEG+PYTHIA migration from particle to reconstructed level (normalized to number of particle level events in each column). Shown separately for $e+jets$ (a) and $\mu+jets$ (b) events and combined over electrons and muons (c).	75
9.4	Efficiency for $t\bar{t}$ events inside the fiducial region to pass the reconstructed-level event selections as a function of the particle top p_T . Shown separately for $e+jets$ (a) and $\mu+jets$ (b) events and combined over electrons and muons (c).	76
9.5	Impact of the signal model uncertainties on the particle-level spectrum.	78

9.6	Results of the statistical uncertainty pseudo experiments.	80
9.7	Statistical bin-to-bin correlations of the particle level result arising from the use of regularized unfolding.	80
9.8	Final result for the differential cross-section as a function of the hadronic particle top-jet candidate p_T in $l+\text{jets}$ decay mode.	81
9.9	Systematic uncertainties on the particle top-jet spectrum. The yellow band shows the total symmetrized uncertainty on the cross-section. .	82
9.10	The differential cross-section in $l+\text{jets } t\bar{t}$ decay mode based on individual channel data.	83
9.11	Ratio between the cross-sections measured based on individual channel data. Error bars show data statistical uncertainty, lepton scale factor and resolution as well as MC statistical uncertainties. The uncertainties related to lepton reconstruction are correlated between bins. . . .	83
9.12	Effect of electroweak corrections and data to MC agreement.	84
9.13	Data-to-MC agreement for the alternate HERAPDF set and different value of the PowHEG <code>hdamp</code> parameter.	85
10.1	(a) Acceptance correction factors, i.e. number of $t\bar{t}$ events passing both particle and parton-level cuts divided the number of events passing only the particle-level cuts as a function of top p_T . (b) Efficiency for $t\bar{t}$ events inside the fiducial region to pass the particle-level event selections as a function of the parton top p_T . (c) PowHEG+PYTHIA migration from parton to particle level (normalized to number of parton level events in each column)	88
10.2	(a) Impact of the signal generator uncertainties on the parton spectrum. (b) Statistical uncertainties determined from pseudo experiments.	89
10.3	Statistical bin-to-bin correlations of the parton level result arising from the combination of limited data statistics and the use of regularized unfolding.	90
10.4	Final result for the differential cross-section as a function of the hadronically decaying top quark p_T	91
10.5	Systematic uncertainties on the unfolded spectrum at parton level. . .	92
A.1	Comparison between the two versions of electron-jet overlap removal in terms of efficiency and acceptance derived with respect to a particle-level with <i>no</i> overlap removal	100
A.2	Comparison between data and simulation for events that are not affected by the subtraction procedure (left) and these that are (right), for the distributions of the distance between the lepton and leptonic-side b -jet candidate (top), the distance between the selected large- R jet and leptonic-side b -jet candidate (middle) and the selected large- R jet p_T (bottom). An overall normalization factor of 0.84 is used in both cases.	101

A.3 (a) p_T distribution for the affected jets and (b) relative change in the reconstructed top p_T spectrum corresponding to e -subtracted jet p_T variations of 2%, 5% and 10%.	101
B.1 Ratios between the e +jets and μ +jets reconstructed-level distribution for both data and MC for the large- R jet p_T (a) and η (b), and the lepton p_T (c). Error bars show only statistical uncertainty.	104

List of Tables

6.1	Reconstructed and particle-level selections	49
6.2	Percentage of events retained at various stages of the event selection. The values are based on a test sample of 15,000 semi-leptonic $t\bar{t}$ events.	53
7.1	Impact of the different uncertainty sources on the total prediction in bins of top-jet transverse momentum (evaluated for the sum of the two decay channels).	59
7.2	Observed and expected number of events in the signal e +jets and μ +jets samples.	59
9.1	Cross-section uncertainties by category as a function of the particle top-jet candidate p_T in l +jets decay mode.	77
9.2	Cross-section values as a function of the hadronically decaying top p_T in l +jets decay mode.	82
10.1	Cross-section uncertainties by category as a function of the top quark p_T	90
10.2	Cross-section values as a function of the hadronically decaying top quark p_T in l +jets decay mode.	91
A.1	The energy of the e -subtracted is varied simultaneously between data and MC by $\pm 5\%$ and $\pm 10\%$ and the data/MC agreement re-evaluated. Only events affected by the subtraction procedure are considered. . .	102

Acknowledgments

Most of all, I am very grateful to have had an excellent advisor. Marjorie Shapiro gave me advice when I needed it and let me freely explore the wonderful and terrible world of doing particle physics in a huge collaboration when I wanted to. Her presence and guidance was always just right, neither too forceful nor too detached. I thank her for choosing projects that ensured I got a broad experience in the many aspects involved in such a grand scale experiment, and at the same time allowed me to delve into subjects I found myself drawn to. I really appreciated her enthusiasm about doing physics and her readiness to jump into a problem and resolve it without unnecessary fuss. I can only hope that some of this blend of optimism, curiosity and determination rubbed off on me!

The idea to measure the differential top quark pair cross-section in the boosted regime came from Jean-Francois Arguin while walking to lunch at R1. I am glad I went to lunch that day! It has been a great pleasure doing this analysis with him. Working alongside JF I had the opportunity to learn not only about doing a physics analysis, but also about fostering a productive collaboration and communicating effectively. I thank him also for all his advice in navigating my path forward beyond this analysis.

Working on this analysis has also given me the chance to tap into the vast knowledge in the ATLAS Top Working Group. The conveners, Tancredi Carli, Alison Lister, Mark Owen, William Bell and Francesco Spano, have all provided much valuable input and their comments on how to improve this analysis were always greatly appreciated. I would like to especially thank Tancredi for his constant support and guidance through the highs and lows of bringing this measurement to fruition. This analysis has also greatly benefited from the work done by the ATLAS top pair resonance search group, who generously shared their work on perfecting the event selection and estimating the data-driven backgrounds. I would like to thank Jiahang Zhong and Samuel Calvet for their help in incorporating these results into the measurement.

Looking further back in my days of working on the Pixel detector, I am filled with great memories of the days of learning to navigate the DAQ software with Mark Cooke and trying to push the limits of both Pixel data-taking efficiency and sleep deprivation with Kerstin Lantzsch and Jens Dopke. It was a lot of fun!

Recounting all the people I have appreciated working with and learning from would take longer than it took to write this thesis. Being a part of the LBL ATLAS group has been an amazing experience. I am grateful for having had the opportunity to observe some of the most talented people I know do the kind of work I hope to be doing myself, following their example. I want to extend a special thanks to Weiming Yao, who guided me through my first research experience as an undergraduate working on the tracker alignment and continued to provide insightful advice all throughout the measurement described in this thesis. I admire his uncanny ability to tell if a plot is wrong right away and his seemingly endless patience. I am especially grateful to have shared time at LBL with Mike Hance and Zach Marshall, both of whom I've

interrupted more times than I can recall with questions ranging from software and physics to career advice. I was never turned back and always left their offices knowing more than I did when I came in.

I will miss all of you greatly.

Chapter 1

Introduction

The Standard Model (SM), the theory describing the interactions between the fundamental particles, has been remarkably successful in providing predictions consistent with the abundant experimental results produced by the Large Hadron Collider (LHC) experiments. With the discovery of the Higgs boson, all particles predicted by the SM have been observed and the model is theoretically viable up to, but not including, energies where gravitational effects become important, i.e. the Planck scale. There are however multiple reasons to believe that new phenomena beyond the domain of the SM should be observed significantly below these energies, in particular at the TeV scale, accessible at the LHC. For example, the existence of dark matter and neutrino oscillations cannot be explained by the SM. Similarly, the matter-anti-matter asymmetry observed in our Universe, the values of the particle masses and the large disparity between the strengths of the fundamental forces remain as mysteries.

A plethora of theoretical models for new physics have been proposed to try to address these issues, including proposals for the addition of new space-time symmetries or dimensions, compositeness as well as entire hidden sectors of additional particles and forces beyond the SM [1]. Unfortunately, despite the very successful first run of the LHC, none of these new particles or phenomena have been observed. It is increasingly likely that new physics may not come with striking signatures, but rather may need to be teased out from the midst of large backgrounds by improving upon the precision of our measurements. Many of the proposed extensions of the SM would produce events that have rich final states including leptons, multiple jets and missing energy. These are also the exact ingredients of top quark pair events, making top production an ubiquitous background for new physics searches. Therefore, it is crucial to understand the kinematics of top quark pair production and improve upon its modeling to allow a corresponding improvement in our searches. Fortunately, top production is abundant at the LHC, which has been referred to as a top quark factory, and indeed the 20 fb^{-1} of 8 TeV proton-proton collisions dataset collected in the LHC Run I should contain over 5 million top pairs. This abundance of data allows for an unprecedented level of precision in the measurements.

The top quark pair differential cross-section has previously been measured by both ATLAS [2] and CMS [3, 4]. However, the reach in top transverse momentum in these results is limited to 800 GeV and 400 GeV, respectively. To help improve the modeling of top production in the highly boosted regime relevant for new physics searches, the analysis described in this thesis aims to extend the top quark transverse momentum measurement into the TeV range with the help of boosted top identification techniques. The results are presented within a fiducial region closely following the detector acceptance in order to minimize uncertainties. The spectrum measured in data is also corrected to the top parton transverse momentum, exploring the evolution of uncertainties involved in the additional corrections and allowing future comparisons with analytic calculations of the top quark pair cross-section (only available at the parton level).

This thesis is structured as follows. Chapter 2 first reviews the basic concepts necessary to understand the modeling of hadron collisions in simulation and then outlines the motivation for measuring the top quark pair differential cross-section. Chapter 3 provides an overview of the analysis strategy employed to extend the cross-section measurement to high transverse momentum. Chapter 4 introduces the ATLAS experiment and the dataset analyzed here. Chapter 5 supplies the definitions of the reconstructed objects at detector level as well as their calibration and associated uncertainties. Chapter 6 introduces the event selection. Chapter 7 contains a brief description of the simulation-based and data-based predictions, a summary of the uncertainties affecting the reconstructed distributions and a comparison of the prediction to the data at the detector level. Chapter 8 introduces the unfolding procedure used to correct the data. This procedure is applied to obtain the particle-level cross-section in Chapter 9 and the parton-level cross-section in Chapter 10.

Chapter 2

Theory

This chapter reviews the basic concepts involved in making predictions for hadron collision processes and the motivation for studying top quarks in particular.

2.1 Predictions for hadron collider processes

Since hadronic collisions are described by Quantum Field Theory (QFT) it is often dangerous or entirely incorrect to talk about annihilating individual partons, discerning individual emissions and identifying when these emissions occurred. While keeping this caveat in mind, it is nevertheless useful to define a language in which hadron collisions can be described schematically. One such simplified picture of the anatomy of a proton-proton collision event is depicted in Figure 2.1. Two protons incoming from the left and the right are presented as a combination of individual quarks and gluons, which go on to split into more partons until eventually interacting. The *hard scatter*, shown in red, between two gluons results in a top pair; one top decays hadronically (left) and the other leptonically (right). This central process is accompanied by additional q/g emissions referred to as *parton shower*, shown in blue. Parton shower can come from the gluons before their interaction, *initial state radiation*, from the produced top quarks, *final state radiation* and also accompanies the final evolution of the q/g decay products into narrow sprays of lower energy partons, *jets*. The recombination of these parton showers into hadrons, *hadronization*, and the subsequent hadron decays are shown in green. Depending on whether each of these processes lies in the domain of perturbative or non-perturbative QFT, they can be treated by either analytical calculations or phenomenological models and then combined to form a complete cross-section prediction. This section provides an overview of the basic concepts involved in making predictions for hadron collider processes.

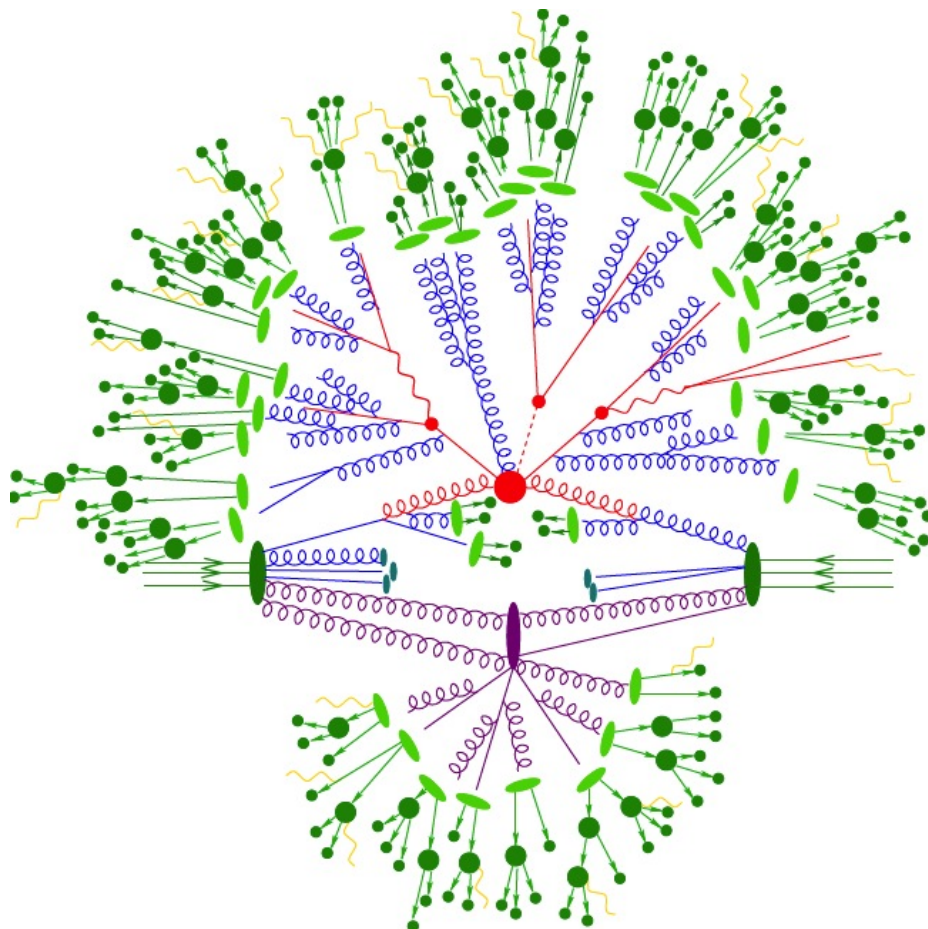


Figure 2.1: Illustration of a top pair event generated using the Sherpa event generator. Red lines indicate the hard scatter, blue - the parton shower, green - the hadronization, yellow - the QED final state radiation and purple the underlying event [5].

2.1.1 Concepts in Quantum Chromodynamics

Quantum Chromodynamics (QCD) is the non-Abelian gauge field theory that describes the strong interactions of quarks and gluons. To account for the three quark colors, QCD is governed by the SU(3) symmetry group. The Lagrangian density dictated by preserving local gauge invariance can be written as [6]:

$$\mathcal{L}_{QCD} = \bar{\psi}_i (i\gamma^\mu \partial_\mu \delta_{ij} - g_s \gamma^\mu t_{ij}^C \mathcal{A}_\mu^C - m \delta_{ij}) \psi_j - \frac{1}{4} G_{\mu\nu}^A G_A^{\mu\nu}, \quad (2.1)$$

$$\text{where } G_{\mu\nu}^A \equiv \partial_\mu \mathcal{A}_\nu^A - \partial_\nu \mathcal{A}_\mu^A - g_s f_{ABC} \mathcal{A}_\mu^B \mathcal{A}_\nu^C, \quad (2.2)$$

ψ is the quark field given by the fundamental representation of SU(3), \mathcal{A}_μ^B are the gluon fields, expressed in the adjoint representation, t^A are the generating matrices of SU(3) and f_{ABC} the group structure constants. The Feynman rules that can be deduced from this Lagrangian include gluon self-interaction in the form of both a 3-gluon and a 4-gluon vertex. The presence of these new vertices results in additional divergent structures in QCD that are not present in Quantum Electrodynamics and can ultimately be traced to the two defining features that allow QCD to account for experimental observations of the strong interaction, namely confinement and asymptotic freedom. The former refers to the fact that at low energy all quarks and gluons are confined to hadrons and the latter, that at high energy the quarks essentially behave as free particles.

The running coupling

In the framework of perturbative QCD, calculating cross-sections beyond the leading order requires the inclusion of diagrams containing loops of quarks and gluons. The resulting divergent integrals over the momenta of the particles in the loop are underconstrained by momentum conservation. The process of removing these divergences, referred to as regularization, involves recasting the calculation in $4-\epsilon$ dimensions. During this procedure one is forced to introduce a new parameter called the renormalization scale, μ_R , to keep all quantities with proper dimensions. Since any physical quantities must be independent of this arbitrary scale, any dependence on μ_R is re-absorbed in the fundamental parameters of the theory, e.g. the strong coupling constant $\alpha_s = g_s^2/4\pi$, a process referred to as renormalization. As a result the theory behaves differently depending on the scale at which it is probed. This effect is encoded in the renormalization group equation revealing the evolution of the coupling constant with μ_R . After some simplifications the coupling constant as a function of the momentum scale Q^2 can be written as [7]:

$$\alpha_s(Q^2) = \frac{\alpha_s(\mu_R^2)}{1 + \left(\frac{11N_C - 2n_f}{12\pi}\right) \alpha_s(\mu_R^2) \log \frac{Q^2}{\mu_R^2}}. \quad (2.3)$$

Here, N_C is the number of quark colors, and n_f is the number of quark flavors for quarks with masses below Q^2 . Since the value at a particular Q^2 is a fundamental parameter of the theory it cannot be predicted, instead it must be taken from experiment. At this point the above equation can be used to relate the values at two different momentum scales. Figure 2.2 shows several measurements overlayed with the functional form. The diverging value of the coupling at low Q^2 is responsible for confinement, while the coupling's decrease as a function of Q^2 , referred to as asymptotic freedom, explains why partons can be considered approximately free in high energy collisions.

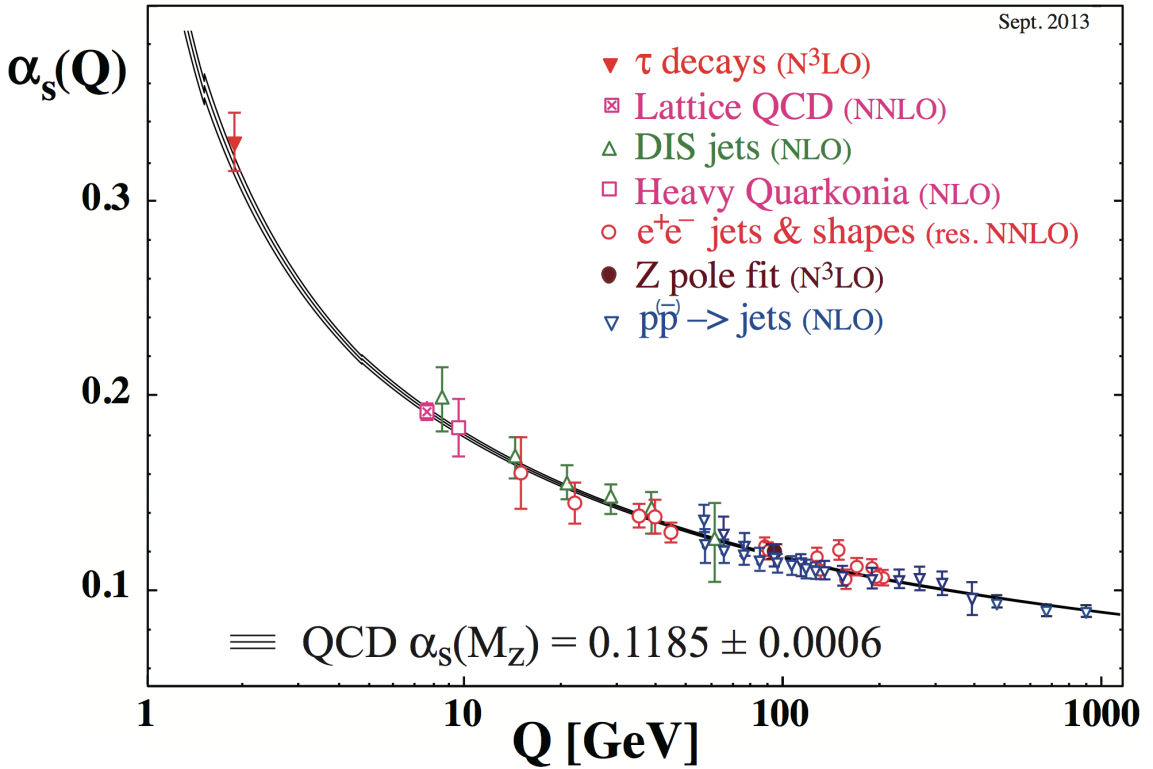


Figure 2.2: Running of the strong coupling constant from the PDG QCD review [8].

Factorization

One can then differentiate two domains of QCD, the low coupling regime governing high energy interactions where perturbative theoretical treatment is possible and the high-coupling, low-energy regime of non-perturbative QCD where quarks only exist in bound states and theoretical understanding is restricted to parametrization and phenomenological models (in some cases augmented with analytical understanding). Despite the non-perturbative components required for the understanding of an

event at the LHC, i.e. the colliding beams are composed of protons and the detectors measure hadrons, detailed predictions are available through the use of Monte Carlo simulation. This is possible due to the decoupling of perturbative and non-perturbative QCD referred to as *factorization*. Specifically, the cross-section for a particular process can be written as [9]:

$$\sigma_{AB}(pp \rightarrow X) = \int dx_a dx_b f_{a/A}(x_a, \mu_F^2) f_{b/B}(x_b, \mu_F^2) \times [\sigma_0 + \alpha_S(\mu_R^2) \sigma_1 + \dots] \quad (2.4)$$

The square brackets denote the expansion of the partonic cross-section in powers of the strong coupling, calculable in the framework of perturbative QCD. The function $f_{a/A}(x_a, \mu_F^2)$ denotes the probability to find a parton with momentum p_a in the proton with momentum p_A . Determination of these probability densities, referred to as Parton Distribution Functions (PDFs), lies in the domain of non-perturbative QCD, rendering them incalculable from first principles. The success of factorization is due to the fact that PDFs are approximately universal, i.e. they can be derived from data obtained in one experiment and then used in another. Since the PDFs depend on the momentum scale at which the proton is probed, analytical methods must be used to extrapolate them between different values of Q^2 . In performing this extrapolation a new arbitrary scale appears, the factorization scale, denoted as μ_F above. It results from using the same regularization and renormalization techniques as for the coupling, but this time to absorb infrared divergences into the PDFs. In this case, the divergences are associated with the soft and/or collinear emissions of one parton by another. Similarly to the case of the coupling constant running, analytic methods can be used to derive the renormalization group equations governing the evolution of the PDFs with μ_F , later referred to as the DGLAP equations. If both the PDFs and the partonic cross-section are calculated to all orders in perturbation theory, the dependence on μ_R and μ_F must cancel. In practice only few terms in the expansion can be calculated so in order to provide sensible predictions for experimental measurements, both μ_R and μ_F are chosen to correspond to the momentum transfer in the process under study. The theoretical uncertainty resulting from this assumption is estimated by variations of μ_R and μ_F within a factor of 2.

Intuitively, one can understand factorization by realizing that the perturbative and non-perturbative effects decouple since they occur on different time scales, each given by the inverse of the momentum scale characteristic of the interaction, $\tau \sim 1/Q$. The hard scatter momentum exchange is much larger than the one between the internal constituents of the proton. Therefore, on the time scale of the hard scatter the internal proton structure can be ignored. The only required input to the calculation is then the fraction of the proton momentum carried by the parton part-taking in the hard scatter.

2.1.2 Hadron collision simulation

The basic principles discussed above are employed in Monte Carlo simulation to allow comprehensive predictions for various kinematic distributions of the final state products in hadron collisions.

Parton Distribution Functions

Since the PDFs are not calculable from first principle, they are derived by fitting experimental data and then serve as input to MC calculations.

PDFs are generally extracted from data at a particular value of momentum transfer, characteristic of the experiment sourcing the data, and then extrapolated to other Q^2 values. In addition, different processes are generally most sensitive to a particular PDF over a particular range of proton momentum fraction values. For example, data from Deep Inelastic Scattering (DIS) experiments, where the probes are leptons, can be used to directly constrain only quark PDFs. Information about the gluon PDF can then be inferred indirectly since the DGLAP evolution of quarks leads to generating gluons and vice versa. Given this constraint, the best estimate of the PDFs are obtained by combining data from multiple experiments and processes into global fits. This is done by 3 PDF fitting collaborations: CTEQ [10], MSTW [11] and NNPDF [12]. The current knowledge of the proton PDFs according to NNPDF is shown in Figure 2.3. At large- x , most of the momentum is carried by the valence quarks and up-type quarks account for about twice the momentum as compared to down-quarks. Comparing the left and right subfigures confirms that as the probe becomes more energetic, a higher fraction of the proton momentum is found in the sea quarks and gluons.

Hard scatter

Description of the partonic cross-section lies in the domain of perturbative QCD and therefore lends itself to analytic calculations. Currently there exist Monte Carlo based programs that can perform these calculations automatically at both the leading order (LO) and next-to-leading order (NLO) in α_S . The leading order matrix element is always positive making it possible to implement the calculations via the Monte Carlo method. On the other hand, at NLO there are real and virtual divergent contributions, due to soft and collinear emissions, that must cancel in order to obtain finite results. This cancellation is guaranteed for inclusive observables like the total cross-section, but not so for observables like parton multiplicity [8]. In general, perturbative QCD can only provide sensible results for infrared and collinear (IRC) safe observables, which are observables insensitive to the addition of infinitely soft particles or the splitting of a particle into two collinear emissions.

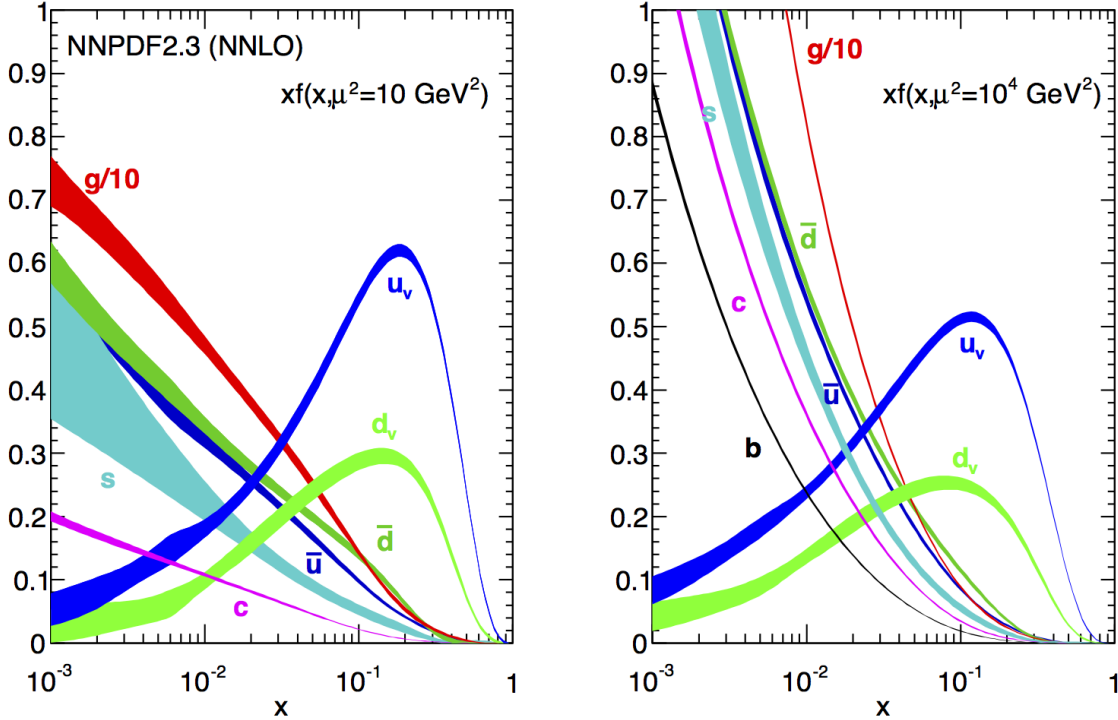


Figure 2.3: Proton PDFs at $Q^2 = 10 \text{ GeV}^2$ (left) and $Q^2 = 10^4 \text{ GeV}^2$ (right) according to the NNPDF collaboration [8].

Parton shower and hadronization

To account for the cross-section contributions from regions of phase space with soft and collinear emissions from both the initial state and final state partons, fixed order calculations must be augmented with parton shower (PS). The latter involve the successive calculation of the probability for a parton to evolve to a lower scale without emitting another parton above some cutoff. MC programs can employ this probability to produce parton splittings accordingly. Once a splitting has occurred the process repeats to find the next successive emission, and then again, until all final partons have energies of $\mathcal{O}(1 \text{ GeV})$. This version of parton showering is implemented in SHERPA [13] and PYTHIA [14] programs. A different approach is to instead calculate the probability of emitting a parton below some angle, i.e. the shower ordering variable is changed from the transverse momentum to the angle of the emission. This method is employed by the HERWIG [15] program.

Due to confinement, the partons produced by the showering programs cannot exist freely. The process of transforming them into hadrons is referred to as hadronization. It lies in the domain of non-perturbative QCD so it can only be described by phenomenological models. The two most widely used hadronization schemes are the Lund *string* model and the *cluster* model, implemented in PYTHIA and HERWIG,

respectively. The Lund string model describes the potential between a $q\bar{q}$ pairs as a string that gains energy from the quark and anti-quark as they move apart. Eventually, the energy stored in the string becomes comparable to hadron masses and it becomes energetically favorable for the string to break and create additional $q\bar{q}$ pairs. When a sufficiently small string fragment forms, it can be directly identified with a hadron, which is then further decayed to the observed stable particles. In the cluster model, first all gluons are split into $q\bar{q}$ pairs. Following, all quarks are combined into color-singlet clusters. If in this process a cluster becomes too heavy, i.e. above 3-4 GeV which would be the domain of a parton shower, the cluster is split. Eventually, the resulting low mass clusters are decayed to hadrons, which go on to produce the observed particles.

Merging fixed-order with parton shower

Matching fixed order calculations with parton shower requires special care since both may account for wide angle radiation, which would result in double counting. Special methods have been developed to ensure that any particular configuration of emissions is handled either exclusively by the parton shower or by the fixed order calculation. Mechanism to perform this matching are available for both LO and NLO generators.

An example of LO+PS combination is the MLM matching scheme [16] implemented in the ALPGEN [17] leading order multi-parton generator. In the MLM scheme events in which the showering produced additional hard wide angle emissions above some cut off transverse momentum scale are rejected and taken from the Matrix Element (ME) calculation. In other words, an event is only accepted if the number of hard well-separated showers is equal to the number of partons in the ME.

In the case of NLO+PS, double counting occurs because parton shower programs by themselves attempt to provide corrections that would approximate the effects of a true NLO calculation. There are two methods to avoid such double-counting MC@NLO [18] and POWHEG [19]. The former involves computing analytically what portion of the NLO result is already present in the parton shower approximation and then subtracting it from the shower before combining with the exact NLO combination. This approach requires calculations to be redone for each showering program as each of them uses different NLO approximations. The method was first implemented in the context of the HERWIG shower, but more recently MC@NLO+PYTHIA has also become available [20]. One disadvantage of the method is that it produces events with negative weight, which can be problematic in sparsely populated regions of phase space. In the POWHEG approach, the probability calculation for each successive step in the spreading of the shower is modified for the first emission such that it reaches exact NLO accuracy. Standard PS programs are then employed to shower the rest of the event employing a p_T veto, such that they do not produce an emission harder than the NLO leg from the previous step. This method can be used to obtain NLO+PS

accuracy using both PYTHIA and HERWIG showers. In contrast with MC@NLO, this method is that all events have positive weights.

Jets and jet substructure

As mentioned earlier, NLO calculations can only be performed for IRC safe observables. Perhaps the most important such observable is the *jet*¹. Ideally, a jet would correspond to the parton shower of one hard parton that initiated it. In reality, a jet may partially or fully contain the shower of multiple partons as well as additional radiation from the underlying event, which will be discussed more later. An IRC safe definition of a jet would allow the comparison of NLO calculations and experiment for non-inclusive measurements, such as the parton multiplicity within a fiducial region. Jets are generally built from the final stable particles in the generator record (green in Figure 2.1), charged particle tracks or calorimeter energy depositions. A jet definition specifies the recombination algorithm according to which the 4-vectors of all constituents in an event are systematically added using a distance metric until each one is associated with a jet. Both the ATLAS and CMS experiments at the LHC use the anti- k_t [21] jet algorithm as the default choice and an assortment of others in special cases. For this analysis both the anti- k_t and the k_t [22] jet algorithms, differing only by the choice of their distance metric, play a role.

To provide a context, consider the ATLAS coordinate system: the origin is at the center of the detector, which consists of concentric cylindrical layers around the beamline; the x-axis points to the center of the LHC ring, the y-axis points to the surface and the z-axis is set to form a right-handed coordinate system. The pseudorapidity η is then defined as $-\ln [\tan(\theta/2)]$, with θ being the polar angle.

The algorithm begins by defining the distances between two constituents i and j and between constituents i and the beam as:

$$d_{ij} = \min(p_{T,i}^{2k}, p_{T,j}^{2k}) \left(\frac{\Delta R_{ij}}{R_0} \right)^2 \quad (2.5)$$

$$d_{iB} = p_{T,i}^{2k} \quad (2.6)$$

Here, p_T denotes the constituent transverse momentum, $\Delta R_{ij} \equiv \sqrt{(\eta_i - \eta_j)^2 + (\phi_i - \phi_j)^2}$ and R_0 is a user defined distance which would approximately determine the size of the jet in the $\eta - \phi$ plane. The value of the exponent k is +1 for the k_t algorithm and -1 for anti- k_t . Given the distance metric and the set of constituents to be clustered into jets, the algorithm proceeds as follows:

- find the smallest d_{ij} and d_{iB}

¹Note that jet building algorithms were not always IRC safe, but with the increased availability of tools with NLO accuracy, the use of IRC safe jet definitions has become a necessity.

- if $d_{ij} < d_{iB}$, replace i and j by a new constituent formed by the 4-vector sum of i and j
- if $d_{ij} > d_{iB}$, declare i a jet and remove from the list of constituents

An illustration of the results of clustering with each of these algorithms is shown in Figure 2.4. The difference in the behavior can be understood by considering that in the case of k_t the metric is proportional to $p_{T,i}^2$, so a smaller d_{ij} would come from prioritizing the combination of lower momentum constituents first. Conversely, for anti- k_t , $d_{ij} \propto 1/p_{T,i}^2$, prioritizing the combination of high momentum constituents first. If the jet is formed, by taking the hardest constituents first and then sweeping neighboring soft radiation, as in anti- k_t , that means the jet axis will quickly stabilize after the first few combinations resulting in the circular jets seen in the figure. Circular jets have the advantage of being easier to calibrate and have better defined acceptance. Because of this feature, the anti- k_t algorithm is the default for both the ATLAS and CMS experiments at the LHC.

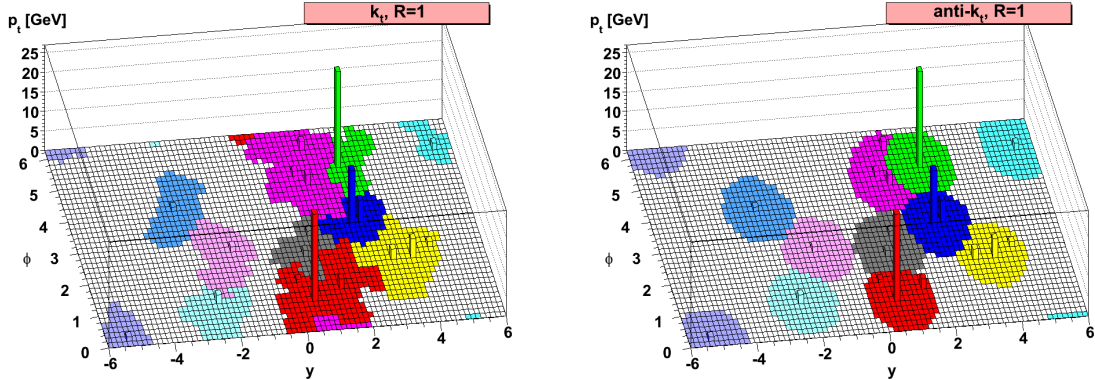


Figure 2.4: The same event clustered with the k_t (left) and the anti- k_t (right) algorithms [21].

The k_t algorithm on the other hand was built with the intention to trace backwards the parton shower evolution by combining together soft nearby constituents into harder and harder jet cores. This results in rather irregular jets, but because of the shower evolution information embedded in the clustering history of each jet, the k_t jet definition is crucial for studying jets containing the decay of heavy particles. The separation between the two decay products of a particle with transverse momentum p_T and mass m is approximately:

$$\Delta R(i, j) \sim \frac{2m}{p_T} \quad (2.7)$$

For example, for a Higgs decaying to $b\bar{b}$ with $p_{T,H} = 500$ GeV and $m_H = 125$ GeV, the distance between the two b -quarks would be ~ 0.5 . Then if the event is clustered

using jet radius $R_0 \geq 0.6$, the two b -quarks are likely to be reconstructed as a single jet. Looking at the energy distribution of this jet would reveal a two-prong structure. Conversely, a light quark jet or gluon would have only a single hard core. If this jet is built with the k_t algorithm, then the two hard energy deposits corresponding to the two quarks would have been the last two constituents to be merged. For a light jet, the last step in the clustering would be the merger of the hard core with a soft/wide angle piece of radiation. The distinction can be made quantitatively by calculating the first k_t splitting scale, which is related to the root of the distance metric in the last clustering step:

$$\sqrt{d_{12}} = \min(p_{T,1}, p_{T,2})\Delta R_{12} \quad (2.8)$$

Here, $p_{T,1}$ and $p_{T,2}$ are the transverse momenta of the last two constituents to be merged together in the formation of the jet. For jets containing the decay of a heavy particle $\sqrt{d_{12}}$ peak at about half its mass, while for light quark or gluon jets the values tend to be low, e.g. about 20 GeV for a jet with $p_T \sim 700$ GeV.

Jet grooming

In an effort to extract more information from jets, a variety of jet *grooming* algorithms have also been developed in the recent years. The goal is to selectively remove soft radiation from jets in order to highlight any potential substructure as well as remove contamination from radiation unrelated to the hard scatter. This analysis uses the jet *trimming* algorithm illustrated in Figure 2.5. First, the initial jet, in this case built with anti- k_t , is reclustered with the k_t algorithm with a significantly smaller radius R_{sub} . This allows for collimated energy deposits within the large jet to form *subjets*. Then, any subjets with transverse momentum below some fraction of the momentum of the original jet, defined as f_{cut} , are discarded. The remaining subjets when recombined form the *trimmed jet*.

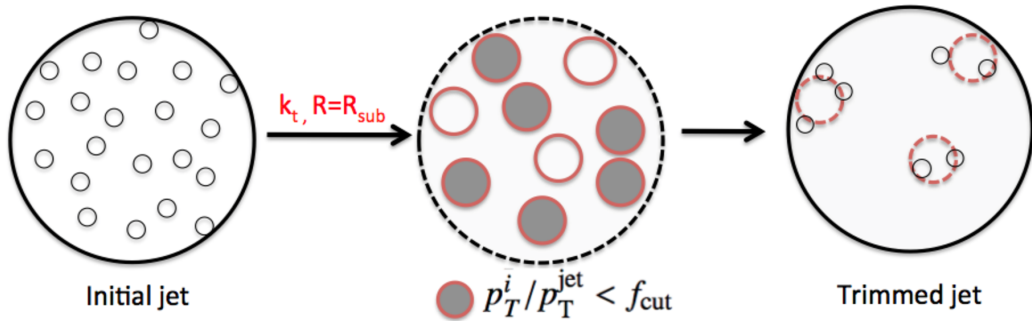


Figure 2.5: Illustration of the jet trimming algorithm [23].

This procedure can be used to enhance the discrimination between jets originating from a single light quark or gluon and jets containing the decay of a heavy particle. Since the former have a single hard core, many of the additional subjets formed by

the soft radiation in the periphery of the hard core would not pass the momentum fraction cut required to retain them. Conversely, the decay of a heavy particle would result in multiple hard subjets and therefore the jet would keep most of its energy after it has been trimmed. This effect is easily seen in the jet mass which is a result of the 4-vector combination of the massless constituents and therefore particularly sensitive to the angular separation of hard radiation in a jet. A comparison of the jet mass for light jets and jets containing the decay of a top, before and after trimming is shown in Figure 2.6. For the light jets shown in black, the mass distribution shifts by more than 50 GeV, while for top jets the mass remains stable. The small peak that appears to the left after trimming top jets is due to instances where one of the quarks produced in the top decay was less energetic and did not survive the f_{cut} requirement.

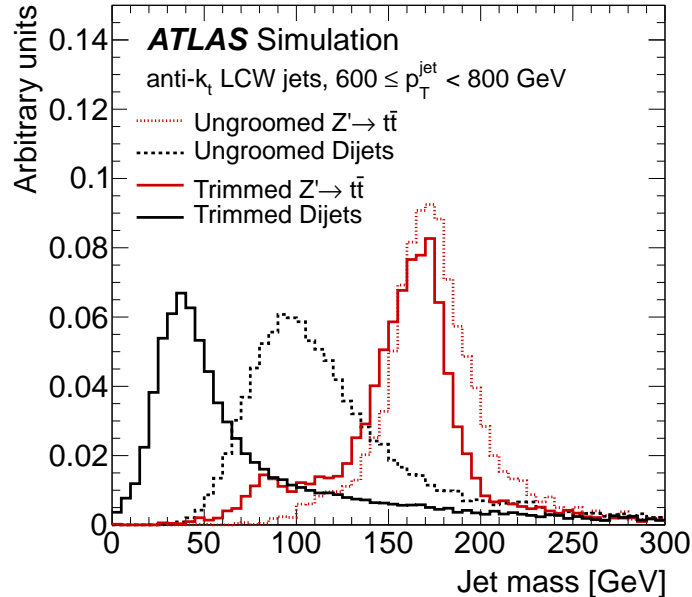


Figure 2.6: Illustration of the effect of jet trimming on light jets and top jets [23].

2.2 Motivation

The Standard Model (SM) of particle physics is one of the most successful theories in the history of science. Evoking the principle of gauge invariance and requiring only few fundamental particles it lends numerous predictions that have been tested and confirmed by experiment. The SM describes the strong, weak and electromagnetic interactions between the fundamental particles - three generations of fermions, 4 gauge bosons, mediating the interactions between the fermions, and the Higgs boson. Measurements testing the underlying rules and strengths of these interactions have

only confirmed the predictions of the SM. With the discovery of the Higgs boson in 2012, all particles predicted by the model have been discovered and the SM is self-consistent up to the Planck scale without the introduction of new physics. One may conclude that this is the beginning of the end, that the fundamental laws of physics have been understood and all that remains is to refine calculations. However, there are indications that this is not the case coming both from experimental observations and unanswered conceptual questions.

2.2.1 Open questions

Experimentally, it is known that only about 15% of the matter in the Universe is made up of the fundamental particles described in the SM, while the rest is referred to as *dark matter* indicating our lack of knowledge of its nature. Similarly, based on experimental measurements of neutrino oscillations, we know that neutrinos have some non-zero mass, which is not accounted for in the SM as it is formulated today. It is possible to extend the SM to account for neutrino masses, but it is generally not agreed upon which of the proposed mechanisms for acquiring mass is the correct one. One more important puzzle comes from the observed matter-anti-matter asymmetry. There is no sufficient source of baryon asymmetry in the SM to explain why we see only matter in the observable Universe (the only source of anti-matter being from collisions, either via cosmic rays entering the atmosphere or via manmade accelerators).

From the theoretical perspective, there are multiple conceptual open questions that cannot be adequately addressed by the SM alone. For example, a Higgs boson at 125 GeV provides a mechanism for the remaining particles of the SM to obtain mass, however, this comes at the expense of the challenge of explaining the mass of the Higgs itself. Since the Higgs is described by a scalar field, there is no natural bound for the Higgs mass parameter in the Higgs sector Lagrangian and the only way to obtain the observed mass is to postulate unnatural cancellations of order the Planck mass in the process of renormalization. Notably, the dominant diagram in the higher order divergent contributions to the Higgs mass come from top quark loops and any solution to the hierarchy problem would have to treat top quarks preferentially. From the aesthetic perspective, another unsatisfactory SM feature comes from the large number of required input parameters, including masses and mixing angles, with no explanation as to their disparate numerical values. Finally, the SM does not provide a way to incorporate gravity and is therefore unsuited for addressing any questions relating to the early universe where a simultaneous description of gravitational and quantum effects become important.

2.2.2 Proposed solutions

Attempt to resolve these questions have led to a plethora of proposals for extensions of the Standard Model. For example, Supersymmetry (SUSY) [24] postulates

an additional symmetry between bosons and fermions, introducing one superpartner of complimentary spin for each particle in the SM. The case for SUSY is particularly compelling since it naturally provides gauge coupling unification and a dark matter candidate without specifically being designed to solve these problems. SUSY also provides a solution to the hierarchy problem since, with the inclusion of the superpartners, the loop diagrams contributing to the diverging Higgs mass are canceled by loop diagrams of the corresponding superpartners that come with an opposite sign. Since superpartners with masses equal to their SM counterparts have not been found, SUSY must be a broken symmetry. The masses of the superpartners must be different, making the cancellation imperfect. In order for SUSY to still provide a solution to the hierarchy problem, be it with some minimal fine tuning, superpartners that contribute the most to the cancellation, such as the top superpartner, must be close to the TeV scale and therefore discoverable at the LHC [1].

Another class of models that are similarly comprehensive in addressing the majority of open questions are characterized by postulating the presence of extra dimensions². In these models, the hierarchy problem (restated to ask why gravity is so much weaker than the other forces) is addressed by allowing gravity to extend into an additional warped dimension, while restricting the rest of the forces to our usual 3 large dimensions. An experimentally observable consequence of the realization of such models is the appearance of excitations of the SM particles, manifesting themselves as new heavy resonances. Examples include Z' and W' bosons as well as g_{KK} (excitations of the graviton). Due to their large mass these resonances can decay into highly boosted top quark pairs, or in the case of the W' to a top and a b-quark.

These are only a few examples of the large variety of proposed extensions to the SM, a more comprehensive summary of the alternatives and their importance for directing the future experimental program are discussed in [1].

2.2.3 Role of the top quark

Top quark pair production is important for searches in multiple ways: the cross-section can be enhanced by tops originating from the decay of new particles, top pairs are often a dominant background which calls for a detailed understanding of the top event kinematics, and finally, cross-section measurements provide new information on the gluon PDF.

Due to its large mass the top quark often plays a special role in the way particles from new physics models relate to the SM particles. For example, in SUSY two process that would enhance top pair production are gluino and stop pair production. The corresponding Feynman diagrams are shown in Figure 2.7. These two signatures are particularly important for SUSY to solve the hierarchy problem. In order to stabilize

²Another popular alternative is to allow for the possibility that elementary particles are in fact composite. This set of models has been shown to be dual to theories with wrapped extra dimensions [1].

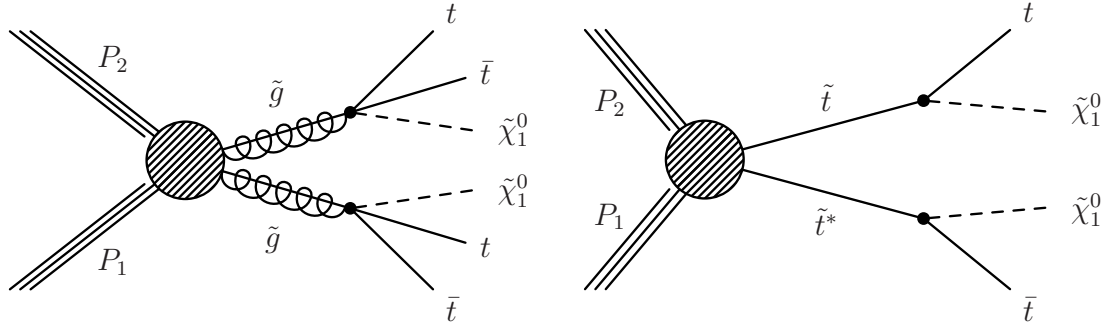


Figure 2.7: Gluino (left) and stop (right) pair production Feynman diagrams [25].

the Higgs mass by canceling contributions to it from top loop diagrams, stops must be light. With the limits on new particle masses now in the TeV range and beyond, it has been suggested that stops, higgsinos and gluinos may be the only SUSY particles with sufficient cross-sections to be discovered in the LHC environment. Additionally, top pair resonances are also present in many alternate new physics models such as wrapped extra dimensions and topcolor. Due to experimental constraints, these resonance are already excluded below a few TeV. Therefore, if they do exist, their decays must result in the production of highly boosted tops.

In pursuing any hints of new physics, studying differential distributions is particularly important since contributions from new physics to the total cross-section may not be observable with the current precision of theoretical predictions and experimental measurements, but enhancements of the cross-section may grow to a detectable level in certain kinematic regions without producing resonant structure. Therefore, production of tops with a high boost is particularly interesting as the limits on new physics continue to be pushed to higher and higher mass scales.

In processes where tops may not be directly produced, top pair production nevertheless remains a notable if not dominant background due to its rich decay. The top itself nearly always decays to a W-boson and a b-quark, but the W can either decay to a quark and an anti-quark or a lepton and the corresponding neutrino. For top pair production, this decay chain can result in events with 0,1 or 2 leptons, missing energy, 2 b-quarks and additional partons. For models such as SUSY which can have long decay chains and produce similarly rich final states, top pair production is the dominant background. For searches relying on the presence of b-quarks to separate the desired signal from the large multi-jet background, top pairs are once again a challenge, not only in the case where both tops decay hadronically, but also when a lepton is lost due to detector acceptance. In all these cases, the uncertainties associated with the prediction of the top pair background are hindrance to discovery of new particles and therefore refining our understanding of the modeling of these events is crucial.

Measurements of the $t\bar{t}$ cross-section at the LHC also help refine our knowledge

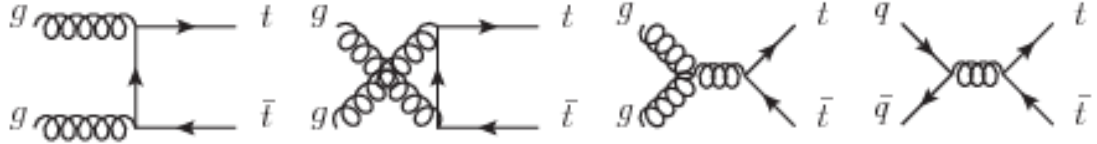


Figure 2.8: Dominant leading order top pair production Feynman diagrams at the LHC [26].

of the proton PDFs. The three leading-order (LO) Feynman diagrams responsible for top pair production at the LHC are shown in Figure 2.8. Since the LHC is a proton-proton collision machine and the proton does not contain valence anti-quarks, $q\bar{q}$ initiated processes are disfavored. The dominant production mechanism is through gluon-gluon fusion, accounting for $\sim 85\%$ of the produced top pairs [27], making $t\bar{t}$ cross-section an important probe of the gluon PDF. Since top quarks are relatively

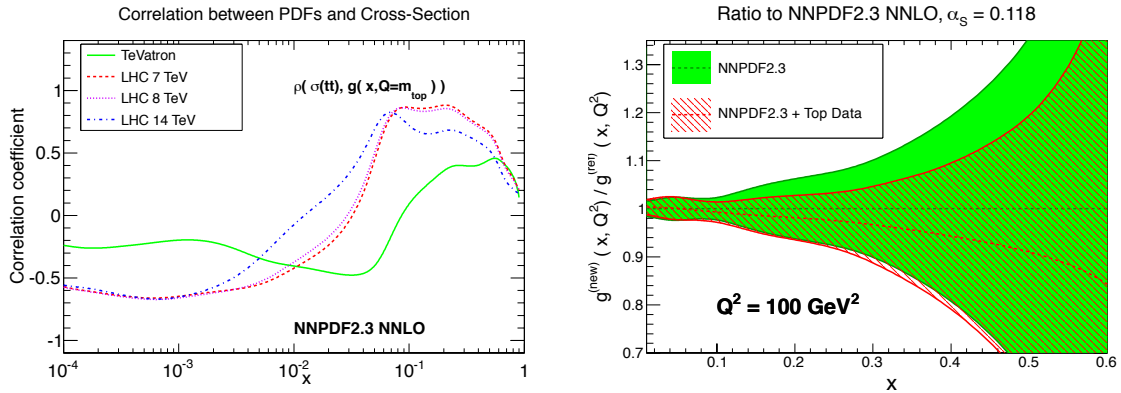


Figure 2.9: Effect on the gluon PDF from including top cross-section measurements in the global PDF fit by the NNPDF collaboration [27].

heavy, the $t\bar{t}$ production is most sensitive to medium-x values for the gluon PDF as shown in Figure 2.9 (a). It is interesting to note that the correlation is dependent on the center of mass energy of collision. The higher the energy, the lower parton momentum fraction is needed to produce tops. Therefore, measuring the cross-section for different center-of-mass energies and differentially can provide complimentary information for the gluon PDF. The above illustration comes from a recent study by the NNPDF collaboration which demonstrates that including top inclusive cross-section measurements from the Tevatron and the LHC in global PDF fits reduces the uncertainty of the gluon PDF by $\sim 20\%$ for x in the range of 0.15 to 0.6. This can be seen in Figure 2.9 (b) showing the PDF uncertainty before and after the inclusion of top cross-section data in the global fit [27]. This reduction of PDF uncertainty benefits cross-section predictions for both SM and new physics processes. Eventually, these improvements in our knowledge of the gluon PDF will also allow for better predictions

at future experiments, just as the LHC benefits from the PDF studies made in DIS experiments and the Tevatron.

Chapter 3

Analysis strategy

In the analysis described in this thesis the measurement of the top transverse momentum is extended into the highly boosted regime, spanning p_T of 300 GeV to 1.2 TeV, using 20.3 fb^{-1} of $\sqrt{s} = 8$ TeV proton-proton collision data. The cross-section is reported within a fiducial region defined at the stable *particle level* as well as extrapolated to the full phase space at the *parton level*. Parton level measurements report the cross-section as a function of the top parton p_T , while particle level results are presented as a function of the kinematics of objects built from stable generator particles. The previous ATLAS measurement of the top quark pair production cross-section performed with 5 fb^{-1} of $\sqrt{s} = 7$ TeV data reached top $p_T = 800$ GeV, with the last bin of the distribution spanning from 350 GeV to 800 GeV [28]. The most recent CMS measurement using 12.1 fb^{-1} of $\sqrt{s} = 8$ TeV reached top $p_T = 400$ GeV, with the last bin 320-400 GeV [3]. In both these measurements the top p_T spectrum found in data is corrected from the detector reconstructed level to the parton level only.

Targeted decay channel

The decay of a top pair consists of 2 W-bosons and 2 b-quarks. Three $t\bar{t}$ decay channels can be distinguished based on the W decays: all hadronic $t\bar{t}$ (both W's decay to quarks), semi-leptonic $t\bar{t}$ (only one W decays to quarks) and dilepton $t\bar{t}$ (both W's decay to leptons) with branching fractions of approximately 46%, 44% and 10%, respectively. All hadronic $t\bar{t}$ is the most abundant, however, due to the large multijet production cross-section at the LHC this channel suffers from an overwhelming background. The dilepton channel is the most pure since events with two isolated leptons are relatively rare, but it also has the smallest branching fraction. In addition, the presence of two neutrinos results in a worse momentum resolution. For these reasons, the measurement is performed in the semi-leptonic channel where the presence of a single lepton allows for better $t\bar{t}$ system reconstruction, a powerful trigger handle and good multijet background suppression.

The targeted event class is further restricted to events where the leptonically decaying W produces an electron or muon either directly or via an intermediate τ lepton. This avoids the additional complication and uncertainties associated with reconstructing hadronically decaying τ 's. Events with an electron will hereafter be referred to as $e+\text{jets}$, while those with a muon as $\mu+\text{jets}$.

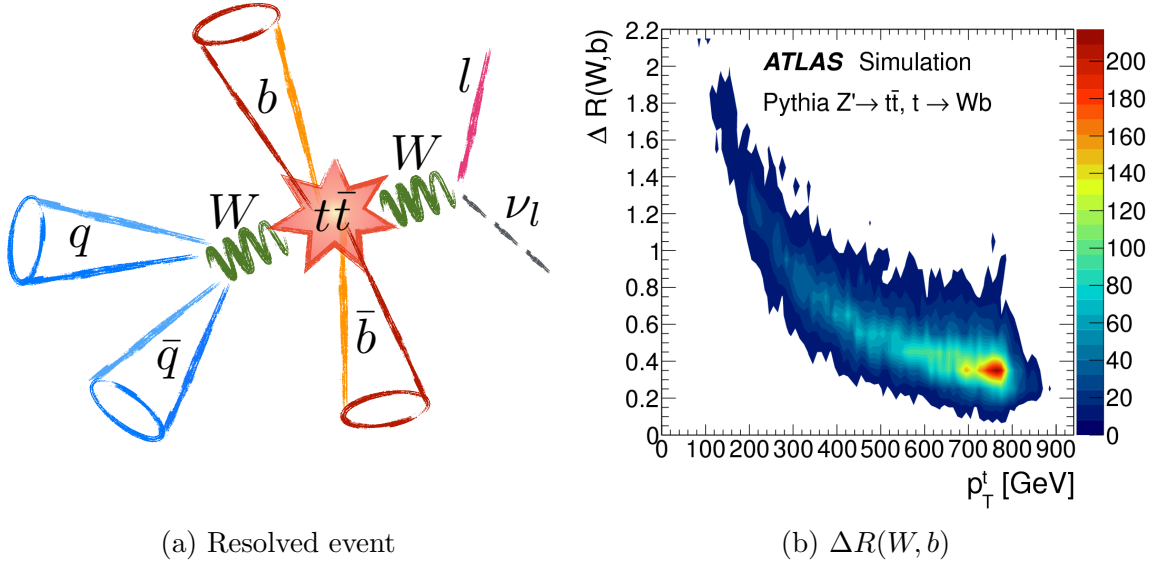


Figure 3.1: Illustrations of (a) the resolved topology and (b) the expected distance between the W boson and the b -quark as a function of top transverse momentum.

The highly-boosted top quark pair topology

The semi-leptonic decay is illustrated in Figure 3.1 (a). Traditionally, top analysis reconstruct the system under the assumption that all 4 quarks present in the event result in narrow, well separated jets. In this *resolved* topology, the general strategy is to select events by requiring there are at least 4 jets, one lepton and some missing energy corresponding to the neutrino. These objects are then input into a Kinematic Likelihood fitter, which takes into account the top and W masses and widths as well as resolutions for the various objects in order to assign the appropriate combination of objects to each of the two tops in the event. At lower masses of the $t\bar{t}$ system this approach provides a clean sample and good resolution. However, when the $t\bar{t}$ system is produced with higher mass and the tops become boosted, this approach begins to fail as the 3 quarks in the hadronically decaying top get increasingly close to each other. The distance between the W boson and the b -quark as a function of top p_T is shown in Figure 3.1 (b). Using small radius (small- R) jets with $R = 0.4$ (default

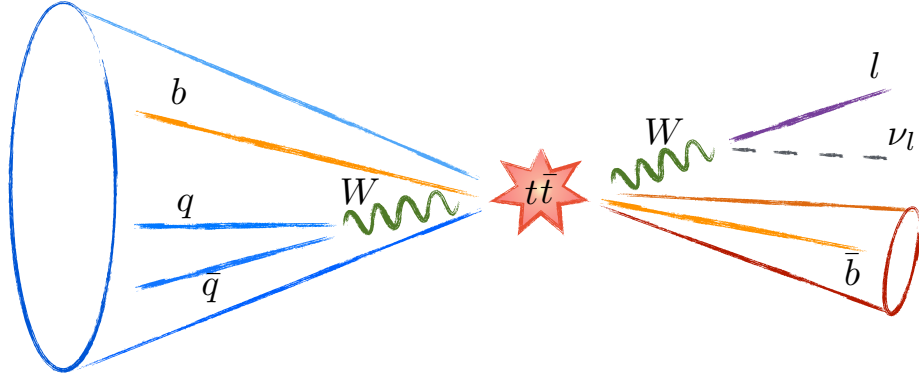


Figure 3.2: The boosted topology

in ATLAS) to reconstruct the top can result in overlapping jets starting at $p_T = 400$ GeV. The requirement of at least 4 small- R jets then results in decreasing efficiency to select and properly reconstruct these events. Note that even if the quarks are separated by, for example, 0.6, this would still be problematic. Even though, in this case the right number of jets may still be reconstructed, there is an increasing chance of misassigning clusters from one quark shower into the jet of another quark.

The alternate approach taken here is to reconstruct the top using a single large radius (large- R) jet as shown schematically in Figure 3.2. The radius is chosen to be $R = 1.0$, which is large enough to allow the usage of this method for moderately boosted tops, 300-400 GeV, where results can be compared to those obtained using resolved reconstruction methods. Reconstructed large- R jets are trimmed and subsequently, the jet mass and first splitting scale are used to determine if a jet in fact contains a top decay. To further eliminate contamination from background processes, events are also required to contain at least one b -quark, as identified by a b -tagging algorithm, associated with one of the reconstructed tops.

Fiducial particle level measurements

Traditionally, the top cross-section has been presented at the parton level to allow comparisons to state of the art fixed order calculations that are not implemented in showered MC. The idea of reporting a particle level top cross-section has drawn attention only recently as a way to minimize the theoretical input into the result, limit the generator dependence of the definition of the reported quantity, as well as reduce theoretical uncertainties. The particle and parton level are highlighted in Figure 3.3.

The process of correcting the data for detector effects, referred to as *unfolding*, involves deriving a transfer matrix and an efficiency correction to transform the detector level quantity, e.g. p_T of a jet, to the truth level quantity, e.g. top parton p_T . When unfolding to a fiducial region at particle level with acceptance cuts following closely the detector level cuts, the data is corrected only for resolution and efficiency effects.

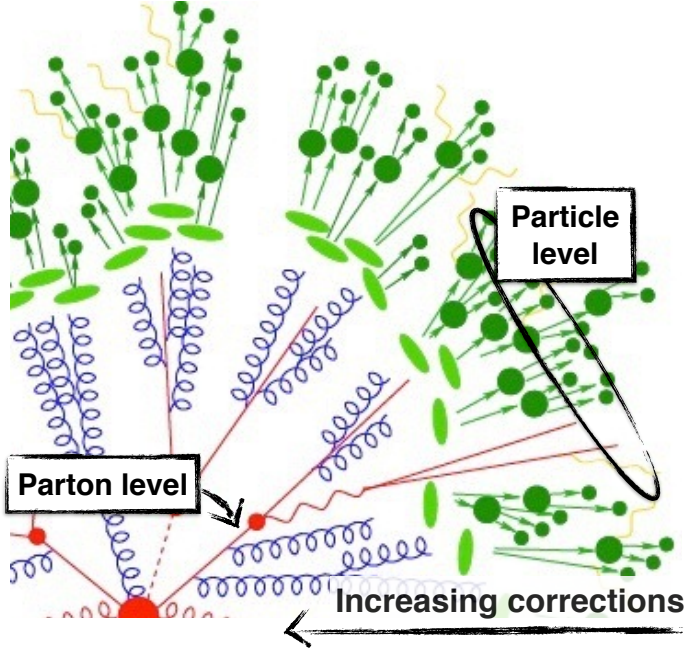


Figure 3.3: Particle and parton level illustrated using the Sherpa generated event from Chapter 2.

On the other hand, when unfolding to parton level, the transfer matrix also includes effects from hadronization and parton shower, as well as extrapolation to phase space beyond the detector geometrical acceptance. The larger correction needed to unfold to parton level is associated with a correspondingly larger uncertainty.

A further complication arises from the fact that MC generator definitions of the top parton may differ significantly since a bare parton is intrinsically ill-defined. In particular the MC definition would depend on merging scheme choice and parton shower among other.

From the perspective of improving $t\bar{t}$ production modeling, a particle level result also allows for the measurement to remain useful for comparisons with fixed order calculations with potentially improved parton shower, merging and hadronization models in the future.

For these reason, the main result of this measurement is the top quark pair production cross-section as a function of the particle level large-R jet, referred to as the *particle top-jet candidate*, within a fiducial region defined by the detector level acceptance. The cross-section is also presented at the parton level extrapolated to the full phase space in order to illustrate the evolution of the uncertainty between the two definitions.

Chapter 4

The ATLAS Experiment

4.1 Large Hadron Collider

The Large Hadron Collider resides in a 27 km underground tunnel on the border of Switzerland and France. In 2012, it produced proton-proton collisions at center of mass $\sqrt{s} = 8$ TeV. It is expected to reach its design center of mass energy of 14 TeV in the forthcoming run.

To achieve such energies, protons are accelerated in several stages. The CERN accelerator complex is shown in Figure 4.1. First, the proton beam is produced in Linear Accelerator 2 (LINAC 2) by using an electric field to strip the electrons from atoms in hydrogen gas. The resulting protons are accelerated to 50 MeV using RF cavities and kept in a focused beam by quadrupole magnets. In the next two stages, the protons are accelerated to 1.4 GeV and then 25 GeV in the Proton Synchrotron Booster (Booster) and Proton Synchrotron (PS), respectively. Even though the PS can accept protons directly from the LINAC2, the intermediate Booster stage with its 4 superimposed synchrotron rings allows for more protons to be injected in the PS simultaneously. In the last preparatory step, the 25 GeV protons from the PS enter the Super Proton Synchrotron (SPS) and get further accelerated to 450 GeV. The beam is contained in the 7 km SPS ring with the help of 1317 room-temperature electromagnets. From the SPS, protons are injected in the LHC ring in two counter rotating proton beams and finally accelerated to their final energy of 4 TeV using 16 superconducting RF cavities cooled to 4.5 K. The beams are kept on their circular trajectory by 1232 dipole magnets and continuously refocused by 392 quadrupole magnets. Higher multipole magnets, bringing the total number of magnets to ~ 9600 , provide the remaining finer corrections to the proton trajectories.

The two proton beams intersect at the 4 experiments: ATLAS, CMS, ALICE and LHCb. While ATLAS and CMS are general purpose detectors, ALICE specializes in heavy-ion physics and LHCb in B-physics. The measurement presented in this thesis is based on collision data collected with the ATLAS Experiment in 2012. Performance studies of the object and event reconstruction methods used in this analysis also utilize

the data collected in 2011 at $\sqrt{s} = 7$ TeV. The 2011 and 2012 data taking periods are collectively referred to as the LHC Run I.

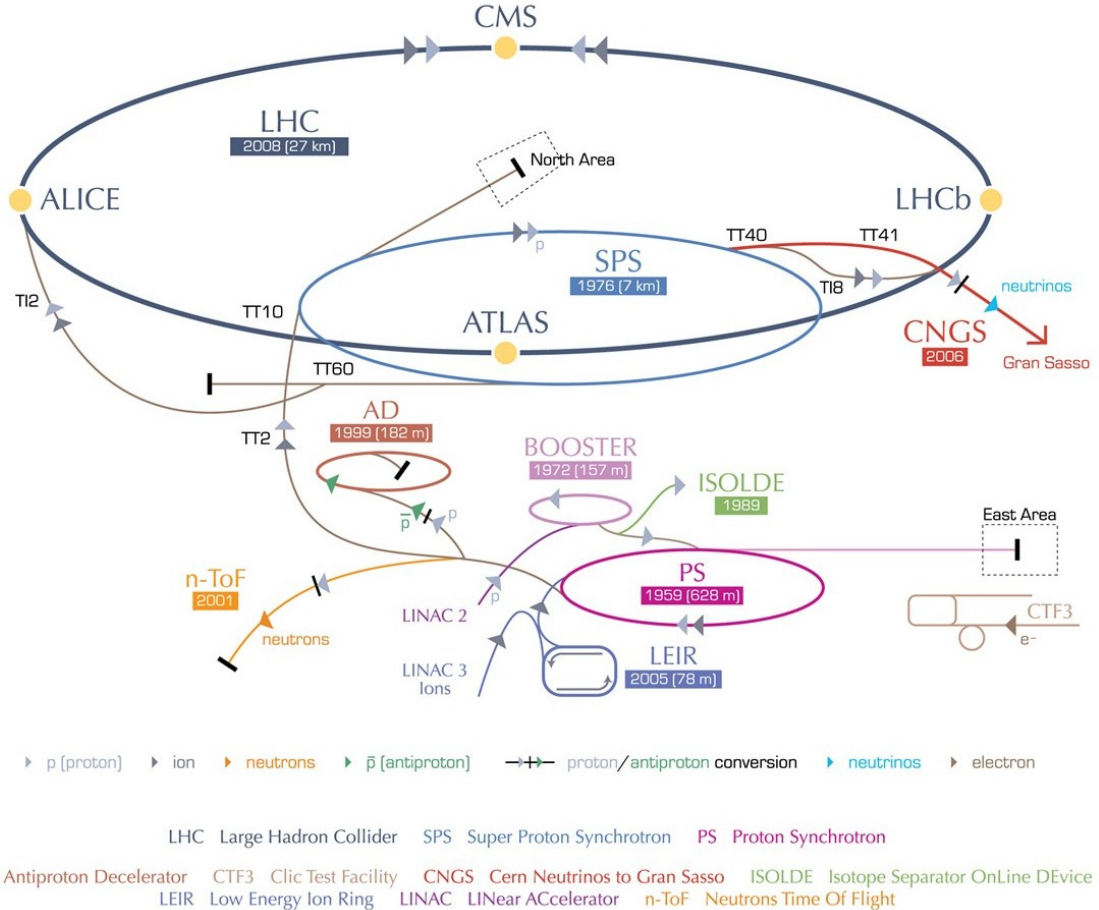


Figure 4.1: CERN accelerator complex

4.2 LHC Run I proton-proton collision dataset

Due to the mechanism of acceleration employed by RF cavities the proton beams are not continuous, but rather separated into tight proton bunches. In the 2012 run, the LHC operated on average with 1380 bunches spaced at 50 ns intervals, each bunch containing 1.7×10^{11} protons. Given these parameters along with the transverse size of the beam, the LHC *instantaneous luminosity* can be obtained from:

$$L = \frac{N_b^2 n_b f}{A} \quad (4.1)$$

where N_b is the number of protons per bunch, n_b is the number of circulating bunches, f is the bunch revolution frequency and A is the cross-sectional area of the interaction region, which can be derived from the beam parameters and beam crossing angle. The maximum instantaneous luminosity reached in 2012 was 7.7×10^{33} . Due to smaller number of protons per bunch and larger interaction region, the maximum instantaneous luminosity for the 2011 run was 3.7×10^{33} .

The beam conditions listed above are only representative. The actual parameters continuously change. One example of a source of a change over the duration of a run is the depletion of protons in the bunches after multiple beam crossings have taken place. Due to these changes, the quantity of interest for physics analysis is the total recorded luminosity given by integrating the instantaneous luminosity over time. Knowing the total luminosity allows conversion of the measured number of events for any process into a cross-section measurement by dividing the number of events by the integrated luminosity. The integrated luminosities are 4.57^{-1}fb with uncertainty of 1.8% [29] and 20.3^{-1}fb with uncertainty of 2.8% [29] for the 2011 and 2012 run, respectively. The increase as a function of time is shown in Figure 4.2.

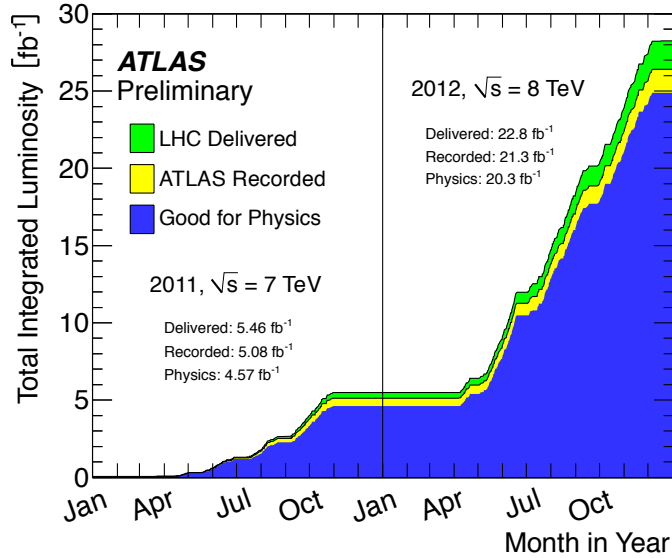


Figure 4.2: Total integrated luminosity of the Run I dataset

The beam conditions also determine a second important quantity, namely the number of proton-proton collisions that take place in the same bunch crossing, commonly referred to as *pile-up*. The ability to extract physics results from the recorded events is strongly affected by the number of pile-up events. Higher pile-up results in more activity in the detector which complicates the combinatorial problems that must be solved to reconstruct events. As a result, increasing pile-up eventually leads to degraded performance. In the 2012 run, due to LHC operation precautions the

machine was operated at higher number of protons per bunch with a larger interbunch spacing. As a result the pile-up was larger than initially anticipated by the experiments. The distribution of the luminosity collected as a function of the mean number of interactions per bunch crossing for the 2011 and the 2012 datasets are shown in Figure 4.3. Successful correction for these pile-up conditions was made possible by both optimizing the existing reconstruction algorithms for pile-up robustness and deploying novel techniques for suppressing the effects of extraneous energy depositions on quantities relevant for the selection of physics objects. The techniques relevant to this analysis will be described in the chapters on object reconstruction and event selection.

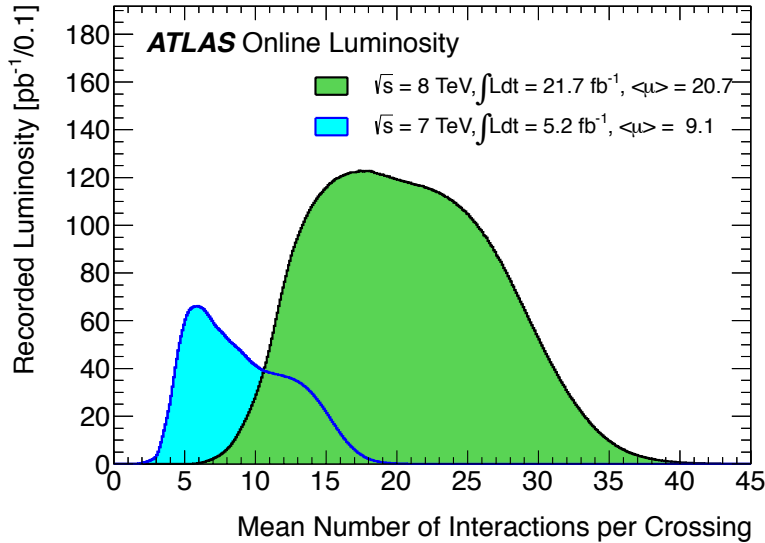


Figure 4.3: Mean number of interactions per crossing in the 2012 LHC run

4.3 ATLAS Detector

ATLAS [30] is a general purpose particle detector. It performs direct measurement of the trajectory and/or energy of electrons, muons, photons, pions, kaons, protons and neutrons. These measurements are then used to infer the energy and direction of flight of the unstable particles that produced them, ultimately providing information about the original products of the hard scattering partons. Particles are reconstructed using the complimentary information from four specialized sub-systems including a tracker, an electromagnetic (EM) and hadronic calorimeters and a muon spectrometer. These are organized as cylindrical layers around the interaction point as can be seen in the ATLAS detector overview in Figure 4.4. At the center is the tracking system, which employs silicon and transition radiation technologies immersed in a

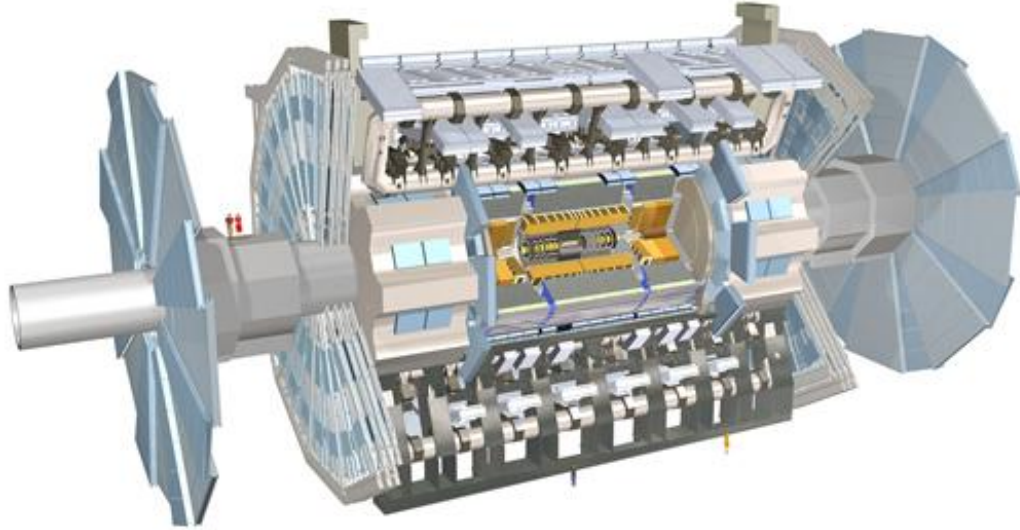


Figure 4.4: Overview of ATLAS

magnetic field for the reconstruction of charged particles trajectories and vertexing. Going radially away from the interaction point, the next detectors are the calorimeters. Both the EM and the hadronic calorimeters employ a shower sampling method with alternating layers of one material that elicits and absorbs the particle shower and another that measures the deposited energy. The EM calorimeter is built to contain electron and photon showers. Even though hadron showers loose approximately 2/3 of their energy in the EM calorimeter, its depth is not sufficient to contain them. This task is delegated to the hadronic calorimeter built of a denser material which allows it to absorb TeV-scale hadron showers. Furthest from the interaction point, enveloping ATLAS, is the muon system. It provides an independent measurement of muon momentum, which can later be complemented with information from the inner tracking system. Due to detector readout, data processing and storage constraints, it is not possible to record the output of the entire detector for every inelastic proton-proton interaction. A dedicated tiered trigger system is employed to make a decision whether each event should be retained for offline analysis. The following sections provide a detailed description of each of the detector sub-systems as well as the trigger.

4.3.1 Inner Detector (ID)

The goals of the tracking system include charged particle momentum measurement and reconstruction of primary and secondary vertices. It is situated in the center of ATLAS and provides the first measurement of collision decay products, with its first measurement point at 50.5 mm and the last at 1082 mm. The detector extends over 5540 mm along the beam direction, corresponding to a track measurement up to $|\eta| < 2.5$. The momentum measurement is made possible by a 2T axial magnetic field provided by a solenoid surrounding the ID volume. The ID consists of three sub-detectors depicted in Figure 4.5. Each subdetector consists of a barrel region where the sensors are arranged parallel to the beampipe and two endcap regions where sensing elements are aligned transverse to the beam. At the center is the Pixel Detector (Pixel) with highest granularity composed of silicon pixels, next is the Semiconductor Tracker (SCT) which is built up from silicon strip sensors. The outermost component is the Transition radiation tracker (TRT) which uses gas filled tubes interleaved with a polymer material in order to allow numerous charged particle trajectory measurements along with electron/pion separation at a reasonable cost.

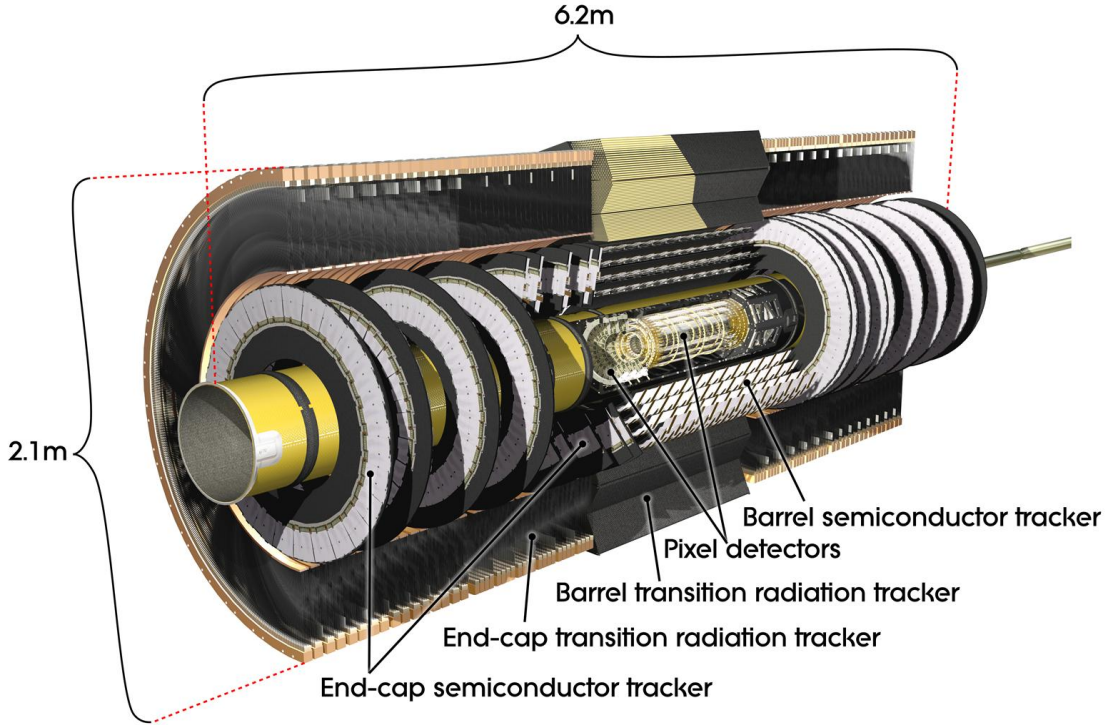


Figure 4.5: Overview of the Inner Detector

Pixel detector (Pixel)

Situated closest to the interaction point, the Pixel detector needs to have the highest granularity in a harsh high radiation environment. Providing the first few trajectory measurements also makes it crucial for secondary vertex reconstruction, which is essential for distinguishing jets originating from b -quarks.

The Pixel consists of 3 barrel layers and 3 endcap disks on each side of the barrel. The overall structure is shown in Figure 4.6. The barrel layers are suspended at radii of 50.5 mm, 88.5 mm and 122.5 mm. The endcaps sit at 495 mm, 580 mm and 650 mm away from the interaction point. This geometry allows charged particle tracking coverage up to $|\eta| = 2.5$.

The basic building block of the Pixel is a module. Barrel modules are arranged into long structures, parallel to the beam direction, called *staves*. Endcap modules are arranged into petals and then into wheels, with the sensing element perpendicular to the beam axis. These supporting structures also host power, clock, command and data lines to and from each module. The staves are arranged at an angle with respect to a cylindrical shape in order to allow for some overlap. In the wheels, modules cover both faces of the wheel with a relative offset, so that a region of overlap is similarly present. Such arrangement prevents gaps in coverage due to edge effects.

Each module hosts 16 front-end readout chips, each of which is responsible for reading out a grid of 2880 silicon pixels, electronically connected to the readout chips via bump bonds. Each pixel is a p-n junction built of n-type bulk with both p⁺ and n⁺ impurities. The additional n⁺ implants allow the pixels to operate even after the inversion of the bulk from n-type to p-type caused by the high radiation dose. Each pixel measures 50 μm by 400 μm with the longer side along the direction of the beam. This pixel size allows charged particle hit resolution of approximately 115 μm along the beamline and 10 μm in the transverse direction.

Semiconductor tracker (SCT)

The SCT is composed of 4 barrel layers and 2 endcaps, each with 9 disks, also visible in Figure 4.6. In the radial direction, the barrels cover the range from 299 to 514 mm. In the longitudinal direction the barrel reaches 749 mm away from the interaction, beyond which the range is extended by the endcap disks, with the last disk at 2735 mm.

Again the basic building block is the module. Similarly to the Pixel, the modules are arranged into staves in the barrel and sectors in the endcaps. Instead of pixel however, each SCT module reads out a set of silicon strips with a pitch of 80 μm and length 6.4 cm. Each module hosts two layers of strips, where one layer is aligned at a stereo angle of 40 mrad with respect to the other. This allows to provide hit position information along both the transverse and the longitudinal direction of the strips at a reduced cost. Given these parameters the transverse resolution is $\sim 17 \mu\text{m}$ and the

longitudinal resolution is $\sim 580 \mu\text{m}$ for tracks with $|\eta| < 2.5$.

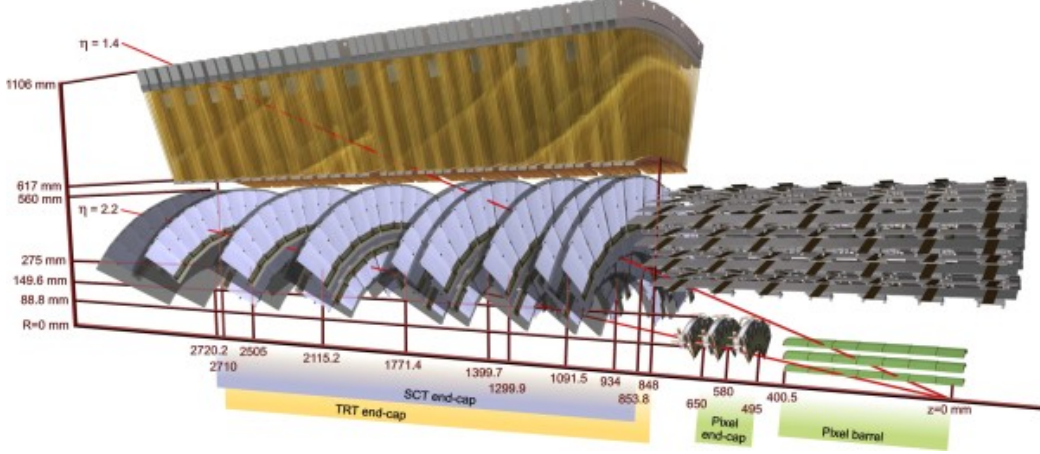


Figure 4.6: Inner Detector barrel and endcap components

Transition Radiation Tracker (TRT)

The TRT extends the charged particle tracking volume up to radius of 1106 mm. It also allows to distinguish electrons from pions based on their transition radiation while traversing this detector. It is composed of polyimide drift tubes arranged in a barrel and two endcaps. The barrel tubes are 144 cm long and the endcap are 37 cm. The barrel is composed of 73 layers of longitudinally arranged wires, while the end-caps are built of 160 planes of tubes in a radial arrangement, giving a total of approximately 350,000 read-out channels. Each track would leave approximately 35 hits in the TRT for pseudorapidity below 2.0.

The outer shell of each tube has a diameter of 4 mm. It is a multi-layer film of thickness $35 \mu\text{m}$ held at -1500V . Inside each tube is a $35 \mu\text{m}$ -wide anode tungsten wire held at ground potential, suspended in a Xe-based gas mixture. When a charged particle passes through the gas it causes ionization and free electrons drift to the anode, where the signal is amplified and finally read out. The signal is further enhanced due to transition radiation resulting from the passage of the particles through polymer fibres sitting between the tubes. This additional radiation caused by traversing the boundary between two materials is dependent upon the Lorentz factor of the particle. Therefore, particles with lower mass result in higher signal. By putting a threshold on the signal amplitude at each straw, one can assign a probability that the hit was made by an electron.

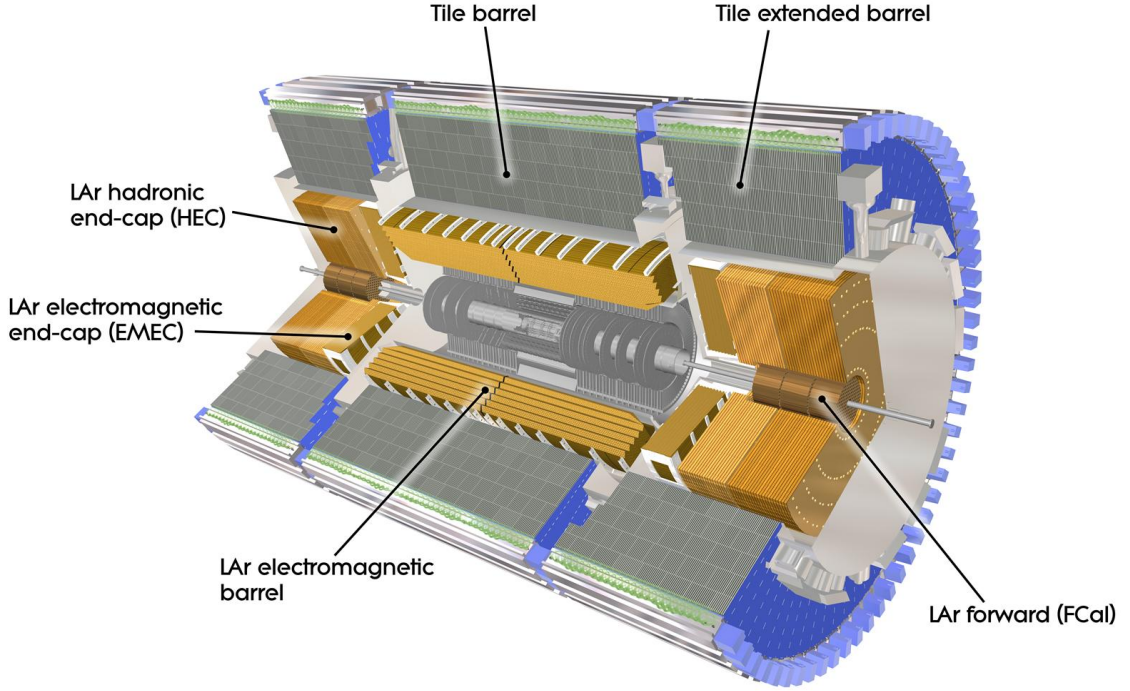


Figure 4.7: Overview of the Calorimeter system

4.3.2 Calorimeters

A basic overview of the calorimeter structure is given in Figure 4.7. The barrel consists of a Liquid Argon (LAr) electromagnetic calorimeter and a Tile hadronic calorimeter. Each endcap consists of three LAr based wheels, the first intended for measuring EM-energy (EMEC), the second intended to contain hadronic showers (HEC) and lastly the Forward calorimeter (FCal), closing the gap between the HEC and the beam pipe, intended to capture the most forward radiation.

Containment of electromagnetic showers, for incoming electrons, photons and other electromagnetically interacting particles, is ensured by radiation lengths of at least 22 and 24 radiation lengths, X_0 , in the barrel and endcap regions, respectively. Even though jets deposit some portion of their energy in the EM calorimeter, whose interaction depth is approximately $1\text{-}2 \lambda$, they generally continue on to the hadronic calorimeter. The hadronic calorimeter has lower resolution, but it is capable of containing TeV scale hadronic showers with an interaction depth of $11\text{-}18 \lambda$, depending on η .

Electromagnetic calorimeter

The EM barrel is a sampling calorimeter alternating lead absorbers with liquid argon active medium and kapton electrodes. The layers are bent in an accordion shape that allows a gapless measurement in the azimuthal direction. A sketch of the geometry of a barrel module is shown in Figure 4.8.

The barrel provides a precision measurement of energy and direction for $|\eta| < 2.5$. It is composed of three layers with increasingly coarser segmentation. The first layer is a presampler with a thickness of $4.3 X_0$. It is finely segmented in the direction along the beam, with a cell width of $\Delta\eta = 0.0031$, but rather coarse in the transverse direction, $\Delta\phi = 0.1$. The second layer forms the bulk of the EM calorimeter with depth of $16 X_0$ and lends equal resolution in both η and ϕ , with cell dimensions of approximately 0.025×0.25 . The combined measurement of these two layers determines the direction of flight for photons. The final layer 3 is a shallow $2 X_0$, with the same segmentation in ϕ , but twice as coarse in η .

The endcap region consists of two layers and extends the coverage to $|\eta| < 3.2$. Here, the accordion-shape wiggles are oriented along the axial direction to allow gapless measurement in η .

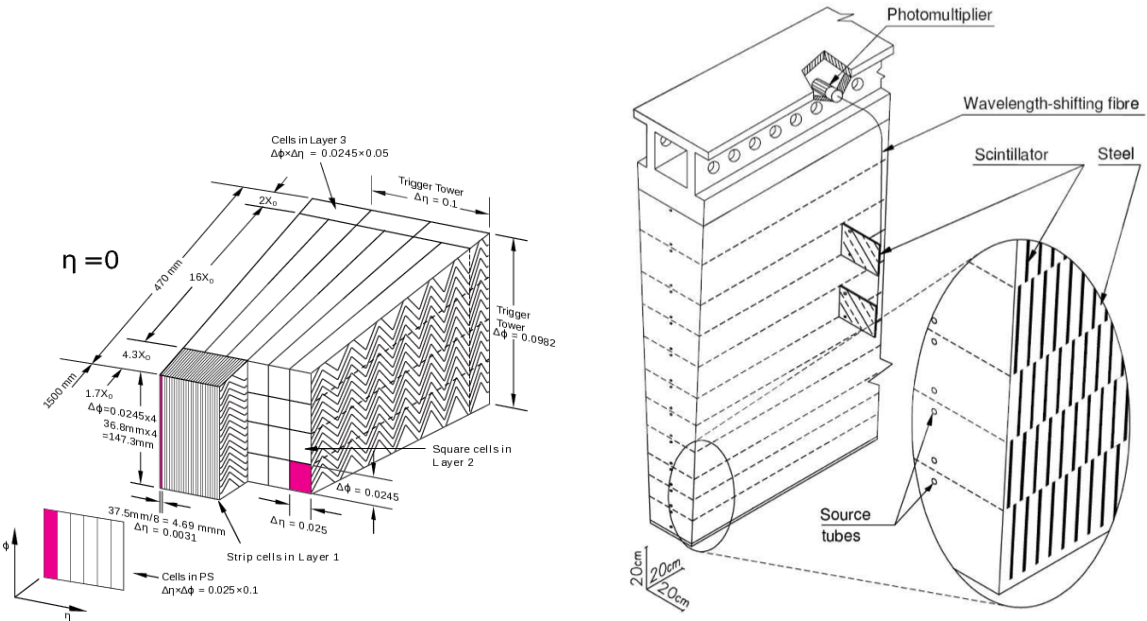


Figure 4.8: EM barrel module

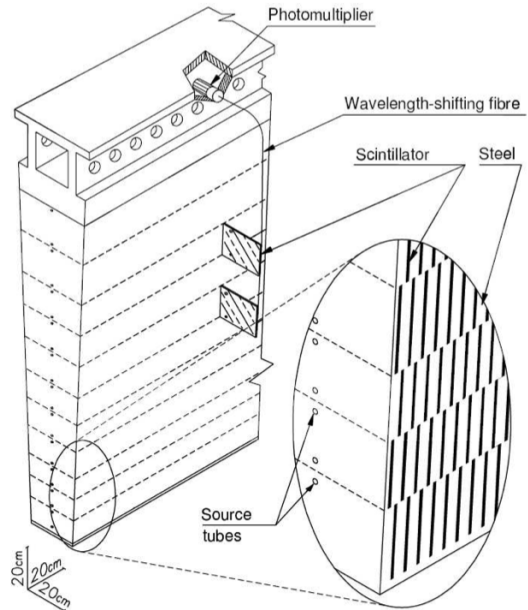


Figure 4.9: Tile barrel module

Hadronic calorimeters

ATLAS has three hadronic calorimeters covering the full η range up to 4.5. The Tile calorimeter employs steel absorber and scintillator tiles and extends up

to $\sim \eta = 1.7$. The Hadronic Endcap Calorimeter (HEC) uses copper absorber and liquid argon to extend the coverage to $|\eta| < 3.2$. Finally, enveloping the beam pipe with coverage up to $|\eta| < 4.5$, the Forward Calorimeter (FCal) ensures a near hermetic energy measurement, making it possible to attribute any remaining transverse momentum imbalance to neutrinos that escape detection. The arrangement of the electromagnetic calorimeter endcap, the HEC wheels and FCal modules in a single cryostat, shown in Figure 4.10, provides near gapless coverage in η .

The Tile calorimeter (Tile) is separated into a barrel for $|\eta| < 1$ and two extended barrels covering $1 < |\eta| < 1.7$. It extends radially from 2.28 m to 4.25 m and has a total depth of 7.4 interaction lengths. The structure of an individual Tile module is shown in Figure 4.9. It is based on the combination of steel absorber and scintillating tiles. As ionizing particles pass the scintillator, they produce ultraviolet light. The light is collected on wavelength shifting fibers, which shift the light to a longer wavelength and transport it to the photomultiplier tubes at the outside edge of the module. The fiber to PMT grouping is arranged such that the readout can differentiate three layers with depths 1.5, 4.1 and 1.8 interaction lengths as well as η segments of width 0.1. The individual readout cell dimension in the azimuth is given by the module width, $\Delta\phi = 0.1$.

Each HEC is composed of two wheels, each containing 32 modules. The shower sampling is realized by alternating copper and liquid argon layers. The front wheel has higher resolution given by 24 copper plates with 25 mm thickness, while the rear wheels have 16 copper plates with 50 mm thickness. The inter-plate spacing is ~ 8 mm of liquid argon separated into ~ 2 mm drift zones by suspended electrodes. These are mechanically separated into readout cells of size $\Delta\eta \times \Delta\phi = 0.1 \times 0.1$ for $|\eta| < 2.5$ and 0.2×0.2 beyond, allowing a measurement of the pointing angle for energy depositions.

The FCal closes the gap between the HEC and the beam pipe, covering the range $3.1 < |\eta| < 4.9$. It is built from 3 modules of 45 cm depth. Again liquid argon is used in the drift chambers for its radiation hardness. The first module uses copper as the absorber, while the two outer modules use tungsten for its superior ability to contain the hadron showers. A copper plate mounted behind the third module provides additional support in minimizing any hadronic shower leakage into the muon system.

4.3.3 Muon System (MS)

The design goal for the muon system is to perform standalone muon momentum measurements with approximately 10% resolution at 1 TeV within $|\eta| < 2.7$. In addition, it provides triggering capabilities within $|\eta| < 2.4$. The components of the muon system are highlighted in Figure 4.11. The magnetic field necessary for momentum measurement is provided by superconducting toroid magnets, one set of coils for the barrel region and two more sets of shorter coils for the endcaps.

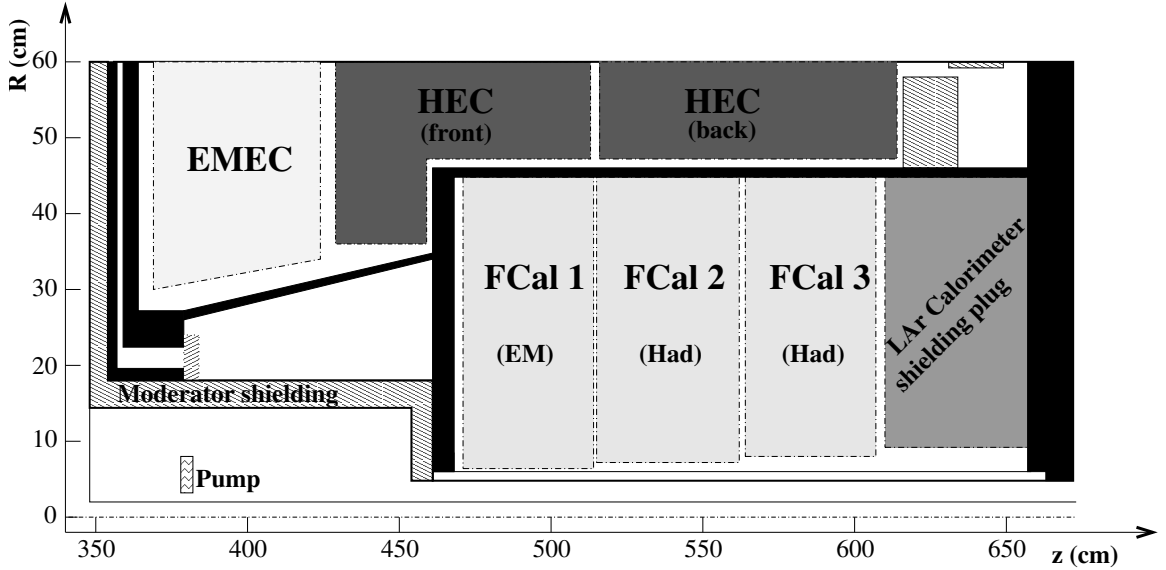


Figure 4.10: Arrangement of calorimeters in one of the two endcap cryotats.

Precision tracking chambers

Precision tracking chambers are arranged in three concentric cylinders at 5 m, 7.5 m and 10 m. The individual chamber size increase as a function of the distance away from the interaction point. As for the inner tracker, the geometrical arrangement ensures overlap between chambers in each layer allowing for gapless coverage and relative alignment based on tracks traversing multiple chambers per layer. In addition, there are 4 endcap wheels at 7.4 m, 10.8 m, 14 m and 21.5 m away from the interaction point, with the last wheel yielding the distinctive outer shape of the ATLAS detector.

There are two types of tracking chambers: Monitored Drift Tubes (MDT), covering the full η range in the outer barrel and up to $\eta=2$ in the inner barrel layer, and Cathode-Strip Chambers (CSC), covering the forward region of the inner layer, $2.0 < |\eta| < 2.7$. MDTs are pressurized aluminum drift tubes of approximately 30 mm diameter filled with Argon/CO₂ gas mixture. The anode is a gold plate tungsten wire held at 3080V with thickness 50 μm . There are 3 to 8 layers of tubes per chamber depending on its location always oriented along the ϕ direction, transverse to the beam. These parameters lend a resolution of approximately 35 μm per chamber. Since the MDT counting rate is limited to 150 Hz/cm² they are not suitable for the forward regions of the innermost layer where higher rates are expected. Instead, the forward region is instrumented with CSCs which provide momentum measurement at higher rate with better timing and spatial resolution. The chambers are arranged in two endcap wheels with 16 chambers each. One chamber contains 4 CSC planes, each plane built by two cathode strip planes sandwiching the anode wires. The cathode strips in one plane are arranged in the ϕ direction and the other in the η direction in

order to provide two dimensional space point measurement. The inter cathode gap is filled with Argon/CO₂ mixture. The anode wires suspended 2.5 mm away from both cathode strip planes are 30 μm thick and operate at 1900V. This design results in 40 μm resolution in the radial direction, away from the beam, and 7 ns timing resolution.

Trigger chambers

The trigger capabilities of the muon system are supplied by the Resistive Plate Chambers (RPC) in the barrel and Thin Gap Chambers (TGC) in the endcaps. As with the precision tracking chambers, different technologies are employed in the barrel and endcap since maintaining the required performance in the forward regions calls for higher granularity and higher rate capabilities. The barrel trigger system is composed of 3 RPC layers, the two inner layers sandwich the middle MDT layer and allow triggering on low p_T muons; the third RPC layer is located outside the outermost MDT layer and its reading combined with one of the inner RPC layers allows for longer measurement level arm and therefore, triggering on high p_T muons. The endcap trigger system is composed of 4 TGC layers, similarly arranged at various distances to allow for different lever arms in the measurement across the full range of momenta of interest.

4.3.4 Trigger System

The ATLAS trigger system has three tiers: Level 1 (L1), Level 2 (L2) and Event Filter. The L1 reduces the information to 75 kHz based on simple multiplicity and energy threshold requirements; L2 uses more refined information from regions of interest in the detector identified by the L1 trigger to further reduce the rate to 3.5 kHz; finally, the Event Filter uses the full power of the offline reconstruction software to determine whether the event should be written to tape, with a final output of up to 200 Hz.

L1 trigger uses calorimeter and muon system information. This allows triggering on missing energy, total energy, jets, electrons/photons, hadronic taus and muons. The decision is based on multiplicity and energy deposit thresholds. Maximum L1 latency, or the time before a decision must be made, is 2.5 μs . At the same time, the data-acquisition system has to also keep track of which data belongs to which bunch crossing so that when a trigger decision becomes available the appropriate event fragments can be collected. This task is particularly challenging in the calorimeters and the muon system where the measurement time is greater than the gap between successive events. In the calorimeter, the electronic signal shape generally extends over 100ns. In the muon system, the time of flight through the full detector is similarly longer than 25 ns.

In the case that an event is accepted the locations of energy deposits are forwarded

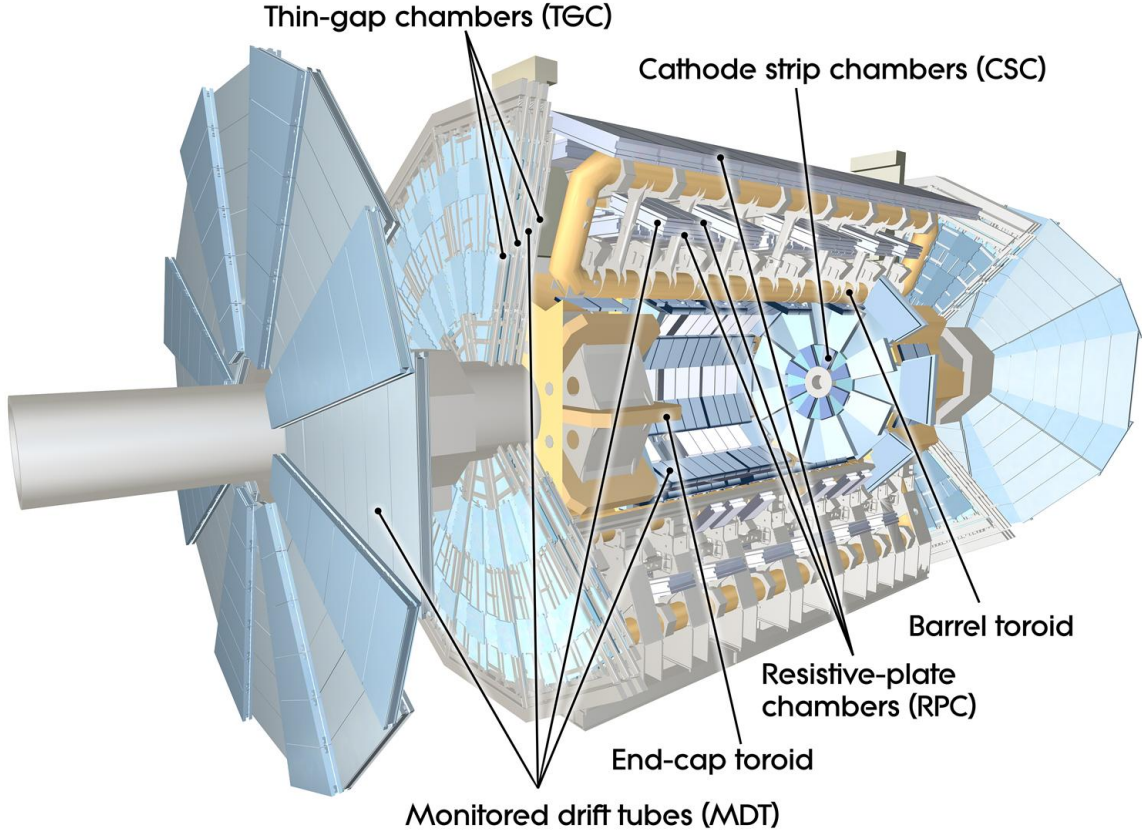


Figure 4.11: Overview of the Muon System

to the higher level L2 trigger in the form of Regions Of Interest (ROIs). The L2 trigger is based on physics signatures, defined by a collection of detector signals that constitute a potential object, for example, a track and electromagnetic cluster for an electron. To test the pre-programmed signatures, the L2 trigger farm requests detailed information within the ROIs as defined by L1 from all detectors as needed.

Finally, if satisfactory physics signature is found by the L2 trigger all the detector information is read out and the standard offline reconstructions are used to build the entire event at which stage energy thresholds can be evaluated with fully reconstructed objects and final decision as to whether the event should be recorded can be made. This level of processing requires about 4s per event and the rate for accepting events at this final trigger level should be kept below 200Hz.

Chapter 5

Object definition and calibration

This analysis selects events based on the reconstructed electrons, muons, missing energy, small- R and large- R jets as well as the presence of jets associated with a b -quark. This chapter reviews the standard reconstruction, identification, efficiencies and calibration of these objects in ATLAS.

5.1 Track and vertex reconstruction

The ATLAS New Tracking [31] includes two track finding sequences, referred to as the *inside-out* and the *outside-in* algorithm. As suggested by the name, the inside-out sequence begins with track seeds in the inner silicon layers obtained by a window search algorithm. In the next step, the seeds are used to define the first iteration of a track trajectory. Next, the algorithm checks if a hit on the next layer out can be associated with this trajectory. If so, the hit is included and the trajectory recalculated including the information from the new hit, and then the search for another hit on the next layer continues. This results in a loose track collection that may have many fake tracks with overlapping hits. An *ambiguity-solver* is employed to clean up the collection by assigning weights to each track, preferring tracks with silicon hits in the innermost layers and larger total number of associated hits. After this step the remaining tracks are extrapolated to the TRT to look for a possible matching TRT extension. Since the inside-out algorithm requires seeds from the silicon layers, it becomes inefficient for tracks originating from secondary vertices or photon conversions. It is therefore supplemented by the outside-in sequence, which starts by looking for track patterns into the TRT and then extrapolates them back to the silicon layers to find short track segments that may have been discarded by the ambiguity-solver.

Since charged particle tracks are bent by the magnetic field, the trajectory takes a helical form and can be expressed by 5 parameters:

- d_0 is the transverse impact parameter, equal to the distance of closest approach

in the plane transverse to the beam of the track to a reference point (this can be either the detector origin or the primary vertex);

- z_0 is the longitudinal impact parameter, equal to the z coordinate of the point of closest approach;
- ϕ_0 is the azimuthal angle of the trajectory at the point of closest approach
- $\cos\theta$ is the cosine of the angle the track forms with respect to the beam
- q/p_T is the charge divided by the momentum in the transverse plane.

Tracks passing basic quality criteria are then combined into vertex seeds by inspecting the z_0 distribution and finding tracks that have similar z_0 values. An iterative vertex fitting algorithm is then used to determine which combinations of tracks provide viable vertices. The resulting vertex with highest $\sum_{trk} p_{T,trk}^2$ is chosen as the Primary Vertex (PV).

5.2 Muons

Muons are reconstructed by combining charged particle tracks found in the Muon Spectrometer and the Inner Detector, while taking into account information on the energy loss in traversing the calorimeters. Tracks in the spectrometer are identified by first looking for segments in each individual layer and then combining the segments. Inner detector tracks are required to pass criteria involving minimum number of hits in all three sub-systems: the Pixel (in particular the innermost layer), the SCT and the TRT. Although, the muon spectrometer can provide a stand alone measurement, to ensure high purity, the muons used in this analysis are required to have matching tracks in both the ID and MS. These muons are referred to as *combined* muons. The final reconstructed muon track is obtained by taking the hits from the ID and MS track segments and performing a combined fit.

The reconstruction efficiency depends on the efficiencies to find an ID track, to find an MS track and to match the two. It is measured using the *tag-and-probe* method. The ID reconstruction efficiency is calculated by selecting events where one muon is identified as a combined muon, referred to as the *tag*, and then a second muon that is only required to have an MS track, the *probe*. The ID reconstruction efficiency is then the fraction of events where the MS track of the probe muon also has an ID track. The exercise can be redone by instead using ID segments as the probe and checking how often there is a matching MS segment, which gives the MS+matching efficiency. The product of the two efficiencies, giving the overall reconstruction efficiency, can be compared in data and MC to obtain scale factors (SF), defined as $SF = \epsilon_{data}/\epsilon_{MC}$. The SF can then be used to adjust the MC efficiency to match the data for the various simulation samples needed in the analysis. To ensure high precision, the

SFs are derived in bins of transverse momentum and η in $Z \rightarrow \mu\mu$ and $J/\Psi \rightarrow \mu\mu$ events [32]. The efficiency in data and MC are generally within 1% based on high statistics study of the combined Run I data [33].

In addition, the muon momentum scale and resolution in MC are corrected to match the data. Mismodeling can arise from multiple sources, including inadequate treatment of detector misalignment uncertainties in MC, imperfect knowledge of the magnetic field map, mismodeling of the energy loss in traversing the calorimeter, etc. The corrections and their corresponding uncertainties are derived by comparing the shape of the dimuon mass distribution in data and MC in $Z \rightarrow \mu\mu$ and $J/\Psi \rightarrow \mu\mu$ events. The corrections are $\leq 0.1\%$ [33].

The muon trigger used in this analysis is the logical OR of a 24 GeV trigger with a loose track-based isolation requirement, the sum of the p_T of tracks within a cone of $\Delta R=0.2$ must be less than 12% the p_T of the muon, and a 36 GeV non-isolated trigger. The muon trigger efficiency and its uncertainty are again estimated by the tag and probe method. Different processes are used to understand the efficiency for different p_T ranges, specifically, $Z \rightarrow \mu\mu$ events for muon $p_T < 100$ GeV and top or $W+jets$ events for higher p_T . In the case of the dimuon events, one triggered muon is used as the tag and the other is the probe. For top and W events, the tag is provided by the missing energy trigger. The trigger efficiency in the barrel region is derived from $Z \rightarrow \mu\mu$ events is shown in Figure 5.1. The main loss of efficiency is due to uninstrumented regions [34].

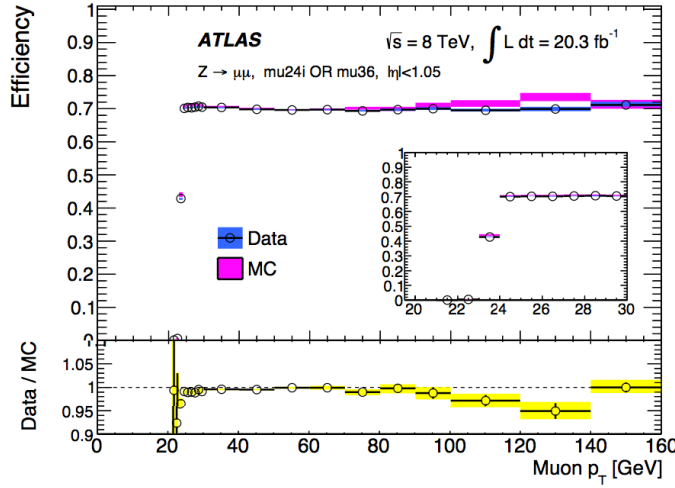


Figure 5.1: Muon trigger efficiency [34].

5.3 Electrons

Electrons are reconstructed based on the combination of energy deposits in the EM calorimeter and tracks reconstructed by the ID. The reconstruction starts with finding cluster seeds. The calorimeter is separated into towers, each measuring 0.025×0.025 in the $\eta - \phi$ plane. Towers are grouped into 3×5 windows and a "sliding-window" algorithm adjusts the position of the fixed size window until the energy it contains is a local maximum. In the next step, charged particle tracks reconstructed in the ID are extrapolated to the middle layer of the calorimeter. If a track and a cluster center lie within $\Delta\eta < 0.05$ and $\Delta\phi < 0.1$, the two are considered a match. The larger matching distance in the ϕ direction is to account for bremsstrahlung. If no track points to the cluster or a pair of closeby tracks are associated with it, then it would be considered as photon candidate. Otherwise, the cluster is considered an electron candidate and the seed cluster is expanded to a pre-optimized size specific to each the barrel and the endcap regions. Finally, to obtain a *reconstructed* electron, corrections are applied to account for energy leakage outside the cluster and for energy lost in the material before the calorimeter.

Reconstructed electrons are further subdivided into *loose*, *medium* and *tight* by imposing additional quality requirements in order to suppress the misidentification of jets, photons or electrons from heavy flavor decays as primary electrons. This analysis uses the tight identification criteria, which include the most stringent requirements on shower shape, hadronic leakage, track quality, tightened track-cluster matching criteria, ratio of cluster energy to track momentum, pixel hit from the inner most layer and TRT identification information. The combined reconstruction and identification efficiency for tight electrons as a function of their transverse energy is shown in Figure 5.2 [35]. Scale factors used to correct the simulation are derived via the tag and probe method in $Z \rightarrow ee$ events.

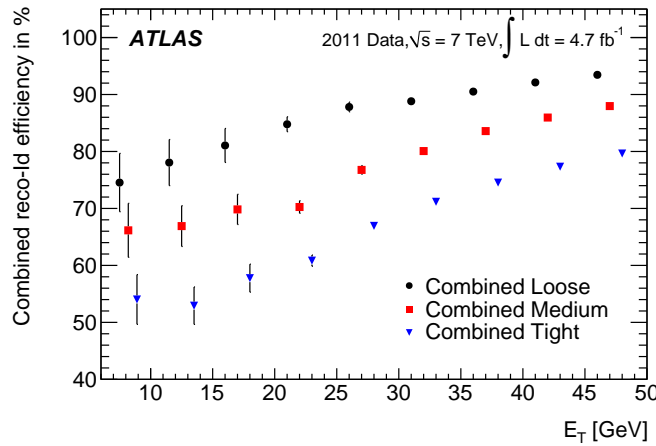


Figure 5.2: Electron reconstruction and identification efficiency [35].

The electron cluster energy is first calibrated based on MC simulation of the electron response. The absolute energy scale and resolution are then compared in data and MC using a large sample of $Z \rightarrow ee$ events. Comparison of the Z invariant mass line shape in data and MC are used to obtain the final corrections to the scale and resolution. The results are cross-checked an independent sample of $J/\Psi \rightarrow ee$ events. The uncertainty on the calibration is below 0.05% across the full p_T range [36].

The electron trigger used in this analysis is the logical OR of a 24 GeV an isolated trigger and a 60 GeV non-isolated trigger. To satisfy the isolation requirement, the sum of the p_T of tracks within a cone of $\Delta R=0.2$ must be less than 10% the p_T of the electron. Both triggers take into account shower shape, hadronic calorimeter leakage, track quality and track-cluster matching criteria. In addition, the 24 GeV trigger has a loose track-based isolation criteria to reduce fake rates at low p_T . Their efficiency is measured using tag-and-probe in $Z \rightarrow ee$ events, where the tag is a tight electron matched to a trigger with a lower threshold and the probe is an oppositely charged electron such that the ee system has invariant mass within the Z mass window of 80-100 GeV. The measured efficiency is shown in Figure 5.3. The uncertainty of the trigger scale factors is obtained by propagating uncertainties on the identification of the tag and varying the boundaries of the Z mass window [37].

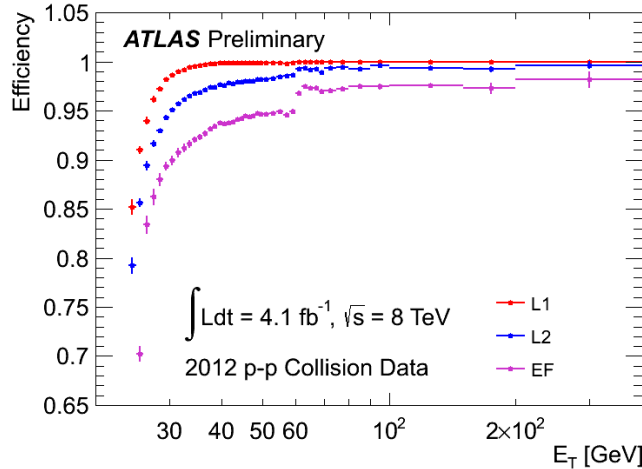


Figure 5.3: Combined efficiency of the 24 GeV and 60 GeV electron triggers [38].

5.4 Small- R jets

Jet reconstruction begins by building and calibrating *topo-clusters* from the EM and hadronic calorimeter cells. The clusters are formed by starting with a seed cell with energy of at least 4σ , where σ is the expected noise, and then recursively adding all neighboring cells with energy above 2σ . Finally, all cells neighboring the

outside edge of the cluster in the previous step are also added. The 4-vector of the topo cluster is defined by the sum of the energies of all its cells, zero mass and a direction obtained from the weighted average of the η and ϕ coordinates of the cells. The energy of the cells used to build the topological clusters is recorded at the EM scale, which reflects the energy of particles that deposit their energy in the form of electromagnetic shower. The topo-clusters are then further corrected to account for hadronic energy measurement non-compensation. The corrections are based on the charged and neutral pion response found in simulation and applied to the clusters based on weights reflecting the degree to which a cluster is electromagnetically or hadronically dominated. The cluster type classification is based on cluster shape variables such as longitudinal depth and energy density [39].

The small- R jet collection is then built using the calibrated topo-clusters as input to the anti- k_t algorithm with $R_0 = 0.4$. The jet 4-vector is given by the sum of the 4-vectors of its constituent topo-clusters as determined by the jet finding. The jet reconstruction efficiency is measured both relative to jets built from charged particle tracks in the ID, requiring a matching calorimeter jet for every track jet, and via tag-and-probe method in QCD di-jet events. The inefficiency is found to be 2% in the 20-30 GeV range and non-existent at higher momentum.

At this stage, the effects of pile up are mitigated via a two step correction. First, the jet p_T is corrected by subtracting the quantity $\rho \times A$, where ρ is the energy density in the event calculated from all calibrated topo-clusters within $|\eta| \leq 2$ and A is the catchment area of the jet. This allows for pile up correction that is tailored to both the individual jet and the extent of pile up in the particular event. The residual correction, primarily relevant for the forward region, is based on parametrization of the pile up contamination as a function of pile up activity estimators. This correction is derived from simulation.

After pile-up subtraction, the jets require a final calibration of their direction (so that the jet points to the primary vertex) and energy scale (JES). The energy scale has an MC-based and *in situ* component. The MC JES is derived as a function of energy and pseudorapidity from the ratio of the energy of a detector level jet to the matching truth level jet. The truth level jet collection is built by running the jet finding algorithm at the generator level, with the stable particles in the event record serving as the input. The subsequent *in situ* correction takes advantage of the superior energy measurement for photons and for Z -bosons that decay to electrons and muons by deriving a JES correction based on events in which a jet recoils against a Z or a photon. Due to limited statistics at high p_T , this method can only be used for jets with p_T below 800 GeV. The correction for higher p_T jets is obtained from events where a high p_T jet is balanced by a system of low p_T jets already calibrated in the previous step. The final JES and its uncertainty are based on a combination of the results from the individual *in situ* measurements. The total relative uncertainty in the central region is shown in Figure 5.4 [39]. The jet energy resolution modeling is separately validated via a di-jet balance method. The resolution in data and simulation is found

to be comparable indicating no need for any additional simulation smearing.

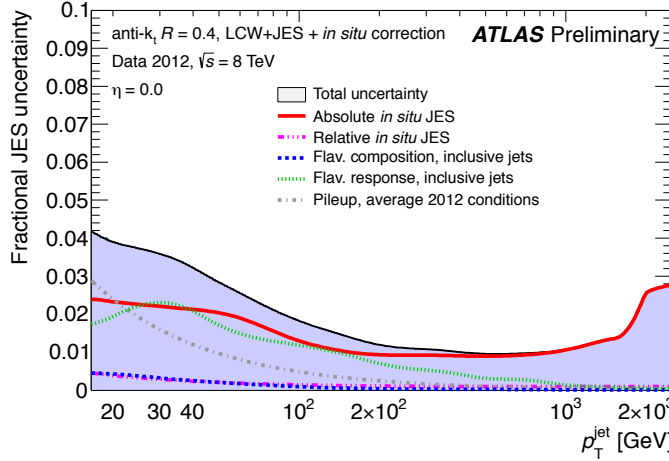


Figure 5.4: Relative small- R JES uncertainty [39].

5.5 Large- R jets

Large- R jets are found starting from the same calibrated topo-cluster collection, but using the anti- k_t algorithm with $R_0 = 1.0$. The jets are then trimmed using the method described in Chapter 2, with the subjet radius set to 0.3 and the subjet energy fraction required to retain the subjet set to 5% of the untrimmed large- R jet energy. In contrast to the small- R jets, the large- R jet calibration is purely simulation based, while *in situ* methods are used to determine the JES uncertainty described later.

A final step when using these jets to identify the collimated decay of a heavy particle is to calibrate the jet mass and the first k_t splitting scale, $\sqrt{d_{12}}$. This step is necessary because the jet energy is less sensitive to soft wide-angle radiation than the jet mass and $\sqrt{d_{12}}$, which renders a JES correction alone insufficient. Similarly to the large- R JES, the jet mass and $\sqrt{d_{12}}$ scales are derived solely from simulation and carry an *in situ*-based uncertainty.

Below 800 GeV the JES uncertainty is found using the same γ -jet balance method as for the small- R jets. The JES uncertainty above 800 GeV as well as the JMS and the $\sqrt{d_{12}}$ scale uncertainties are determined using the track-to-calorimeter ratio method. It relies on the fact that the tracking and calorimeter measurement uncertainties are uncorrelated in order to derive relative uncertainties for the calorimeter jets with respect to the track jets. Here, track jets are built with the same algorithm, but using tracks as the input instead of clusters. Taking as an example the jet mass uncertainty, the method goes as follows. The uncertainty is binned in mass, p_T and m/p_T as it is found that the uncertainty is smaller in regions of these variables that are of particular interest to boosted tops. For each bin the distribution of the ratios

of the calorimeter jet mass to the track jet mass is obtained in both data and MC. Using these, one can form the double ratio:

$$R_m = \left(\frac{m_{\text{calo jet}}}{m_{\text{trk jet}}} \right)_{\text{data}} \Bigg/ \left(\frac{m_{\text{calo jet}}}{m_{\text{trk jet}}} \right)_{\text{MC}} \quad (5.1)$$

The deviation of R_m from 1 gives the relative uncertainty for the bin. This is then added in quadrature to the track based uncertainties due to tracking inefficiency and its impact on the track jet mass. The procedure is repeated to determine the uncertainties for the jet p_T scale above 800 GeV and $\sqrt{d_{12}}$ using the corresponding mass and $\sqrt{d_{12}}$ double ratios [23].

The above methods for deriving the uncertainties are based on inclusive samples dominated by light quark or gluon jets. An additional topology uncertainty is necessary when attempting two describe jets containing boosted tops. It is estimated by comparing the response for jets initiated by a top, a W -boson, a light quark or a gluon and taking the maximum response difference as the uncertainty. It is combined in quadrature with the γ -jet balance or track-to-calorimeter (method depends on the p_T) based JES uncertainties.

A summary of the relative JES and JMS uncertainties for example η and m/p_T bins are shown in Figures 5.5 and 5.6, respectively. The former is the dominant experimental uncertainty for the analysis described in this thesis.

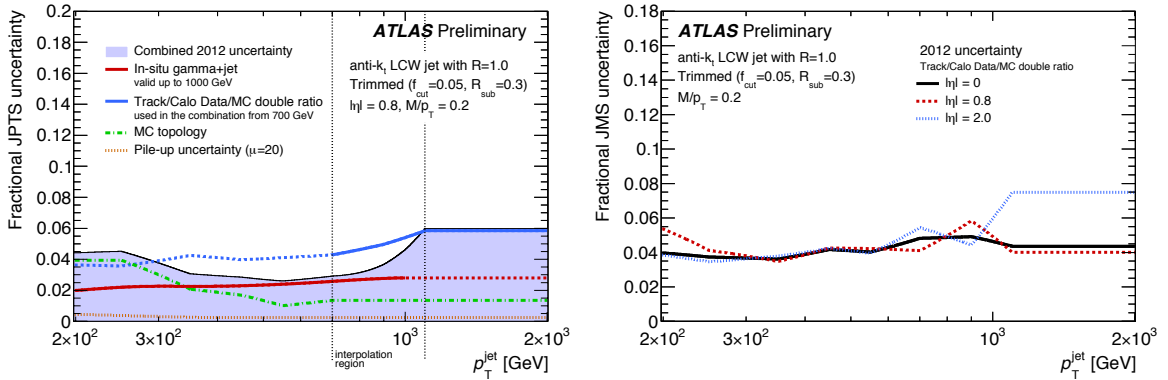


Figure 5.5: Large- R JES uncertainty [23] Figure 5.6: Large- R JMS uncertainty [23]

Since *in situ* tests of small- R jets shows good resolution modeling, the p_T and mass resolution are taken from simulations and the uncertainty is determined by varying the detector geometry, the hadronic interactions model and MC generator. Based on these studies an uncertainty on the resolution is found to be 20% [40].

5.6 B-tagging

Upon hadronization b-quarks form B-hadrons. Thanks to their relatively long lifetime of approximately 1.5 ps, B-hadrons travel a distance of $\mathcal{O}(\text{mm})$ before decaying, which results in a secondary vertex, displaced with respect to the primary interaction vertex (PV). Over time many increasingly sophisticated algorithms have been developed to exploit this feature to identify b-quark initiated jets, referred to as *b-tagging*. All of these are based on reconstructed tracks and vertices information at various levels of detail. The main ideas are summarized below, while further information can be found in [41] and [42].

This analysis relies on the output of the ATLAS MV1 b-tagging algorithm, which is an artificial neural network combining the discriminating power of three of its predecessor algorithms. These can be described as follows:

- The *IP3D* algorithm exploits the transverse, d_0 , and the longitudinal, z_0 impact parameters of tracks associated with the b-jet candidate. Since d_0 and z_0 are measured with respect to the PV, tracks coming from a B-hadron decay will have a larger impact parameter. Their limited resolution is taken into account by using their significances, $d_0/\sigma(d_0)$ and $z_0/\sigma(z_0)$, instead of the raw values. Finally, since these variables are expected to have a distinct correlation pattern for b-jets, the 2D distribution of $d_0/\sigma(d_0)$ vs. $z_0/\sigma(z_0)$ for all tracks in the jet is constructed. Using a likelihood ratio method, the IP3D algorithm then assigns a b-tag weight to the candidate jet by comparing the 2D distribution obtained from its tracks against template distributions for light- and b-initiated jets derived from simulation.
- The *SV1* algorithm attempts to reconstruct all possible two track vertices. It then rejects the candidates that have mass consistent with K_s or Λ decays as well as vertices within one of the silicon layers likely associated with material interactions. Next, it combines the remaining 2 track vertices into a single secondary vertex. Finally, the secondary vertex mass, the ratio of energy from tracks associated with the secondary vertex to all the jet tracks, the number of 2-track vertices and the direction of the line joining the primary and secondary vertex with respect to the jet axis are employed in a likelihood ratio technique to assign a b-tagging weight.
- The *JetFitter* algorithm attempts to reconstruct the characteristic PV, b-vertex, c-vertex decay chain using a Kalman filter. The advantage is that it can separately identify the b and c vertex, which would otherwise be merged by the procedure employed by SV1 for example. JetFitter then uses the same variables as SV1 in addition to flight length significance as inputs to a neural network in order to obtain the probabilities that the jet is a light-, c- or b-initiated.

To ensure that the performance of the combined MV1 algorithm [43] in simulation matches data, the output is calibrated for specific operating point efficiencies. This analysis uses the 70% b-tagging efficiency operating point. The calibration is again accomplished by applying scale factors to the simulation based on studies of the performance in data. The final scale factors come from the combination of the results of three different calibration methods:

- The *system8* [44] method works by solving for the b-tagging efficiency starting from 8 coupled linear equations relating the expected and observed number of events obtained from three independent event selections designed to have significant b-tag purity.
- In the *tag-and-probe* method the efficiency is measured in a dilepton $t\bar{t}$ sample. The *tag* is simply a *b*-tagged jet. The efficiency is obtained by checking if a second jet, the *probe*, is *b*-tagged. The probe must have high purity for this method to provide unbiased results. For $t\bar{t}$ events assigning the probe is complicated by the presence of additional non-*b*-jets from initial and final state radiation as well as the limited detector acceptance. To avoid these complications, the events are required to have exactly two jets in approximately back-to-back topology.
- The *kinematic selection* [42] method is again based on $t\bar{t}$ enhanced sample, specifically in the $e\mu$ dilepton channel for increased purity. It solves for the b-tagging efficiency from the number of *b*-tagged events in data and the number of predicted mistagged jets (light-quark or gluon jets identified as *b*-jets by the algorithm). The latter is obtained based on knowledge of the fraction of non-*b*-jets from simulation combined with the calibrated misidentification rate (obtained in a separate set of data analysis not described here).

As an example, the comparison of the efficiency found in data and MC using the kinematic selection method is shown in Figure 5.7. The ratio of the two curves gives the scale factors applied to simulation along with their uncertainties. The scale factors for the small number of *b*-jets with p_T above 300 GeV are taken from the last measured bin.

5.7 Missing energy

The missing transverse energy, E_T^{miss} , represents the momentum imbalance in the transverse plane, which in the absence of unknown particles that may escape detection is attributed to neutrinos. The measurement of missing energy is made possible by the near hermetic coverage of the calorimeter system up to $\eta < 4.5$. The main challenges in determining the E_T^{miss} come from cracks in the coverage due to inactive detector modules, imperfect resolution, the remaining uncovered region above $\eta=4.5$ and fake contributions due to cosmic muons traversing the detector.

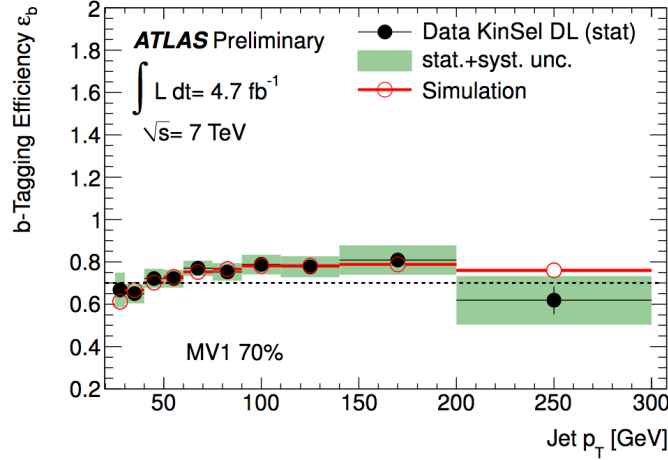


Figure 5.7: B-tagging efficiency [42].

E_T^{miss} reconstruction is based on combining information from all subsystems. The tracker supplies the energy associated with low momentum tracks that curve sufficiently in the magnetic field, so that they never exit the ID and the energy of muons that are not reconstructed in the spectrometer. The muon spectrometer is used to provide the contribution from muons and the remaining information is taken from the calorimeters. To avoid introducing fake contributions, the calorimeter term is constructed using fully calibrated objects. Finally, the E_T^{miss} soft term is given by topo-clusters not associated with any reconstructed object. These are added at the hadronic scale, unless they are matched to a track in which case the track momentum is used instead.

The uncertainty on the missing energy [45] comes from varying the scale and resolution uncertainties of each of the reconstructed objects used to rebuild it in addition to the scale and resolution uncertainty of the soft term. The former were described in the previous sections, the latter is derived separately as follows. Using a sample of $Z \rightarrow \mu\mu$ events without any jets above 20 GeV, the projection of the E_T^{miss} along the direction of the Z in the transverse plane is compared between data and MC. The deviation from unity is taken as estimate of the scale uncertainty. The results are cross-checked by an alternate method using balancing real E_T^{miss} with hard objects. The uncertainty is of order few percent and it has insignificant impact in this analysis.

Chapter 6

Event selection

The event selection used in this analysis has been specifically designed to have high efficiency for selecting lepton + jets $t\bar{t}$ events in the boosted topology, while maintaining good background rejection. It was originally developed for the ATLAS $t\bar{t}$ resonances search [46]. A detailed summary is given in Table 6.1, where the detector level selection is shown together with the particle-level fiducial region for the cross-section measurement. The latter will be discussed further in Chapter 9.

Cut	Reconstructed level		Particle level
	Electrons	Muons	
Preselection	Event quality; Single lepton trigger; GRL; Vertex		None
Leptons	$\ z_0\ < 2.$ $\text{miniso}/p_T(l) < 0.05$ $ \eta < 2.47$ (- crack) $p_T > 25 \text{ GeV}$	$\ z_0\ < 2. \& d_0/\sigma(d_0) < 3.$ $\text{miniso}/p_T(l) < 0.05;$ $ \eta < 2.5$ $p_T > 25 \text{ GeV}$	$ \eta < 2.5$ $p_T > 25 \text{ GeV}$
Anti-kT R=0.4 jets	$\text{JVF} > 0.5$ if $p_T(j) < 50 \text{ GeV}$ $p_T > 25 \text{ GeV} \& E > 0$ $ \eta < 2.5$		$ \eta < 2.5$ $p_T > 25 \text{ GeV}$
Overlap removal	$\text{if } dR(e, j) < 0.4: j' = j - e$ $\Delta R(e, j') < 0.2: e \rightarrow 0$	$\text{if } \Delta R(\mu, j') < 0.04 + 10./p_T(\mu):$ $\mu \rightarrow 0$	None
E_T^{miss}, m_T^W	$E_T^{\text{miss}} > 20 \text{ GeV}, E_T^{\text{miss}} + m_T^W > 60 \text{ GeV}$		
Leptonic top	at least one anti-kT R = 0.4 jet, j'^{lep} , s.t. $\Delta R(l, j'^{\text{lep}}) < 1.5$		
Hadronic top	$p_T(J) > 300 \text{ GeV}, m(J) > 100 \text{ GeV}, \sqrt{d_{12}} > 40 \text{ GeV}$ $dR(j'^{\text{lep}}, J) > 1.5, d\phi(l, J) > 2.3$		
B -tagging	At least one of: 1) the leading anti-kT R = 0.4 jet that satisfies $\Delta R(l, j'^{\text{lep}}) < 1.5$ is b -tagged; 2) \exists a b -tagged anti-kT R = 0.4 jet, j , s.t. $\Delta R(j, J) < 1.0$ ("inside" the selected large-R jet)		

Table 6.1: Reconstructed and particle-level selections

The selection begins with the trigger and event quality requirements. The sample is collected using the combination of single lepton triggers described in the previous chapter, with events selected in the $e+jets$ channel required to pass one of the electron triggers and $\mu+jets$ events required to pass one of the muon triggers. Problematic events, such as those containing LAr calorimeter noise bursts or tile calorimeter corrupted data, are rejected. The selected events are also required to have a primary vertex with five or more associated tracks.

The event must contain exactly one *good* lepton, matching the trigger object. This is enforced as follows. First, electron, muon and jet candidates are selected based on kinematic and identification quality criteria. Since electrons and muons deposit energy in the calorimeters, an overlap removal procedure is applied to avoid double-counting leptons and small- R jets. After any duplicates have been removed, the event is required to contain exactly one lepton candidate.

Electron candidates are selected from the subset of reconstructed electrons identified as tight. In addition to the criteria intrinsic to the the tight definition, the electron track is required to have longitudinal impact parameter of less than 2 mm, to ensure it is consistent with the primary vertex. The electron direction is obtained from the associated track if the track has more than 4 silicon hits and from the calorimeter cluster otherwise. The pseudorapidity is required to satisfy $0 < |\eta| < 1.37$ or $1.52 < |\eta| < 2.47$, with the excluded region corresponding to the transition between the barrel and end-cap calorimeter. The minimum transverse momentum is set to 25 GeV, slightly above the trigger threshold, to ensure flat trigger efficiency. Finally, to reject electrons coming from heavy flavor decays, the candidate is required to pass an isolation criteria. Traditionally, in the resolved topology, a simple cone isolation can be used, however, in the boosted case, where the top decay products have become collimated, such an isolation requirement quickly starts to suffer inefficiencies since the isolation cone starts to overlap with neighboring quarks. To solve this problem, the *mini-isolation* variable [47] has been adopted in boosted top analysis. It uses an isolation cone that shrinks as a function of p_T and a maximum energy in the isolation cone that is also p_T dependent. It is defined as:

$$I_{\text{mini}} \equiv \sum_{\text{tracks}} p_T^{\text{tracks}} / p_T^l, \quad (6.1)$$

where p_T is the transverse momentum of the lepton. The sum runs over all tracks within $\Delta R(\text{track}, \text{lepton}) < 10 \text{ GeV} / p_T^l$ that have $p_T > 1 \text{ GeV}$ and satisfy track quality criteria, excluding the lepton candidate track. The track quality cuts include impact parameter and silicon tracker hit requirements designed to minimize sensitivity to bremsstrahlung electrons and pile up. For an electron candidate to be considered isolated I_{mini} must be less than 5%.

Muon candidates are selected from the combined muon collection. Similarly to the electrons, they are required to have longitudinal impact parameter less than 2 mm. In addition, their transverse impact parameter significance must satisfy $d_0/\sigma(d_0) < 3$,

to remove muons from cosmics. This cut also helps suppress muons from heavy flavor decays. To ensure high quality, the muon ID track must also satisfy the following hit requirements:

- at least one pixel hit; if the track crosses a dead pixel sensor, it counts as a missed hit, satisfying this requirement;
- at least 4 SCT hits; similarly, each crossed dead SCT module counts as 1 hit towards satisfying this requirement;
- no more than 2 total pixel and SCT holes, where a hole means there was a hit expected based on extrapolating a track across a layer, but no such hit was recorded;
- a successful TRT extension.

The pseudorapidity of the combined track must be less than $|\eta| = 2.5$. As for the electrons, the transverse momentum minimum is again set to 25 GeV and the mini-isolation required to be less than 5%.

Small- R jet candidates, built as described in the previous chapter, are required to have transverse momentum above 25 GeV. In order to allow the use of the b -tagging algorithm, which is based on tracks, the jet pseudorapidity must be less than 2.5. Additional pile up jet suppression is achieved by cutting on the jet vertex fraction or JVF [48], which is the ratio of the total p_T of tracks associated with both the jet and the primary vertex to the total p_T of all tracks associated with the jet. Jets with $p_T < 50$ GeV are required to have $\text{JVF} > 0.5$. The cut is only applied in the lower p_T region since most pile-up jets are soft. Finally, small- R jets must also satisfy jet quality criteria designed to reject events with high- p_T jets that are not associated with a proton-proton collision. Such jets may result from proton-beam-gas collisions, cosmic ray muons and calorimeter noise. Their identification is based on cell-level energy deposition parameters, energy deposition vs. shower development direction and associated track parameters [39]. If such a jet is present, the entire event is rejected.

The electron-jet overlap removal procedure specifically designed for the boosted topology is as follows. If the distance between the candidate electron and any small- R jet is $\Delta R(e, j) < 0.4$, the electron 4-vector is subtracted from the jet 4-vector and the jet JVF is recalculated removing the electron track. If this e -subtracted jet passes the p_T , η and JVF requirements, it is kept and otherwise rejected. After this subtraction procedure, if the candidate electron is still within $\Delta R(e, j) < 0.2$ of a small- R jet, it is rejected. More details and checks of this procedure are provided in Appendix A. The muon-jet overlap removal procedure removes muons that fall inside a cone of $\Delta R(\mu, \text{jet}) < 0.04 + (10 \text{ GeV}/p_T^\mu)$ around a small- R jet passing the jet requirements. The p_T -dependent radius is used to increase the reconstruction efficiency for boosted kinematics.

To take advantage of the knowledge that the event must contain missing energy from the neutrino, the E_T^{miss} is required to be greater than 20 GeV. The E_T^{miss} -lepton system should also be consistent with coming from a W -boson, which is exploited by first defining the W transverse mass as:

$$m_T^W = \sqrt{2 p_T E_T^{miss} (1 - \cos \Delta\phi)}, \quad (6.2)$$

where $\Delta\phi$ is the azimuthal angle between the lepton and the missing energy and then requiring $E_T^{miss} + m_T^W > 60$ GeV.

Since the leptonic top decay products are expected to be collimated, a jet corresponding to the b -quark should be in the vicinity of the lepton. Therefore, at least one small- R jet per event is required to satisfy $\Delta R(\text{jet}, \text{lepton}) < 1.5$. If there is more than one such jet, the highest p_T one is taken as the leptonic side b -jet candidate.

Next, the event must contain a valid top-jet candidate. To begin, at least one large- R jet with transverse momentum greater than 300 GeV is required. Since this jet is expected to contain the hadronically decaying top quark, its reconstructed mass is required to be greater than 100 GeV. The fact that the $R = 1.0$ jets should contain at least two or three high- p_T sub-jets is exploited by requiring that the first k_t splitting scale $\sqrt{d_{12}}$ be greater than 40 GeV. The mass and $\sqrt{d_{12}}$ cuts are primarily targeted at rejecting events originating from the production of a W -boson in association with jets. In these events, the E_T^{miss} and W transverse mass are satisfied by definition and therefore their most distinguishing feature is the large- R jet substructure. If the large- R jet is formed by a system of light-quark jets balancing the W -boson these can easily fake a top-jet despite these cuts. If instead the W is balanced by a high- p_T jet initiated by a single light-quark, its mass and $\sqrt{d_{12}}$ would tend at low values as discussed in Chapter 2 and these cuts will provide good rejection.

Two event topology cuts are enforced in order to further ensure that the large- R jet indeed corresponds to the hadronic top. Since there is no overlap removal between leptons and large- R jets, these cuts ensure that the top-jet candidate does not come from the leptonic top. This is especially important in the electron channel where the electron energy deposited in the calorimeter is not vetoed during topo-cluster formation. The combination of topo-clusters corresponding to the electron and the b -jet would then also provide the necessary substructure to fake a hadronic top. To prevent this, the large- R jet is required to be well separated from the lepton candidate, $\Delta\phi(\text{jet}_{R=1.0}, l) > 2.3$, and from leptonic side b -jet candidate, $\Delta R(\text{jet}_{R=1.0}, \text{jet}_{R=0.4}) > 1.5$. Hereafter, the highest p_T large- R jet that satisfies all above requirements is considered the hadronic top-jet candidate.

To further reduce backgrounds, at least one of the top candidates (leptonic or hadronic) must have an associated b -jet. This is satisfied if there exists at least one b -tagged small- R jet within the hadronic top-jet, i.e. $\Delta R(\text{jet}_{R=1.0}, \text{jet}_{R=0.4}) < 1$, or the leptonic side b -jet candidate as previously defined is b -tagged.

The most stringent requirements come from the lepton and top-jet candidate. As an example, the percentage of selected events at various stages of the event selection

Stage in event selection	Retained events
Exactly one good lepton	43 %
E_T^{miss} and m_T^W requirements	37 %
A small- R jet in the vicinity of the lepton	23 %
A top-jet candidate	0.6 %
b -tagging requirement	0.5 %

Table 6.2: Percentage of events retained at various stages of the event selection. The values are based on a test sample of 15,000 semi-leptonic $t\bar{t}$ events.

based on a test sample of 15,000 semi-leptonic $t\bar{t}$ events is shown in Table 6.2. The lepton requirement leaves less than half of the events. After the large- R jet requirements the sample is reduced to less than 1% of the original count. For the full 8 TeV pp -collision dataset, the total numbers of selected events in data are 4148 in the $e+jets$ channel and 3604 in the $\mu+jets$ channel. Based on these events, the $t\bar{t}$ cross-section is measured as a function of the p_T of the hadronic top-jet candidate.

Chapter 7

Detector-level modeling

The stringent requirements on the lepton quality, the presence of missing energy, the presence of jet substructure and the use of b -tagging in the event selection allow to obtain a very clean $t\bar{t}$ sample. As can be seen in Figure 7.3 (to be discussed more shortly), approximately 90% of the selected events come from single and dilepton $t\bar{t}$ production. The remaining 10% are shared between $W+jets$, single top, multijets, $Z+jets$ and dibosons. This chapter describes how the background predictions are obtained and presents the comparison between the total prediction and the data at the detector level.

7.1 Data-driven background predictions

Since theoretical predictions of the $W+jets$ and Multijet backgrounds suffer from sizable theoretical uncertainties their contributions are, to a varying extent, extracted from data. To indicate this, the $W+jets$ and Multijet backgrounds are labeled as *data-driven*. Since this analysis uses the same event selection as the ATLAS $t\bar{t}$ resonance search, the data-driven estimates produced by the resonance search group are used here directly. This section summarizes the methods used for their extraction. More details can be found in Ref. [49, 46].

7.1.1 $W+jets$

$W+jets$ is the dominant background. In particular, the production of W -boson in association with heavy flavor jets results in events that are particularly hard to discriminate from $t\bar{t}$ due to the presence of a real W , satisfying all lepton and E_T^{miss} cuts, and heavy flavor jets, satisfying the b -tagging requirement. The large- R jet can be faked by a system of quarks recoiling from the W . Theoretical predictions of the total $W+jets$ production rate for events with multiple additional jets as well as the fraction of events corresponding to $W+c$, $W+b\bar{b}$ and $W+c\bar{c}$ production carry large

uncertainties. For this reason, W +jets simulation, provided by ALPGEN+HERWIG, is used only after applying normalization and heavy flavor fraction (HFF) scale factors which bring these quantities in agreement between data and MC.

The overall W +jets normalization is determined by exploiting two facts: 1) the number of W^+ +jets events is higher than that of W^- +jets events in pp -collision, a charge asymmetry caused by the higher density of up quarks than down quarks in the proton and 2) the ratio of W^+ +jets to W^- +jets production has smaller theoretical uncertainties than the total production. To exploit these observations, the number of W +jets events is expressed in terms of the charge asymmetry found in data as follows:

$$N^{W^+} + N^{W^-} = \left(\frac{r_{MC} + 1}{r_{MC} - 1} \right) (D^+ - D^-) \quad (7.1)$$

Here, $N^{W^+} + N^{W^-}$ are the total number of W +jets events, r_{MC} is the ratio of the theoretical cross-sections for $W^+ + jets$ and $W^- + jets$ production, and $D^+ - D^-$ is the charge asymmetry in data. The normalization is first obtained in the larger sample before applying a b -tag requirement and then the HFF, described next, are used to obtain the normalization in the tagged sample.

The HFF scale factors are extracted from a sample of events selected using the same lepton and E_T^{miss} requirements and exactly 2 jets. The results are extrapolated to higher jet multiplicities characteristic of this analysis using simulation. The HFF in the 2-jet bin are determined by enforcing a relation between the events with and without b -tag found in data:

$$N_{W^\pm}^{tag} = N_{W^\pm}^{pretag} (F_{bb} P_{bb} + F_{cc} P_{cc} + F_c P_c + F_{light} P_{light}) \quad (7.2)$$

Here, $N_{W^\pm}^{tag}$ and $N_{W^\pm}^{pretag}$ are the numbers of events before and after applying a b -tag, respectively, that are found in data in a W +jets dominated control region after any background has been subtracted; F_{bb} , F_{cc} , F_c and F_{light} are the 2-jet bin HFF; and P_{bb} , P_{cc} , P_c and P_{light} are the b -tagging probabilities obtained from simulation. Since the charge asymmetry for $W+b\bar{b}$, $W+c\bar{c}$ and $W+light$ differ from the one for $W+c$ sample the events that contain positively and negatively charged lepton can be used separately to obtain two constraints. The difference is due to the fact that at LO $W+c$ events result from $g-s$ and $g-\bar{s}$ scattering which is an equally probable initial state as there are no valence strange quarks in the proton. The other three processes result from $u-d$ -type scattering and therefore inherit the asymmetry associated with the u and d proton PDFs. Having 4 HFF, means that 2 more constraints are needed. These come from the requiring that the HFF add up to 1 and constraining the ratio F_{bb}/F_{cc} to the value found in simulation. Having determined the HFF in the 2-jet bin, they are extrapolated to the higher jet multiplicities using simulation.

The systematic uncertainty associated with the charge asymmetry normalization and HFF scale factors are broken down into components corresponding to varying the multijet background (described next), experimental uncertainties, PDFs as well

as using the NLO prediction for the charge asymmetry (as opposed to the NNLO prediction used in the nominal scale factor derivation).

In addition, the $W+jets$ shape uncertainty is obtained by measuring the impact of varying the **ALPGEN** generator settings of the functional forms of the renormalization and factorization scales as well as the matrix element to parton shower matching scale.

7.1.2 Multijet

Multijet events may occasionally mimic the signal if a non-prompt lepton coming from a heavy flavor quark decay is identified as prompt or in the case of electrons, if there is a jet with a high electromagnetic fraction. Even though the rate of selecting such electrons is low, their contribution is measurable thanks to the large multijet production cross-section in pp -collisions. Since the theoretical prediction of the cross-section in such a limited phase space comes with sizable uncertainties, the multijet background must be derived from data. This is achieved using the Matrix Method [50]. To begin, two data samples are defined, one equivalent to the event selection used in the analysis, referred to as *tight*, and the other keeping all cuts but only loosening the lepton criteria, referred to as *loose*. Loose muons are defined by removing the isolation to allow selection of more non-prompt muons. For loose electrons, in addition to removing the isolation, the electron track quality and track-cluster matching criteria are also loosened to allow contributions from jets faking the electron. The number of events in the tight and loose sample can be expressed as:

$$N_{\text{loose}} = N_{\text{loose}}^{\text{prompt}} + N_{\text{loose}}^{\text{non-prompt}} \quad (7.3)$$

$$N_{\text{tight}} = N_{\text{tight}}^{\text{prompt}} + N_{\text{tight}}^{\text{non-prompt}} = \epsilon \times N_{\text{loose}}^{\text{prompt}} + f \times N_{\text{loose}}^{\text{non-prompt}} \quad (7.4)$$

Here, $N_{\text{loose}(\text{tight})}^{\text{prompt}(\text{non-prompt})}$ refers to the number of events where a prompt (non-prompt) lepton passes the loose (tight) selection criteria; ϵ is the efficiency for a prompt electron to pass the tight criteria, derived from $Z \rightarrow ll$ events; and f is the rate for a non-prompt lepton to pass the tight criteria, calculated from a sample enriched in multijet events which is obtained by inverting the E_T^{miss} and m_T^W cuts (and also $d_0/\sigma d_0$ for muons). Then, given the two constraints and only two unknowns, $N_{\text{loose}}^{\text{prompt}}$ and $N_{\text{loose}}^{\text{non-prompt}}$, the multijet background can be calculated.

The systematic uncertainty on the data-driven multijet estimate is studied by varying the definition of the loose leptons, changing the selection used to form the control region used to derive the fake rate, and propagating the statistical and systematic uncertainties on the parameterizations of the efficiency and the fake rate. The resulting total uncertainty on the multijet background is 19.4% and 18.9% in the electron and muon channel, respectively.

7.2 MC-based predictions

Top quark pair events are modeled by a sample generated with the PowHEG NLO generator [19] using the CT10 [10] PDF set from the CTEQ collaboration. Parton shower and hadronization are simulated using the PYTHIA [14] program. The sample is normalized to the NNLO+NNLL cross-section, which includes the perturbative partonic cross-section to $\mathcal{O}(\alpha_S^4)$ and the logarithmic enhancements of the cross-section from soft gluon emissions to next-to-next-to-leading-log. Additional scale factors are also applied to account for cross-section depletion due to electroweak corrections [51, 52, 53]. This $t\bar{t}$ sample, hereafter referred to as PowHEG+PYTHIA, is used to model the detector response for single lepton $t\bar{t}$ events when unfolding the data. It also provides the estimate of the dilepton background.

Single-top events are separated in three channels depending on the production mechanism, depicted in Figure 7.1. The Wt -channel accounts for $\sim 75\%$ of the single top contribution to this selection. The t -channel production is simulated using the ACERMC [54] generator, while the s -channel and the $W + t$ associated production are modeled by PowHEG, with the shower provided by PYTHIA in both cases. The cross-sections are normalized to the NLO+NNLL calculations. The symmetrized theoretical normalization uncertainties are 4% [55] for s -channel, 4% [56] for t -channel and 7% [57] for Wt -channel. Adding the uncertainties in quadrature according to the size of the contribution results in a total normalization uncertainty of 5.4%, which is propagated through the full analysis. In addition, a shape uncertainty for the largest Wt -channel is estimated by comparing the nominal PowHEG distributions to those obtained from samples generated with MC@NLO.

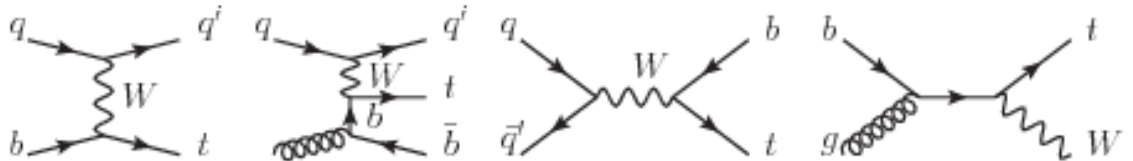


Figure 7.1: Single-top production in the t -channel (1st and 2nd diagram from the left), the s -channel (3rd diagram) and the Wt -channel (right-most diagram) [26].

Events from diboson, WW , WZ and ZZ , and Z +jets production give only very small contributions, $<0.5\%$. The diboson production is modeled using SHERPA [58] and normalized to the NLO cross-sections. The Z +jets is modeled using the ALPGEN generator and HERWIG parton shower and hadronization. The Z +jets and diboson backgrounds are assigned a conservative normalization uncertainty of $\pm 50\%$, with negligible effects on the reported $t\bar{t}$ cross-section.

7.3 Systematic uncertainties at detector level

The uncertainties associated with the reconstruction and calibration of each object, described in Chapter 5, are propagated through the analysis by re-running the event selection after applying efficiency scale factors/calibrations/ resolutions corresponding to a 1σ deviation with respect to their nominal values. The selection is rerun individually for each uncertainty source, separately for a deviation of $+1\sigma$ and -1σ . These uncertainties are propagated as fully correlated between all MC samples.

The background uncertainties described in the previous section affect only the specific background. They are added in quadrature to the total uncertainty on the prediction.

The complete list of uncertainties considered at the detector level, including all the object uncertainties described in Chapter 5, is as follows:

- **Large- R jets:** jet energy, mass and $\sqrt{d_{12}}$ scale; jet energy and mass resolution;
- **Small- R jets:** jet energy scale and resolution; jet reconstruction efficiency; JVF scale;
- **Heavy flavor tagging:** b -tagging efficiency and mistag rates;
- **Leptons:** identification, reconstruction, isolation and trigger efficiencies; momentum calibration and resolution;
- **Missing transverse energy:** scale and resolution of the E_T^{miss} soft term;¹
- **Backgrounds:** shape and normalization as described in the previous section; uncertainty due to limited statistics of the samples used to derive the backgrounds;
- **Luminosity**

Uncertainties on the $t\bar{t}$ modeling and cross-section are not included at the detector level as the aim of this analysis is to measure the $t\bar{t}$ contribution. Effect of the $t\bar{t}$ modeling on the data unfolding will be described in Chapters 9 and 10.

The contribution of each uncertainty source as a function of the top-jet p_T , the distribution to be unfolded, is shown in Table 7.1. The uncertainty grows with top-jet p_T from approximately 13% to 23%. The main contributions come from the top-jet energy scale and b -tagging.

¹Additional contributions to the E_T^{miss} uncertainty coming from the imperfect knowledge of object calibration are included under the uncertainty on the object, since the E_T^{miss} is recalculated in each event using the calibrated objects in that particular iteration of the event selection.

RECONSTRUCTED SPECTRUM - $l+\text{jets}$ ($e + \mu$)								
Uncertainty[%] / Bins [GeV]	300-350	350-400	400-450	450-500	500-550	550-650	650-750	750-1200
Large- R jet momentum scale	13/-10	8.1/-9.0	11/-6	10/-14	9/-11	9/-10	17/-16	17/-13
Large- R jet momentum resolution	1.5/-1.5	1.1/-1.1	3.9/-3.9	1.1/-1.1	0.0/-0.0	0.4/-0.4	1.8/-1.8	1.4/-1.4
Large- R jet mass and $\sqrt{d_{12}}$	3.5/-3.8	2.8/-2.7	2.2/-2.2	1.7/-2.1	1.7/-1.7	1.8/-2.1	2.1/-2.3	2.8/-3.3
Small- R jets	0.9/-1.1	0.8/-0.9	0.4/-0.9	1.1/-2.3	1.6/-2.9	2.0/-0.5	3.2/-2.2	2.6/-1.8
Heavy flavor tagging	1.9/-2.0	2.6/-2.6	3.1/-3.1	3.7/-3.7	3.8/-4.0	4.9/-5.2	6.8/-7.8	6.5/-9.5
Lepton	1.4/-0.9	1.5/-0.9	1.7/-0.9	1.9/-0.9	2.1/-0.9	2.4/-0.9	2.6/-0.9	3.0/-1.0
Missing transverse energy	0.2/-0.2	0.0/-0.2	0.0/-0.3	0.0/-0.4	0.1/-0.1	0.2/-0.2	0.0/-0.5	0.4/-0.1
MC generator/Fragmentation	0.4/-0.4	0.4/-0.4	0.5/-0.5	0.5/-0.5	0.5/-0.5	0.6/-0.6	0.6/-0.6	0.6/-0.6
Initial/Final state radiation	0.0/-0.0	0.0/-0.0	0.0/-0.0	0.0/-0.0	0.0/-0.0	0.0/-0.0	0.0/-0.0	0.0/-0.0
Backgrounds	0.7/-0.9	0.8/-1.0	0.9/-1.1	0.8/-1.1	1.7/-1.9	2.1/-2.3	1.9/-2.2	2.3/-3.0
Luminosity	2.8/-2.8	2.8/-2.8	2.8/-2.8	2.8/-2.8	2.8/-2.8	2.8/-2.8	2.8/-2.8	2.8/-2.8
MC statistics	0.0/-0.0	0.0/-0.0	0.0/-0.0	0.0/-0.0	0.0/-0.0	0.0/-0.0	0.0/-0.0	0.0/-0.0
Statistical uncertainty	1.8/-1.8	2.3/-2.3	3.0/-3.0	3.9/-3.9	5.5/-5.5	5.5/-5.5	9.3/-9.3	12/-12
Total systematic uncertainty	14/-11	10/-10	13/-9	12/-15	11/-13	11/-12	19/-18	20/-17

Table 7.1: Impact of the different uncertainty sources on the total prediction in bins of top-jet transverse momentum (evaluated for the sum of the two decay channels).

7.4 Comparison of data to prediction

Having evaluated the backgrounds and the systematic uncertainties the data to simulation agreement is assessed at the detector level. The prediction is built by summing the contributions from all the backgrounds with the single-lepton $t\bar{t}$ model obtained from PowHEG+PYTHIA. The uncertainty on the prediction is the combination of the systematics described in the previous section. Table 7.2 gives the number of expected events for each process as well as a comparison of the total prediction to the observed number of events. The prediction is generally found to overestimate the data by approximately 1σ (this would be further improved when the $t\bar{t}$ modeling uncertainties are taken into account).

	$e+\text{jets}$	$\mu+\text{jets}$
$t\bar{t} \ell+\text{jets}$	4020 ± 460	3500 ± 400
$t\bar{t}$ dilepton	227 ± 36	210 ± 26
$W+\text{jets}$	263 ± 50	252 ± 48
single top	136 ± 27	134 ± 25
Multijet	91 ± 17	3 ± 1
$Z+\text{jets}$	34 ± 18	14 ± 8
Dibosons	22 ± 11	18 ± 9
Prediction	4790 ± 540	4130 ± 470
Data	4148	3604

Table 7.2: Observed and expected number of events in the signal $e+\text{jets}$ and $\mu+\text{jets}$ samples.

The data-to-prediction agreement is validated further by studying the distributions of several variables of interest.

Starting with the leptonic side, the p_T of the selected lepton, the E_T^{miss} and the m_T^W are shown in Figure 7.2. While the prediction generally overestimates the data, as already observed from Table 7.2, the shape of the E_T^{miss} and m_T^W is generally well modeled by the simulation. The lepton p_T appears softer in the data compared to simulation. Since this effect appears more pronounced in the $\mu+jets$ channel, it has been verified that the two channel results are consistent within the statistical and uncorrelated systematic uncertainties (for more details, see Appendix B).

On the hadronic side, the top-jet mass and first splitting scale, $\sqrt{d_{12}}$, shown in Figure 7.3, appear well modeled. As would be expected for a top, the mass peaks at ~ 170 GeV. The large tail to lower masses corresponds to less boosted tops, where one of the quarks or some portion of the final state radiation associated with the top was not captured in the large- R jet. For a heavy decaying particle the splitting scale should be clustered about half the mass, in this case ~ 85 GeV, as observed in Figures 7.3 (c) and (d).

The top-jet candidate η and p_T are shown in Figures 7.4. In both cases the shape is not well modeled. In the case of the rapidity, again the discrepancy is more prominent in one channel than the other. The η distribution appears narrower in data in the $e+jets$ channel. In the case of the top-jet p_T the disagreement increases with p_T , with the simulation overestimating the data by up to approximately 50% in the highest p_T bin in both channels. Similarly to the case of the lepton p_T , the data-to-MC agreement is compared between the two channels and the results are found to be consistent (for more details, see App. B).

Since events must have a b -jet associated with at least one of the top candidates, the b -jet kinematics and multiplicity are also examined. As shown in Figure 7.5, the distributions of η and p_T are generally well modeled, while the multiplicity tends to larger values in data, however, the deviations remain within uncertainty especially when the $t\bar{t}$ generator modeling is taken into account.

The modeling of the top-jet candidate p_T spectrum is the subject of the present analysis. The observation that the prediction increasingly overestimates the data at high p_T has been reported in previous differential cross-section measurements by both ATLAS [2] and CMS [3, 4]. The boosted top selection utilized here allows to study this effect at higher p_T values than these accessible in the previous measurements.

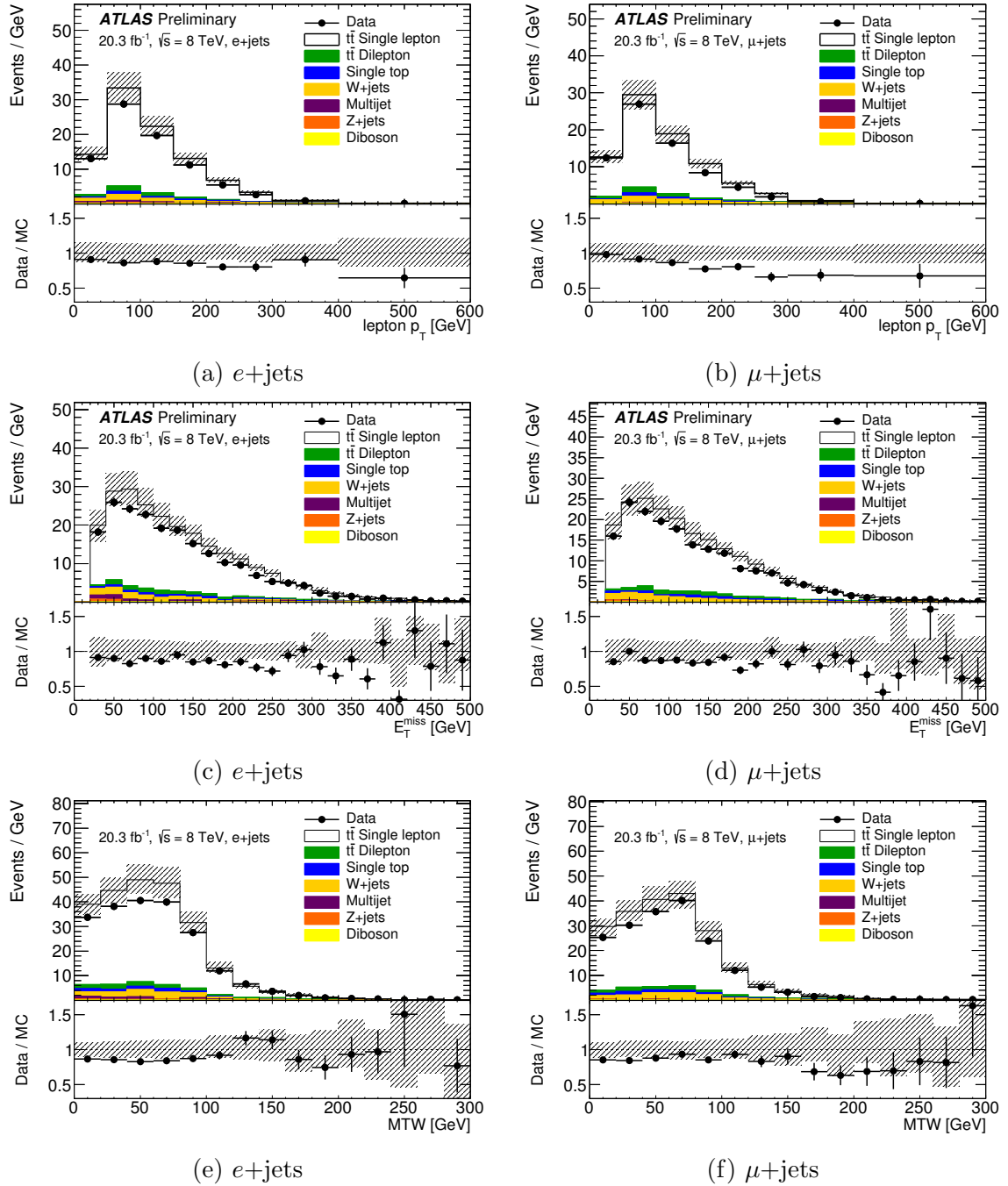


Figure 7.2: Distributions of the p_T of the selected lepton, the missing transverse energy and the W transverse mass.

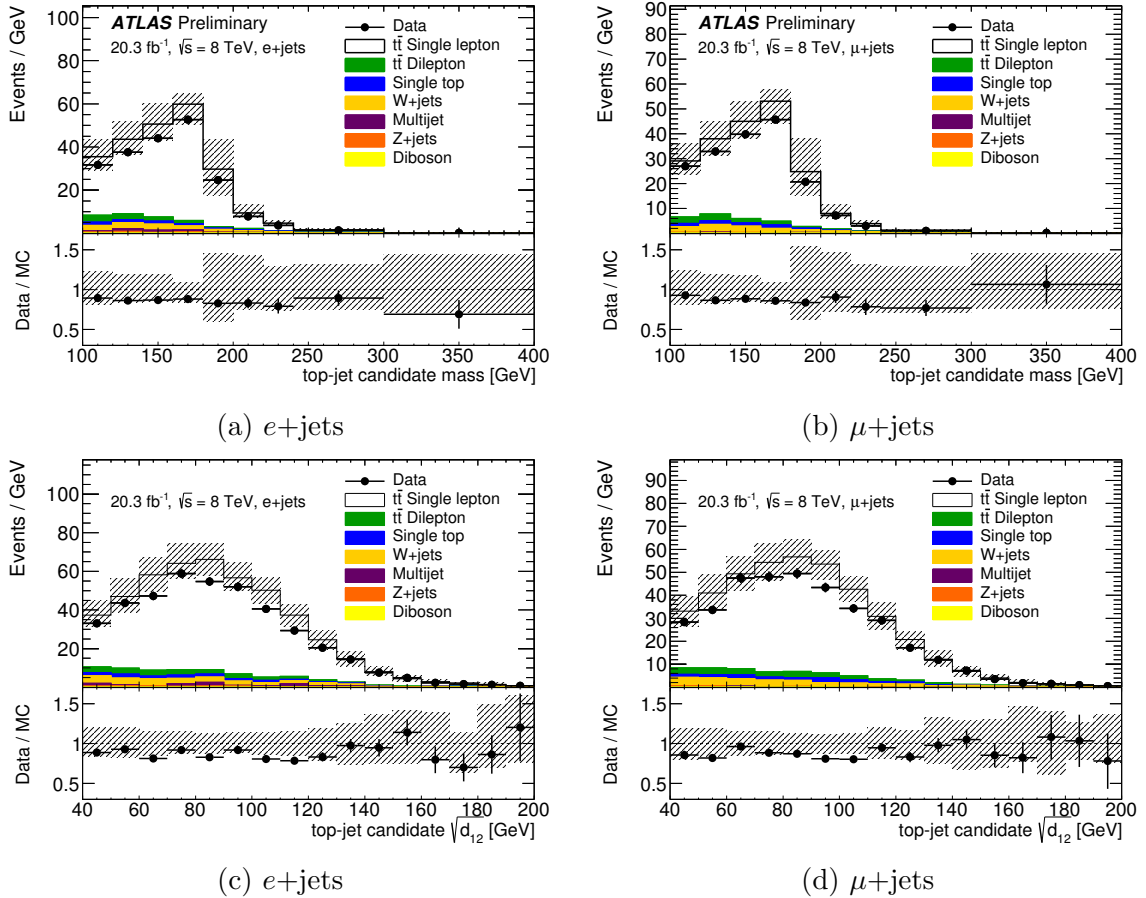
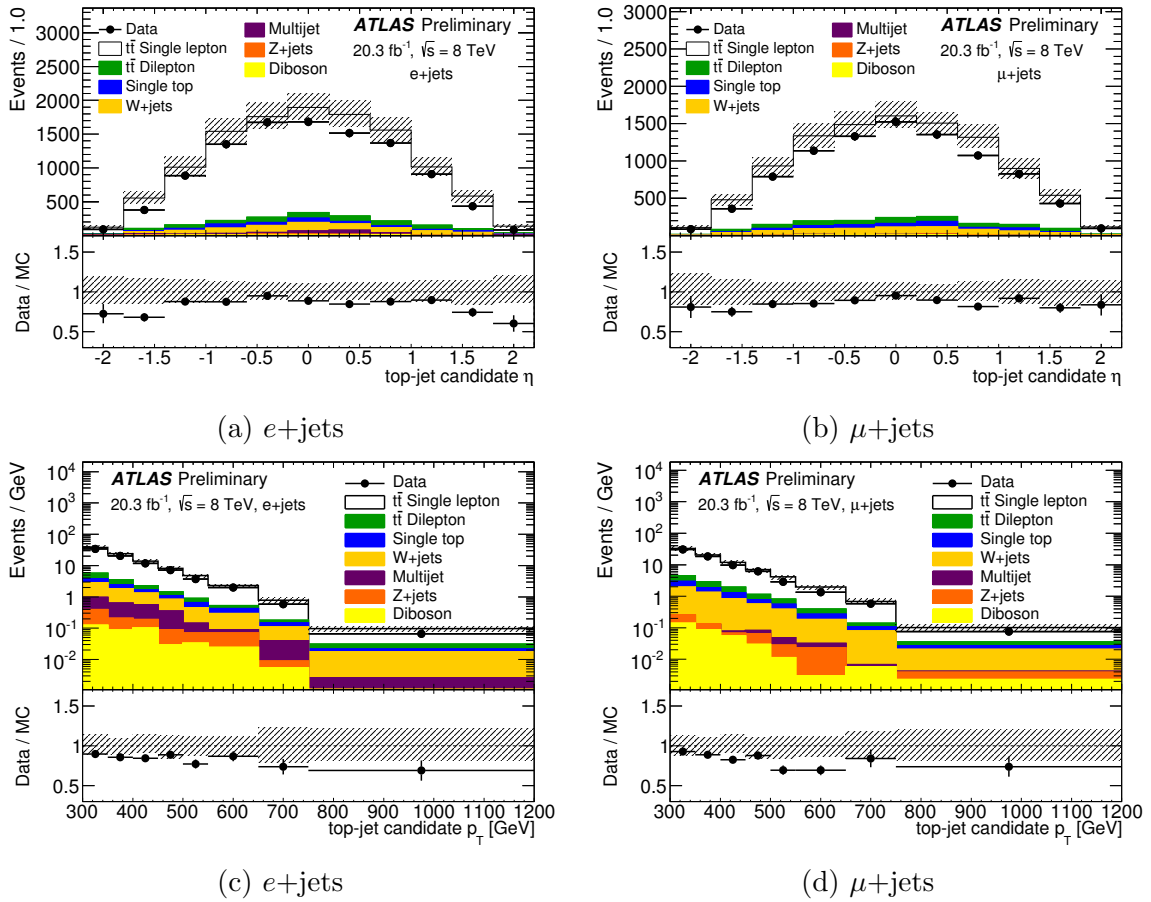
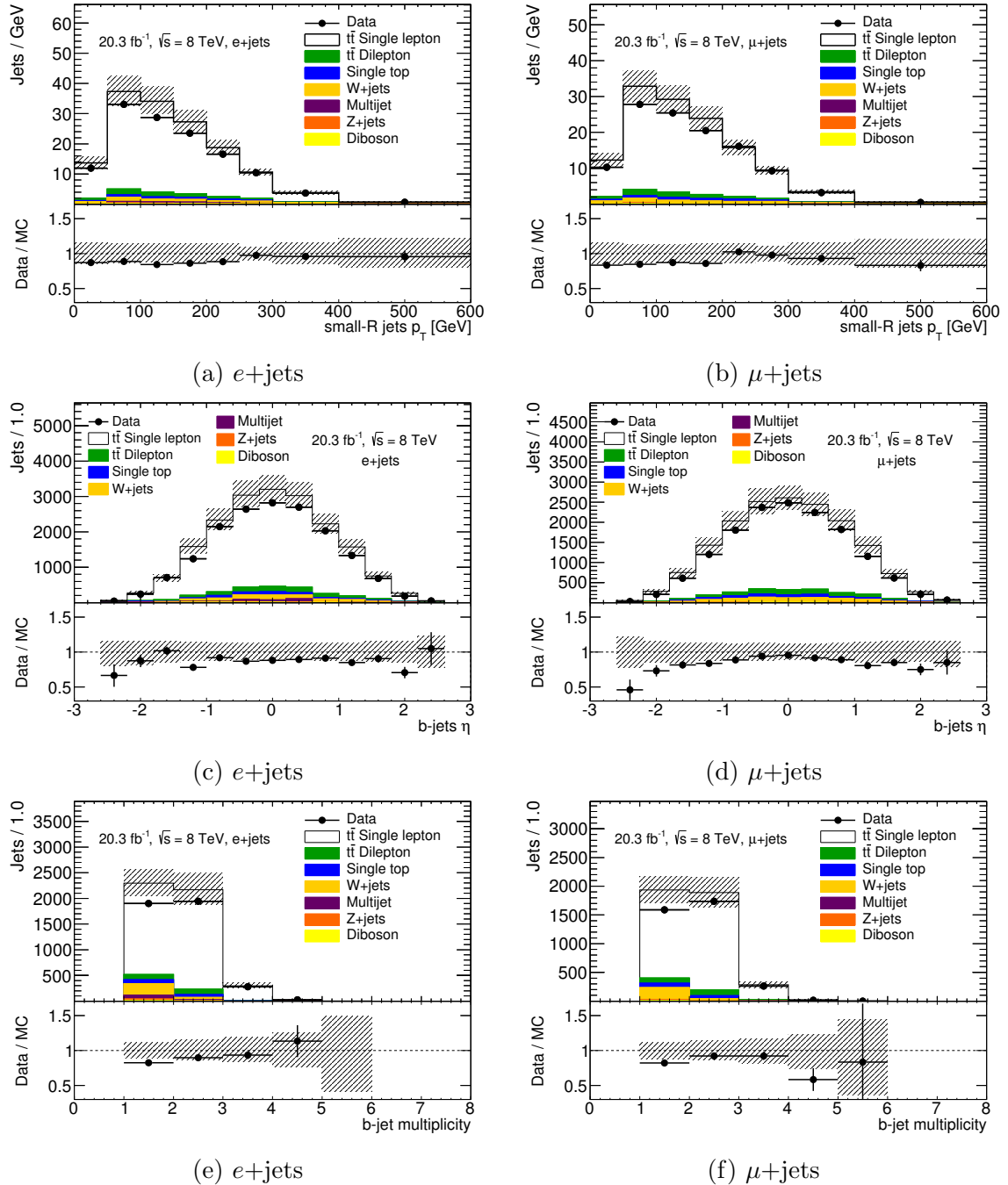


Figure 7.3: Distributions of the mass and the first splitting scale of the top-jet candidate.

Figure 7.4: Distributions of the η and the p_T of the hadronic top-jet candidate.

Figure 7.5: Distributions of η , p_T and multiplicity of the b -tagged small- R jets.

Chapter 8

Unfolding strategy

The goal of the unfolding is to correct the data to the *truth*, i.e. the measurement that would have been obtained with a perfect detector in the absence of any background events. Because in its essence the unfolding is a transfer function from one quantity to another, the method can be used to correct not only for detector effects, but also to relate the measured detector-level p_T spectrum to a top parton p_T before hadronization and parton shower. The removal of detector effects going to stable *particle level* allows to compare result to the output of various MC programs without the need to run detector simulation for each. Having removed detector effects makes it possible to also compare results between different experiments. The additional correction for hadronization and parton shower going to the *parton level* allows to compare the cross-section to analytical calculations that may not be available in the form of MC programs.

In this analysis the cross-section is reported at both the particle and the parton level. The individual corrections needed to perform each unfolding are derived from simulation and therefore introduce additional uncertainties accounting for any potential bias from choosing a particular MC sample. To illuminate the evolution of these uncertainties as the data incurs more and more corrections, the data is unfolded from the detector to the particle level and then from the particle to the parton level. To ensure the two step procedure does not introduce extra uncertainty, the parton level result is cross-checked by unfolding directly from the detector level to the parton level. In each case the same unfolding procedure is followed. For simplicity, this chapter describes the unfolding procedure in the context of the correction from detector to particle level. The same method is used in the particle-to-parton and detector-to-parton unfolding.

8.1 Unfolding procedure

The unfolding procedure consists of four successive corrections which account for the presence of background events and the limited acceptance, resolution and efficiency of the detector.

Background subtraction

First, the non- $t\bar{t}$ background as described in Chapter 7 is subtracted from the observed number of events in each reconstructed top p_T bin. Then, the contamination from dilepton $t\bar{t}$ events is removed via a multiplicative correction, i.e. the contents of each bin are multiplied by the ratio of single-lepton $t\bar{t}$ to the sum of dilepton and single-lepton $t\bar{t}$ found in simulation. Using this multiplicative factor instead of subtracting the dilepton contribution expected from simulation allows correction for the presence of dilepton background without introducing uncertainties related to its shape and normalization.

Acceptance

The acceptance correction is needed to account for events that may be considered fakes, in the sense that they are real $t\bar{t}$ events passing the reconstructed-level selection, but they do not belong to the fiducial region defined at particle-level. For example, due to poor detector resolution, an event with a particle level top-jet with $p_T = 280$ GeV may be reconstructed to a detector-level top-jet with $p_T = 301$ GeV. Such event should be removed since it should not contribute to the fiducial cross-section. The acceptance correction is obtained by taking the ratio between the number of events that pass both the reconstructed- and particle-level selections to the number of all events that pass reconstructed selection in a particular reconstructed p_T bin.

Resolution

Having accounted for events falling outside the fiducial volume, the next step is to correct the spectrum for resolution effects. This is achieved by constructing the detector *response* and inverting it so that it can be used to transform the detector-level spectrum into the corresponding particle level spectrum. The detector response is defined as the binned 2D distribution of the detector-level top-jet p_T vs. the particle-level top-jet p_T . The response is easily obtained from simulation and in theory the only remaining step is to invert it and apply it to the measured distribution. Given the discretization of the spectra and the response, this amounts to solving a system of linear equations. In practice, seeking the exact solution to the unfolding problem can be dangerous since the measured distribution suffers from finite statistics and

the response may have sizable off-diagonal components due to limited detector resolution. If handled blindly, the combination of these two effects leads to an oscillatory behavior of the unfolded result. Several methods to *regularize* the unfolded result, mitigating the impact of such fluctuations, have been developed. This analysis uses the SVD method [59], which employs the Singular Value Decomposition of the response matrix to determine its true rank. Knowing the true rank allows determination of how many coefficients in the expansion of the unfolding solution are significant and should be retained, the remaining components are suppressed, obtaining a smooth unfolded distribution. Since the spectrum being unfolded is smoothly falling, i.e. no new resonances from unknown physics source are present, this method of effectively smoothing the solution can safely recover the particle-level spectrum without biases.

Efficiency

The efficiency correction is needed to account for events that were not successfully reconstructed due to detector inefficiencies coming from object reconstruction and identification, trigger, b-tagging, etc. Its magnitude equals the inverse of the efficiency, itself defined as the ratio between the number of events that pass both the reconstructed- and particle-level selections to the number of all events that pass the particle level selection.

8.2 Bin optimization

The ideal binning is infinitely fine, giving the cross-section at every point. On the other hand, a bin size smaller than the resolution means large off-diagonal elements in the response, large statistical fluctuations and therefore a need for stronger regularization and subsequently large bin-bin correlations of the result. A bin size that is too small also prohibits a meaningful evaluation of the systematic uncertainties which would be dominated by poor statistics. To arrive at a usable binning, the analysis was first performed with a bin size such that the width of each bin is comparable to the resolution in that bin, i.e. the RMS of the distribution of the difference between the reconstructed and particle-level top p_T in the bin. Examining the reconstructed-level systematic uncertainties showed that the statistical fluctuations dominate over systematic uncertainties in many bins. Therefore, the analysis was re-done by choosing bin widths such that the width is no less than 1.5 times the resolution. The bin sizes were then rounded to the nearest 50 GeV and the last few bins were merged until the statistical uncertainty was deemed satisfactory, giving the final binning:

$$300\text{-}350, 350\text{-}400, 400\text{-}450, 450\text{-}500, 500\text{-}550, 550\text{-}650, 650\text{-}750, 750\text{-}1200 \text{ GeV.}$$

8.3 Validation

Closure test

The PowHEG+PYTHIA $t\bar{t}$ sample, which will be used to unfold the data, is used here to demonstrate that the unfolding described above can successfully recover the truth spectrum given the reconstructed spectrum. One thousand pseudo-experiments are performed. For each one, the input reconstructed spectrum is fluctuated by smearing the contents of each reconstructed p_T bin with a Gaussian with a width equal to the statistical uncertainty in the bin. The smeared spectrum is then unfolded using the response, acceptance and efficiency corrections from the nominal PowHEG+PYTHIA sample (i.e. corrections not affected by the smearing). The mean of the unfolded spectra from all pseudo experiment is then divided by the known truth spectrum. The result is shown in Figure 8.1 (a). An exact closure is observed.

Stress test

Due to the imperfect agreement of the top p_T spectrum between data and our nominal $t\bar{t}$ simulation, it is also necessary to check whether this mismodeling could introduce a bias via the unfolding. This is tested by verifying that the nominal set of unfolding corrections allows to recover a truth spectrum differing from the one found in the nominal simulation. Specifically, a spectrum that mimics the one found in the data is used. The procedure goes as follows. First, the MC is reweighed so that it better models the data. This provides a set of pseudo-data for which both the truth-level and the detector-level spectra are known. The reweighing function is a first degree polynomial derived by fitting the ratio of the simulated top-jet p_T spectrum to the data top-jet p_T after background subtraction. Then, the pseudo-data is unfolded using the nominal (unweighted) response and corrections. The unfolded result is then compared to the pseudo-data truth. Non-closure would indicate that the unfolding introduces a bias. Again a 1000 pseudo experiments, fluctuating the reweighed input spectrum and unfolding, are performed. The ratio of the mean of the experiments and the pseudo-data truth are shown in Figure 8.1 (b). The black dotted line is the ratio between the reweighed and nominal MC truth indicating the degree of distortion introduced for this test. Some fluctuations are observed, however, these remain negligible with respect to other uncertainties which will be discussed later.

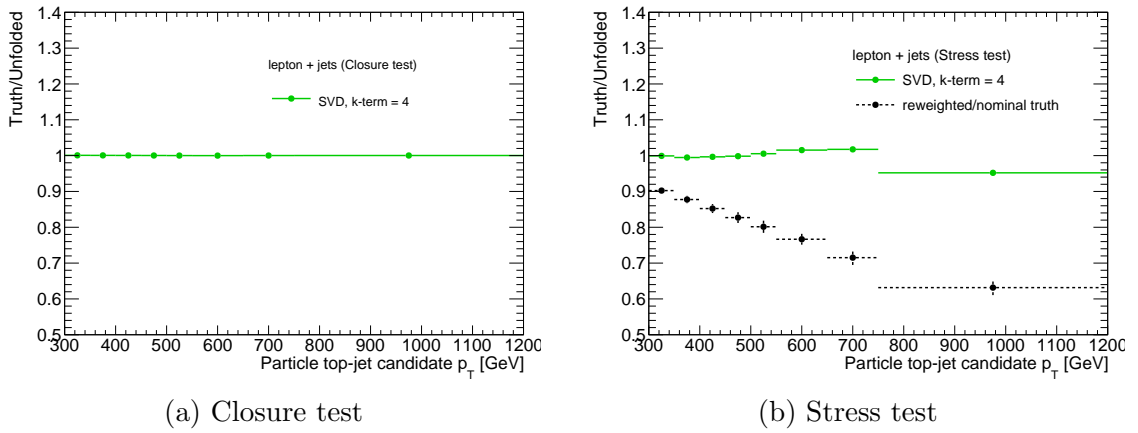


Figure 8.1: Results of (a) the closure test (unfolding the PowHEG+PYTHIA reconstructed spectrum with its own response and comparing to truth), and (b) the stress test (unfolding a reweighed PowHEG+PYTHIA reconstructed spectrum with the nominal response and comparing to the reweighed truth).

Chapter 9

Unfolding to particle level

This chapter starts with describing the particle level objects (Sec. 1) and the definition of the fiducial region for the cross-section measurement (Sec. 2). Next, the strategy used to combine the two lepton channels is presented (Sec. 3). The corrections needed to unfold the data from the detector level to the particle fiducial region are presented (Sec. 4) and then used to propagate the systematic and statistical uncertainties from the detector to the particle level (Sec. 5). Finally, the data is unfolded to obtain the final cross-section result (Sec. 6).

9.1 Particle level objects

All particle-level objects are constructed using only stable particles defined by a lifetime greater than 0.3×10^{-10} s. With this categorization, charged pions are considered stable. The objects are defined as follows:

Leptons: Both muons and electrons considered in the particle-level selection are required to not originate from a quark or a hadron. With such a definition only leptons originating from a W -boson, itself originating from a top, are considered. Electrons and muons from τ decays are accepted if the τ lepton satisfies the same criterion. The leptons are *dressed* by adding the four-vectors of all photons within $\Delta R < 0.1$ to the lepton four-vector. Such dressing allows the closer correspondence with a detector-level lepton, which encompasses a full electromagnetic shower.

Jets: The truth jet collections for both small- R and large- R jets are clustered using all stable truth particles with the exception of any leptons matching the criteria described above, and any photons used to dress them. The jets in the large- R jet collection are trimmed with the same parameters that are used at the reconstructed level and the first splitting scale, $\sqrt{d_{12}}$, is computed from the trimmed jet.

***B*-tags:** A particle-level small- R jet is considered b -tagged if it can be *ghost-matched* to a B -hadron with $p_T > 5$ GeV. Ghost-matching is realized by adding the 4-vectors of B -hadrons, scaled by a small number, e.g. 10^{-5} , to the list of stable particles used to build the jets. Since B -hadrons are not stable, they should not contribute to the jets (their decay products will). The scaling factor allows association of the B -hadrons to the jets by clustering them into the jets without affecting the jet's final 4-vector.

Missing Transverse Energy: The particle-level E_T^{miss} is given by the four-vector sum of all neutrinos not associated with a quark or hadron decay, i.e. these coming from a prompt W

9.2 Fiducial region definition

Aiming to minimize the simulation input in the measurement manifested in the unfolding corrections, the fiducial region is chosen to closely follow the event selection in data including both kinematic cuts on the objects and event topology cuts. The full definition of the particle-level fiducial cross-section includes the following requirements:

- Exactly one lepton with a dressed four-vector that has $p_T > 25$ GeV, $|\eta| < 2.5$.
- At least one small- R jet with $p_T > 25$ GeV and $|\eta| < 2.5$ within $\Delta R < 1.5$ from the lepton. If there is more than one such jet, the highest p_T one is considered the b -jet candidate.
- At least one trimmed large- R jet with $p_T > 300$ GeV, mass > 100 GeV, $\sqrt{d_{12}} > 40$ GeV and $|\eta| < 2$.
- $E_T^{miss} > 20$ GeV and $E_T^{miss} + m_T^W > 60$ GeV.
- The trimmed large- R jet is well separated from both the lepton ($\Delta\phi > 2.3$) and the small- R jet associated with the leptonic top ($\Delta R > 1.5$).
- B -tagging is only considered for small- R jets with $p_T > 25$ GeV and $|\eta| < 2.5$. There must be at least one b -tagged small- R jet s.t. $\Delta R(jet_{R=1.0}, jet_{R=0.4}) < 1$ and/or the leptonic side b -jet candidate must be b -tagged.

To facilitate channel combination, the same particle-level selection is used in both channels. The particle-level selection is compared together with the reconstructed-level selection in Table 6.1. Differences include the impact parameter cuts on lepton tracks and the JVJ requirement which are omitted, since the simulation generator record does not contain pile-up. The mini-isolation cut is not applied because its purpose is to reduce contamination from non-prompt leptons and particle-level leptons

are prompt by definition. Finally, overlap removal is not applied since prompt leptons were not included in the particle-level jet clustering, i.e. there is no overlap equivalent to the one at the detector level where electrons are reconstructed also as jets.

9.3 Electron and muon channel combination

The combination is performed by adding together events of the two channels at the reconstructed level in data. The unfolding machinery, which is described below, is constructed by adding e +jets and μ +jets events in the proportion expected from the MC. Even though the e +jets and μ +jets efficiencies are slightly different, this simple combination method can be employed if their relative yield is the same in data and MC, which is the case, as shown in Table 7.2. The acceptance and response are equivalent between the two channels within statistics.

The uncertainties on the combined spectrum are similarly evaluated based on the sum of the events. This approach properly accounts for all uncertainty correlations since uncertainties that are correlated between the two channels, such as jet energy scale (JES), will add linearly, while uncorrelated uncertainties, e.g. electron scale factors, will enter only through e +jets events and so will get properly added in quadrature to other uncertainty sources. Since the largest uncertainty, large- R JES, is common, the relative uncertainty on the combination is again similar to that observed in the individual channels. This combination method is cross-checked by performing the unfolding in each channel individually, and comparing their results with the combined result.

9.4 Unfolding ingredients

This section shows the magnitude of the acceptance and efficiency corrections as well as the detector response when unfolding from the detector to the particle level. To motivate the channel combination strategy, the unfolding ingredients for each individual channel are presented together with those obtained from the combined sample.

The left column of Figure 9.1 shows the acceptance, which is the first step in unfolding the background-subtracted data. As described earlier, it corrects for events that smear into the fiducial region at the reconstructed level due to the limited detector resolution. The correction magnitude is found to be similar for the combined ℓ +jets sample (a) and the individual channels (c) and (e). The acceptances extracted from two alternate MC programs, MC@NLO+HERWIG and ALPGEN+HERWIG, are also plotted for comparison. No significant MC dependence is observed.

Next, the unfolding requires as input the response matrix shown in Fig. 9.2. It is constructed from all events that pass both the particle and reconstructed level

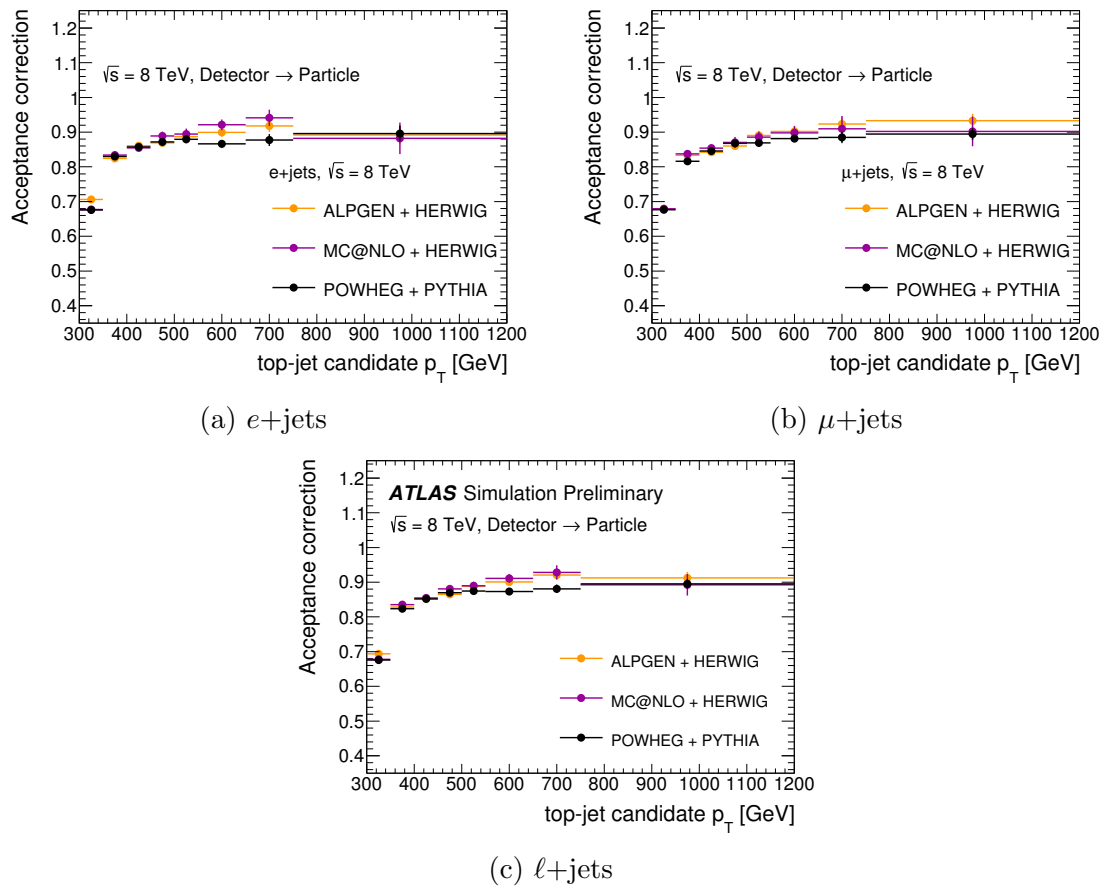


Figure 9.1: Acceptance correction, accounting for events that pass the detector level selection, but do not belong to the particle-level fiducial region. Shown separately for $e + \text{jets}$ (a) and $\mu + \text{jets}$ (b) events and combined over electrons and muons (c).

selection in the nominal $t\bar{t}$ MC sample. The migration matrix, which is the response after transposing and normalizing to the number of truth events in each truth bin, is shown in Fig. 9.3. Its diagonal gives the probability that a truth jet stays in the same p_T bin at reconstructed level, while the off-diagonal entries give the probability that the jet migrated to a different reconstructed p_T bin. The response is a better indicator of problematic unfolding behavior as it shows the available MC statistics in each bin, while the migration matrix shows more clearly the detector response independent of the statistics. As expected from the binning optimization, most entries are contained on the diagonal. The migration is also shown for each channel separately, illustrating that the detector response is essentially the same in both channels.

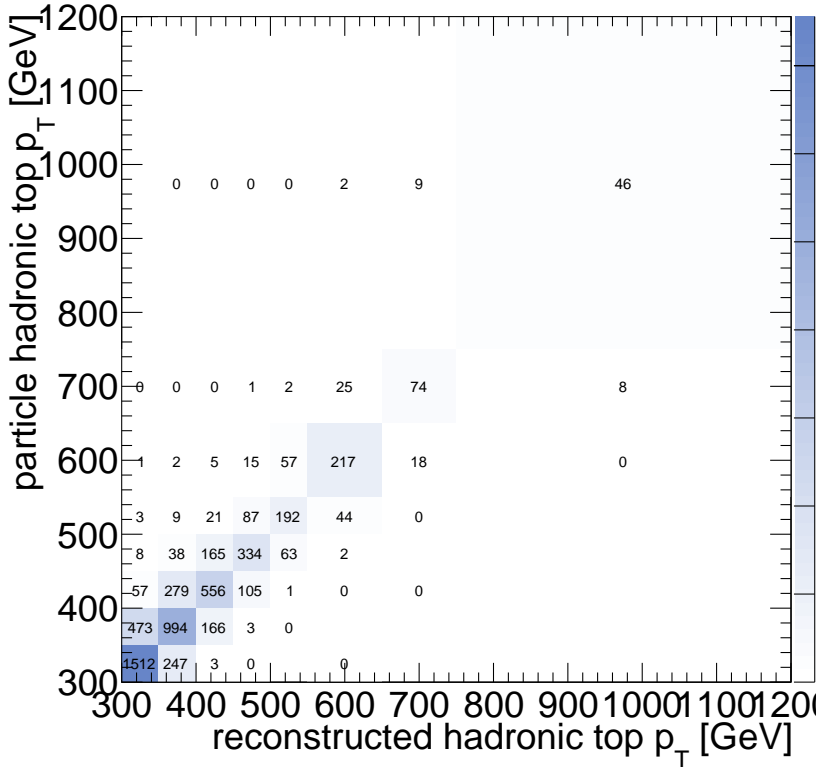


Figure 9.2: Detector response for the combined ℓ +jets sample. The z -axis shows the number of events in the bin in the nominal $t\bar{t}$ MC sample.

With the response and truth distributions in hand, one can also infer the efficiency to reconstruct events from the particle level fiducial region of interest. Its magnitude for the combined ℓ +jets sample as well as for each channel is shown in Fig. 9.4. The difference in the efficiency between the two channels is due to the varying lepton identification and trigger efficiencies between the two channels. Since in all cases the efficiency is defined with respect to the common ℓ +jets phase space, the e +jets and μ +jets efficiencies necessarily add to the ℓ +jets efficiency. The small differences

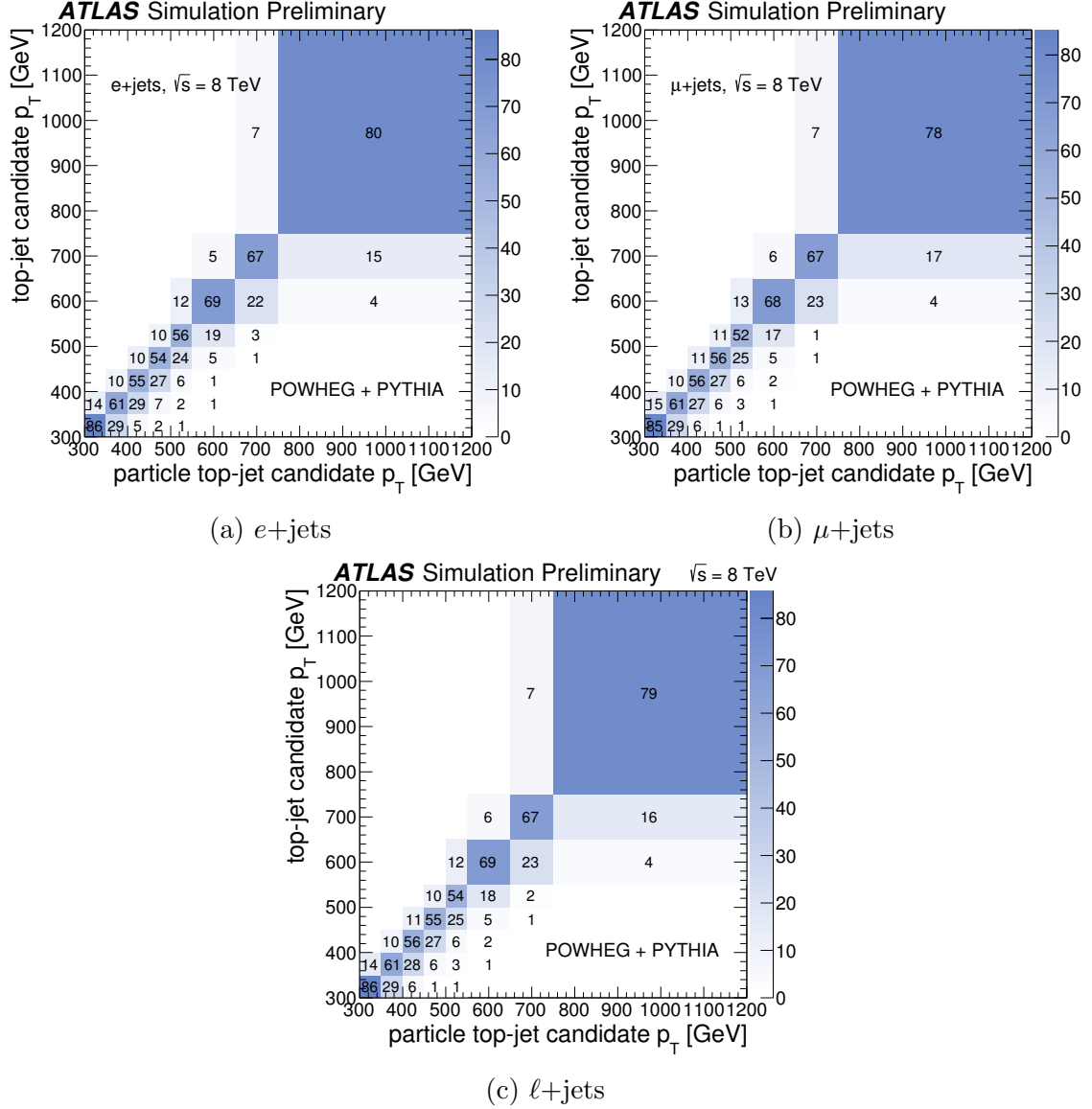


Figure 9.3: PowHeg+Pythia migration from particle to reconstructed level (normalized to number of particle level events in each column). Shown separately for $e+jets$ (a) and $\mu+jets$ (b) events and combined over electrons and muons (c).

between the efficiency model in different MC programs are taken into account via the signal model uncertainties described in the following section.

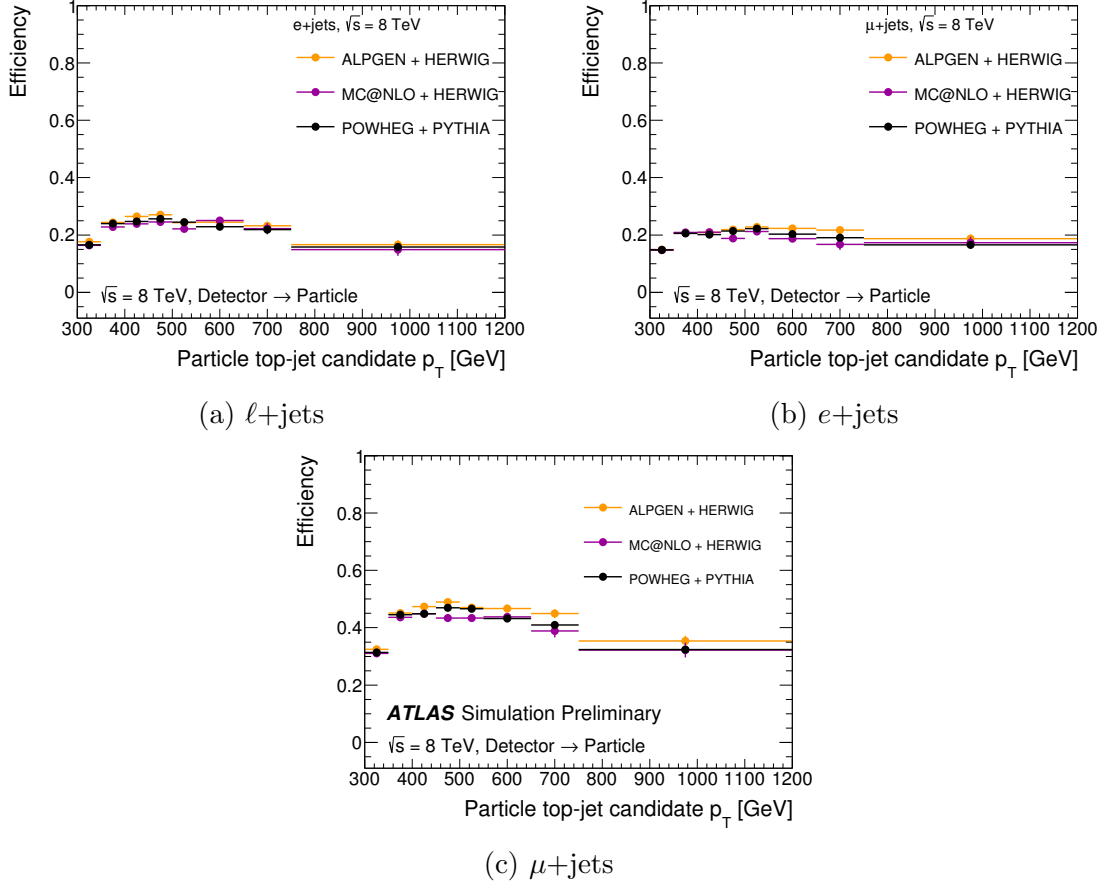


Figure 9.4: Efficiency for $t\bar{t}$ events inside the fiducial region to pass the reconstructed-level event selections as a function of the particle top p_T . Shown separately for $e+jets$ (a) and $\mu+jets$ (b) events and combined over electrons and muons (c).

9.5 Uncertainty propagation

This section outlines the strategies to propagate the systematic uncertainties from the reconstructed to the particle-level.

9.5.1 Experimental systematics

The systematics associated with object reconstruction, identification, trigger and calibration, as described in Chapter 5, as well as these associated with the background

PARTICLE LEVEL SPECTRUM - $l+\text{jets}$ ($e + \mu$)								
Uncertainty[%] / Bins [GeV]	300-350	350-400	400-450	450-500	500-550	550-650	650-750	750-1200
Large- R jet momentum scale	15/-12	11/-10	11/-10	12/-13	12/-14	14/-15	19/-17	22/-19
Large- R jet momentum resolution	1.4/-1.4	0.5/-0.5	1.6/-1.6	0.7/-0.7	0.1/-0.1	0.6/-0.6	1.5/-1.5	2.0/-2.0
Large- R jet mass and $\sqrt{d_{12}}$	4.2/-4.5	3.4/-3.5	2.6/-2.6	2.1/-2.2	2.0/-2.2	2.4/-2.6	2.9/-3.2	3.4/-3.8
Small- R jets	1.1/-1.3	0.9/-1.0	0.8/-1.4	1.1/-2.4	1.5/-2.4	2.0/-1.2	2.3/-0.9	2.6/-0.7
Heavy flavor tagging	2.2/-2.2	2.8/-2.8	3.6/-3.6	4.3/-4.3	5.2/-5.4	6.5/-7.2	8.1/-9.5	9/-11
Lepton	1.6/-1.0	1.7/-1.1	2.0/-1.1	2.3/-1.1	2.6/-1.1	3.1/-1.2	3.5/-1.2	3.9/-1.3
Missing transverse energy	0.3/-0.2	0.0/-0.1	0.0/-0.3	0.1/-0.3	0.0/-0.2	0.1/-0.2	0.1/-0.3	0.2/-0.3
MC generator/Fragmentation	1.9/-1.9	1.9/-1.9	5.1/-5.1	5.1/-5.1	6.4/-6.4	6.4/-6.4	6.1/-6.1	6.1/-6.1
Initial/Final state radiation	3.2/-3.2	3.2/-3.2	2.6/-2.6	2.6/-2.6	4.0/-4.0	4.0/-4.0	4.3/-4.3	4.3/-4.3
Backgrounds	1.3/-1.5	1.2/-1.4	1.5/-1.7	1.9/-2.1	2.6/-2.8	3.6/-3.9	4.9/-5.2	6.6/-7.0
Luminosity	3.3/-3.3	3.3/-3.3	3.3/-3.3	3.4/-3.4	3.5/-3.5	3.6/-3.6	3.7/-3.7	3.9/-3.9
MC statistics	0.9/-0.9	0.8/-0.8	1.1/-1.1	1.3/-1.3	1.6/-1.6	1.5/-1.5	2.2/-2.2	2.7/-2.7
Statistical uncertainty	2.9/-2.9	2.7/-2.7	3.3/-3.3	3.9/-3.9	4.7/-4.7	5.9/-5.9	9.1/-9.1	13/-13
Total systematic uncertainty	16/-14	13/-12	14/-13	15/-16	16/-18	18/-19	23/-23	27/-25

Table 9.1: Cross-section uncertainties by category as a function of the particle top-jet candidate p_T in $l+\text{jets}$ decay mode.

uncertainties in Chapter 7 are propagated to the particle level using simulation. For each systematic a set of pseudo data is constructed by summing up the predictions corresponding to the 1σ deviation of the systematic. For example, for JES, the event selection is carried out on all MC samples with the JES set to its nominal value $\times(1 + \sigma)$. The predictions are summed together to obtain the pseudo-data corresponding to *JES up* variation. Following, the nominal background is subtracted from the pseudo-data. The resulting distribution is then unfolded using the nominal corrections presented in Sec. 4. The relative uncertainty is then the difference between the unfolded result and nominal PowHEG+PYTHIA particle-level spectrum, normalized by the latter. This process is repeated for all experimental systematics. In the case of background systematics, the pseudo data is constructed by varying the background under study, while the rest of the predictions take on their nominal values. The uncertainties are shown in Table 10.1

9.5.2 Signal modeling

The $t\bar{t}$ simulation may not model accurately the hard scatter, parton shower and hadronization. This impacts the measurement through the efficiency, acceptance and detector response used to unfold the data. To estimate the associated uncertainty alternate MC programs with generator, parton shower and hadronization models that differ from these in the nominal MC are used to represent pseudo-data. The alternate models include ALPGEN+HERWIG, PowHEG+HERWIG and MC@NLO+HERWIG. The alternate model reconstructed spectrum is unfolded using the nominal corrections. The unfolded result is then compared to the true particle-level spectrum of the alternate generator to see if it has been recovered. The difference between the

unfolded result and the alternate generator truth spectrum, divided by the alternate generator truth is quoted as the relative uncertainty. The process is separately done for the 3 models. The resulting relative uncertainties are shown in Figure 9.5 (ACERMC appearing in the same figure is discussed next). The largest absolute deviation in each bin, increasing with p_T from 2 to 6%, is quoted as the *Generator/Parton Shower* uncertainty. For all bins, this corresponds to comparing the modeling in PowHeg+Pythia vs. MC@NLO+Herwig.

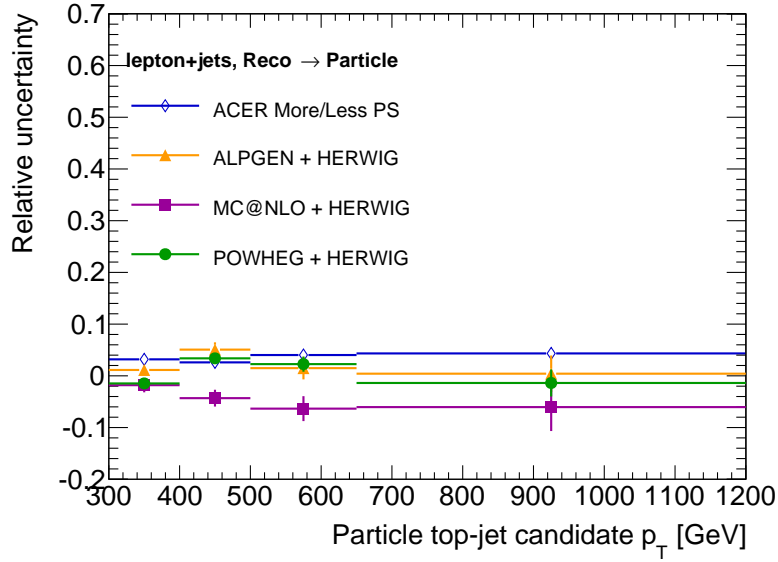


Figure 9.5: Impact of the signal model uncertainties on the particle-level spectrum.

The uncertainty due to the modeling of initial and final state radiation is estimated from two dedicated samples produced with the ACERMC MC program using generator settings that produce more or less parton shower activity relative to the nominal. The size of the variations used to construct the samples is constrained from previous measurements of the additional jet activity in $t\bar{t}$ events [60]. Here, the nominal PowHeg+Pythia is used as pseudo-data and the unfolding corrections are taken from one of the two alternate ACERMC models. The uncertainty is given by half of the difference between 1) PowHeg+Pythia unfolded with corrections from ACERMC with more parton shower and 2) PowHeg+Pythia unfolded with the corrections from ACERMC with less parton shower. The resulting relative uncertainty is $\sim 3\text{-}4\%$ as shown Figure 9.5. This is added in quadrature to the previously defined Generator/Parton Shower uncertainty.

9.5.3 Data and MC statistical uncertainties

The uncertainty accounting for the limited number of simulated $t\bar{t}$ events used to estimate the response, the efficiency and the acceptance corrections, hereafter labeled as *MC statistics*, is obtained using the bootstrap method. Each selected event is assigned a 1000 different random weights, each pulled from a Poisson with a mean of 1. The weighted events are used to fill a thousand replicas of the response, particle and reconstructed spectra. The data is then separately unfolded using corrections derived from each replica. The unfolded results are used to construct the covariance matrix. The bootstrap approach provides an estimate of the MC statistical uncertainty that properly accounts for statistical correlations between the response and correction factors. The resulting uncertainty ranges from approximately 1% at low p_T to 4% at high p_T .

The uncertainty due to the finite statistics used to model the backgrounds is determined by smearing the total background, subtracting it from the total nominal MC prediction and unfolding the resulting distribution. The uncertainty is extracted from the covariance built from a 1000 such pseudo experiments. As shown in Figure 9.6, the uncertainty due to the background reaches up to 5% at high top p_T .

Finally, the uncertainty due to finite data statistics is determined using the actual data. Again the covariance is obtained by performing a 1000 unfolding pseudo-experiments, where the data has been smeared by a Poisson with variance equal to the statistical uncertainty. The mean of the pseudo experiments results is consistent with the nominal data result, indicating no additional biases. The uncertainty obtained from the covariance is shown in Figure 9.6. It approaches 14% in the highest bin. The naive statistical uncertainty computed by taking the square root of the number of events in each particle-level top p_T bin is shown in comparison. It yields comparable results. The correlation matrix that can be obtained from the covariance, Figure 9.7, indicates the bin-to-bin correlations of the unfolded result that are expected from the application of a regularized unfolding method.

9.6 Results

To obtain the cross-section, the data is unfolded with the nominal corrections from PowHEG+PYTHIA as given in Sec. 4. The uncertainties described in Sec. 5, summed in quadrature, represent the total statistical and systematic uncertainty on the measurement. The measured differential cross-section is shown in Figure 9.8 and Table 9.2. The boosted top techniques allow to measure the top p_T spectrum up-to 1200 GeV and to cover three order of magnitude of cross-section. The total uncertainty increases with the measured p_T from approximately 15% to 29%. The predictions for the top p_T spectrum given by PowHEG+PYTHIA, PowHEG+HERWIG, MC@NLO+HERWIG and ALPGEN+HERWIG are harder than the one observed in data, with the discrepancy increasing with p_T . The cross-section is overestimated by

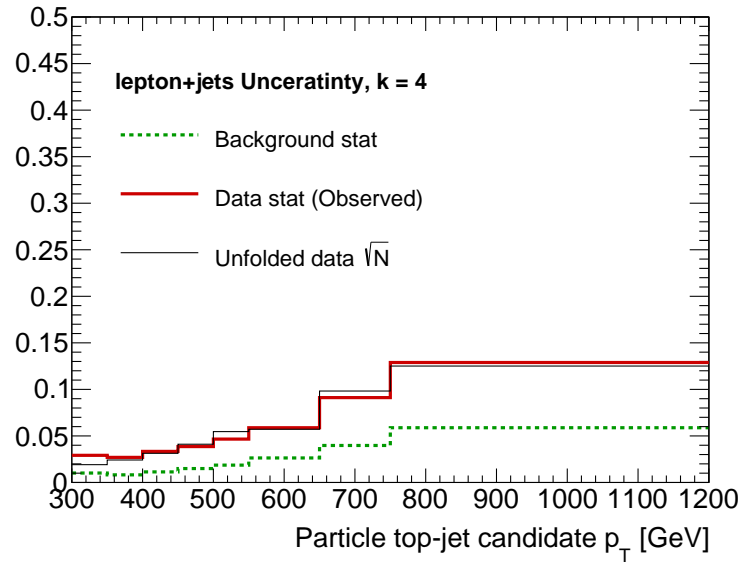


Figure 9.6: Results of the statistical uncertainty pseudo experiments.

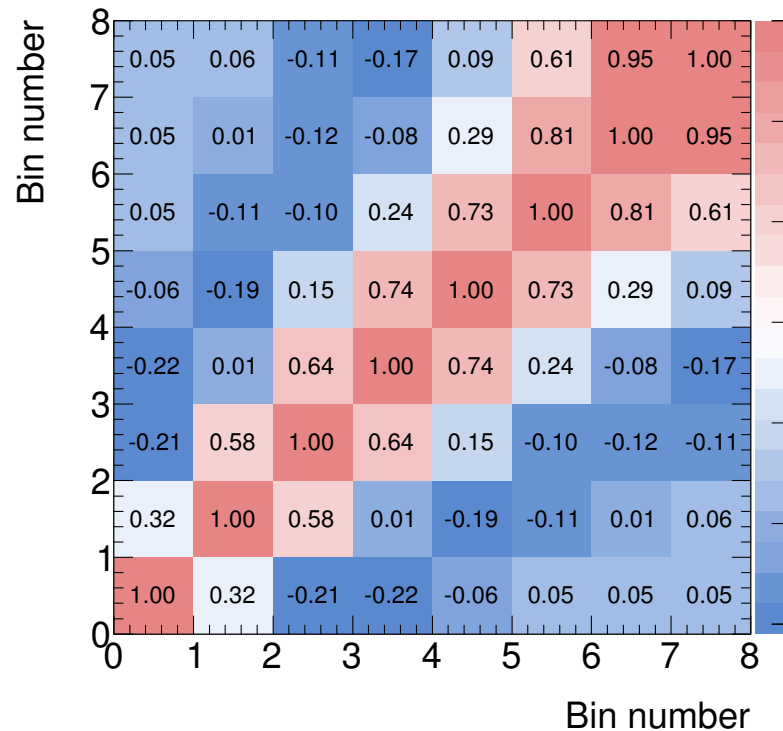


Figure 9.7: Statistical bin-to-bin correlations of the particle level result arising from the use of regularized unfolding.

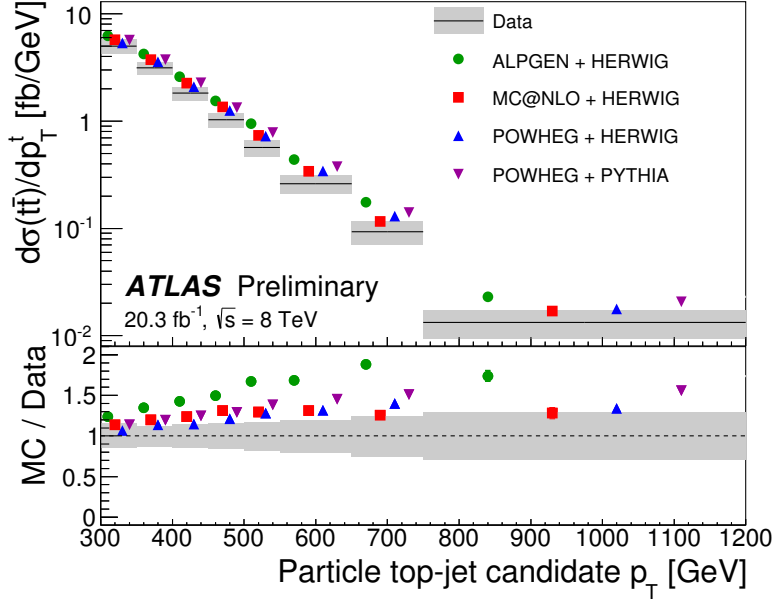


Figure 9.8: Final result for the differential cross-section as a function of the hadronic particle top-jet candidate p_T in $l+jets$ decay mode.

approximately up-to 30% for MC@NLO+HERWIG and PowHEG+HERWIG, 50% for PowHEG+PYTHIA and 70% for ALPGEN+HERWIG.

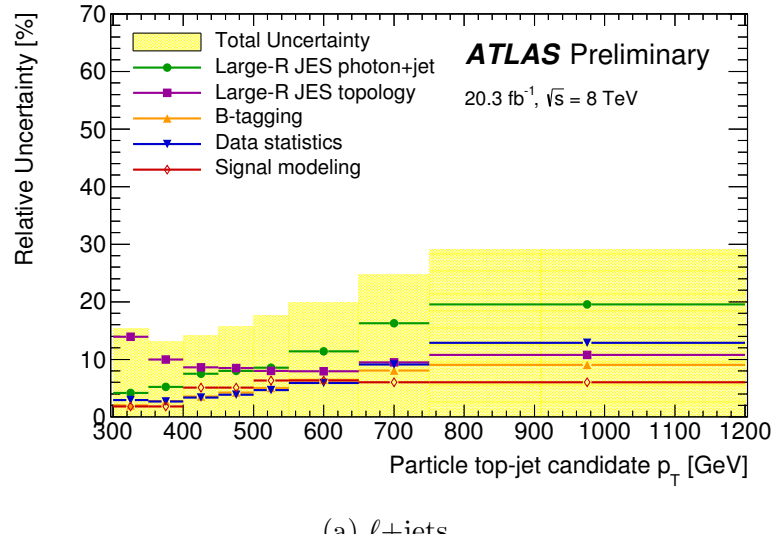
The uncertainties propagated through the unfolding are summarized in Fig. 9.9. The total statistical and systematic uncertainty after symmetrization is represented by the yellow band. The dominant uncertainty across the full spectrum is the large- R jet energy scale. The uncertainties associated with the limited data statistics, b -tagging efficiency and signal modeling are comparable and represent the largest sub-dominant systematics.

9.7 Cross-check

As a cross-check to the combination method, the data collected in each channel is separately unfolded using corrections derived from simulated events in the particular channel, as previously shown in Figures 9.1, 9.3 and 9.4. The results obtained in each channel are shown in Figure 9.10. The ratio between the cross-sections measured in each channel is shown in Figure 9.11. The error bars show only the uncorrelated uncertainties, i.e. these associated with lepton reconstruction, identification, trigger and calibration, and statistics. The results agree within the quoted uncertainties.

p_T^t [GeV]	$d\sigma(t\bar{t})/dp_T^t$ [fb/GeV]	Stat. Unc. [%]	Total Unc. [%]
300 - 350	5.0	± 2.9	± 15
350 - 400	3.1	± 2.7	± 13
400 - 450	1.8	± 3.3	± 14
450 - 500	1.0	± 3.9	± 16
500 - 550	0.57	± 4.7	± 18
550 - 650	0.26	± 5.9	± 20
650 - 750	0.093	± 9.1	± 25
750 - 1200	0.013	± 13	± 29

Table 9.2: Cross-section values as a function of the hadronically decaying top p_T in $l+jets$ decay mode.



(a) $\ell+jets$

Figure 9.9: Systematic uncertainties on the particle top-jet spectrum. The yellow band shows the total symmetrized uncertainty on the cross-section.

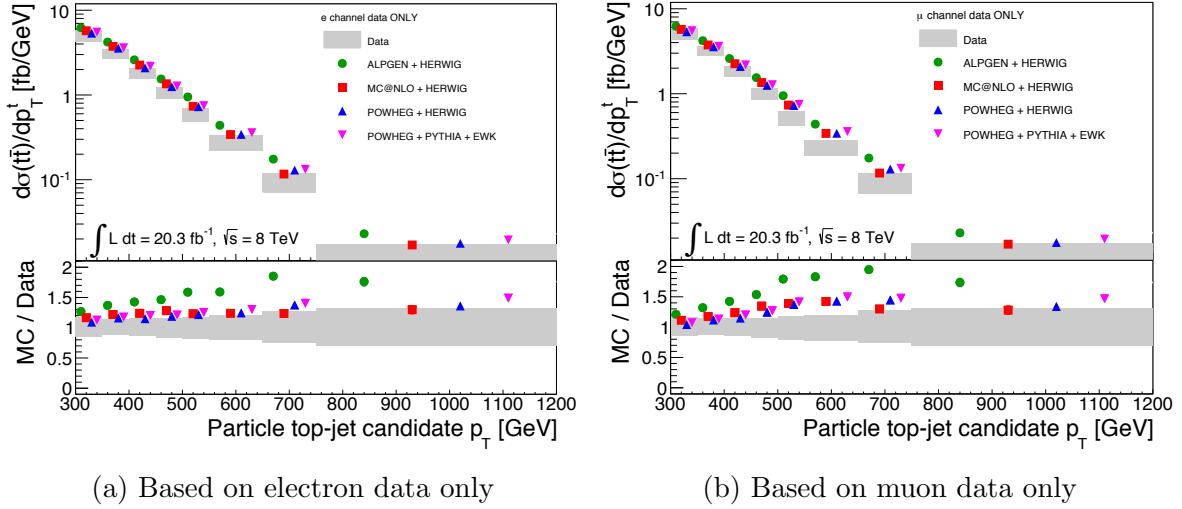


Figure 9.10: The differential cross-section in $l+jets$ $t\bar{t}$ decay mode based on individual channel data.

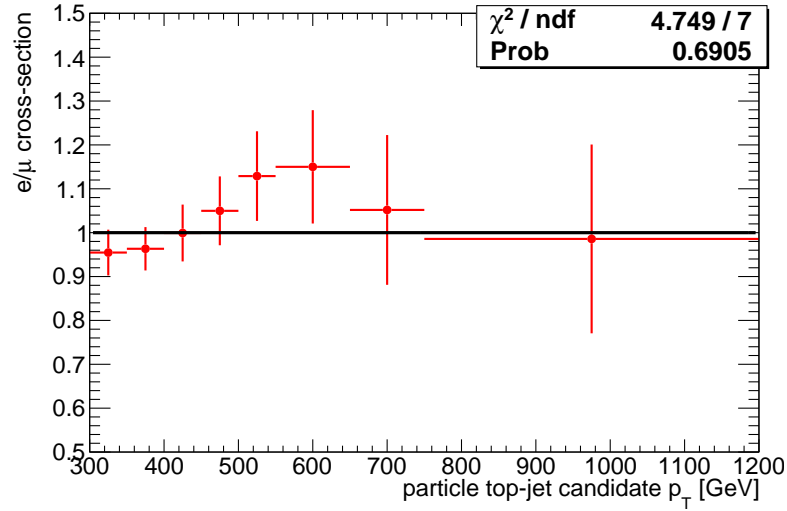


Figure 9.11: Ratio between the cross-sections measured based on individual channel data. Error bars show data statistical uncertainty, lepton scale factor and resolution as well as MC statistical uncertainties. The uncertainties related to lepton reconstruction are correlated between bins.

9.8 Discussion

The difference between the observed and predicted cross-section can be due to the combination of multiple sources including: additional partonic cross-section contributions, parton shower mismodeling, inaccurate PDFs or inadequate choice of the values of any of the MC tunable parameters.

Higher order QCD corrections to the partonic cross-section, beyond the NLO QCD prediction shown here, may soften the top p_T spectrum. Work on calculating the exact NNLO differential cross-section is ongoing and can be readily compared to the measured parton level cross-section when available. In addition, electroweak corrections to the cross-section have been shown to lower the cross-section by as much as 10% in the high- p_T tail. The comparison between the POWHEG+PYTHIA prediction before and after reweighting to account for these corrections is shown in Figure 9.12.

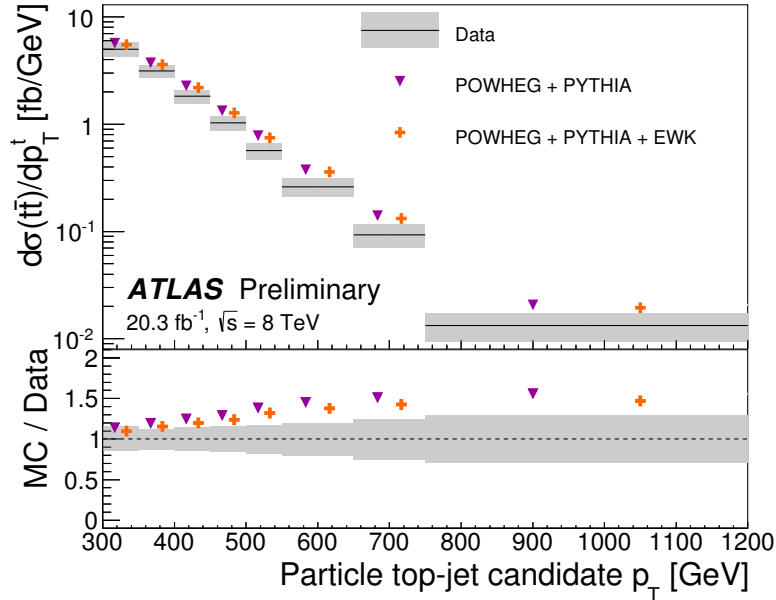


Figure 9.12: Effect of electroweak corrections and data to MC agreement.

Given that $t\bar{t}$ production at the LHC is dominated by gluon fusion, the high- p_T tail of the cross-section may be overestimated if the gluon PDF is too hard. To investigate the effects of the PDF choice, the POWHEG+PYTHIA prediction using the default CT10 PDF set is compared to the prediction using the HERAPDF [61] set, which is obtained by fitting HERA deep inelastic scattering data exclusively. As shown in Figure 9.13, even though the prediction still exceeds the data, the agreement is significantly improved. This is an indication that the gluon PDF may at least partially account for the mismodeling, but is unlikely to be the only source. This observation is

consistent with earlier studies at 7TeV, where the data was compared to predictions using HERAPDF, MSTW2008, CT10 and NNPDF 2.3¹, and the HERAPDF-based prediction was found to produce the softest p_T spectrum [28].

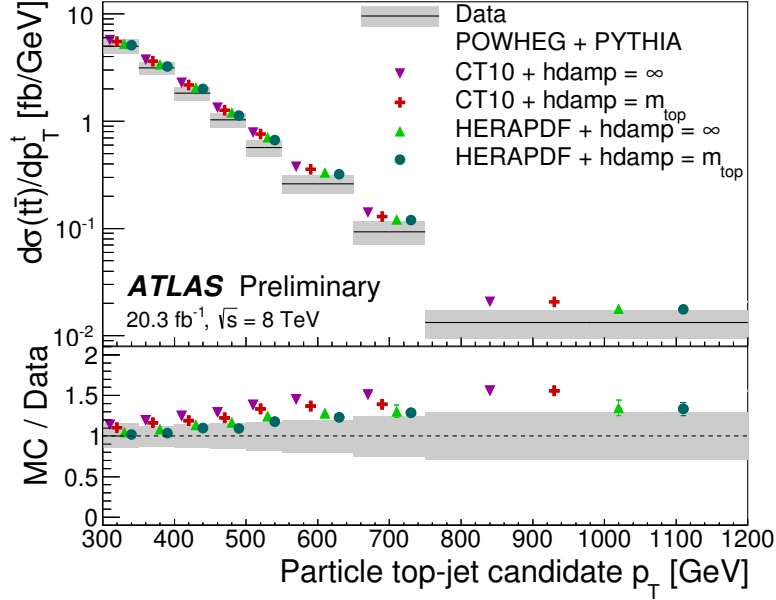


Figure 9.13: Data-to-MC agreement for the alternate HERAPDF set and different value of the PowHEG $hdamp$ parameter.

The data-to-MC agreement is also affected by the tunable MC parameters whose values are not known from first principles. An example is shown in Figure 9.13, where the prediction is shown for two values of the $hdamp$ [62] parameter in PowHEG, which effectively regulates the hardness of the first radiation emission. The prediction is shown for either $hdamp=\infty$ or $hdamp=m_{top}$. Here, a smaller value corresponds to the damping of high- p_T radiation and results in a better description of the data.

Finally, the observation that MC@NLO and PowHEG, both corresponding to NLO partonic cross-section, but interfaced to a different parton shower, give different spectra may indicate parton shower and/or merging effects.

Disentangling to what extent each of these effects may contribute to improving the modeling of the top p_T spectrum would require further MC studies.

¹The latter 3 are the results presented by the 3 global PDF fitting collaborations mentioned in Chapter 2

Chapter 10

Unfolding to parton level

In this chapter the particle-level result obtained previously is further unfolded to the parton level in order to illuminate the evolution of the uncertainties as the measurement is extrapolated to obtain the differential cross-section as a function of the top quark p_T . It is structured as follows. The top quark definition and measurement phase-space are presented in Sec. 1. The particle-to-parton unfolding corrections are given in Sec. 2. The systematic uncertainty propagation is reviewed in Sec. 3 and the final result is presented in Sec. 4.

10.1 Parton level phase-space

The parton-level top is taken as the generator particle that decays to a b and W , schematically shown in Figure 3.3¹. It represents the top quark approximately after final state radiation and before decay. This definition is dependent on the chosen MC program, since it depends on the specific parton shower, its merging with the matrix element as well as the initial and final state radiation settings. The parton level phase-space is bounded only by the requirement that the top quark p_T is above 300GeV.

10.2 Unfolding method

The method used to propagate the measurement to the parton level is exactly the same as the one employed in Chapter 9. The unfolding begins with the application of the acceptance correction that accounts for events that fall within the particle-level fiducial region, but have a parton top p_T below 300 GeV. The resulting distribution is corrected for resolution effects, based on the MC-derived particle-to-parton response.

¹Note that, even though the figure shows a leptonically decaying top, the cross-section is measured as a function of the hadronically decaying top.

Finally, the efficiency correction accounts for events that pass the parton level p_T cut, but fail the particle level selection. The acceptance, migration matrix and efficiency are shown in Figure 10.1. A comparison with Figures 9.1 and 9.4 shows that the spread between different MC predictions of the efficiency and the acceptance corrections from particle to parton level is larger than the spread of these predictions for the corresponding detector-to-particle level corrections. This may be related to the aforementioned MC program dependence of the top quark definition.

10.3 Uncertainty propagation

Each experimental uncertainty is propagated from the particle to the parton level individually. Recalling from the detector-to-particle unfolding, the reconstructed spectrum corresponding to a 1σ systematic variation is unfolded to the particle level using the nominal reco-to-particle response and corrections (at this point the particle-level uncertainty was quoted by comparing to the nominal particle level spectrum). Then, to extrapolate the uncertainty to the parton level, the shifted particle-level result is further unfolded using the nominal particle-to-parton response and corrections. The parton level uncertainty is given by comparing the unfolded result to the nominal parton-level spectrum. This is repeated for all systematics. The relative experimental uncertainties are found to be similar at the particle and the parton level. This is expected since experimental mis-measurement effects, such as JES, enter the reconstructed-to-particle response, but not the particle-to-parton response.

Again following the detector-to-particle level unfolding methodology, the signal model uncertainty is obtained by unfolding alternate MC reconstructed distributions to the particle level and then further to the parton level using the appropriate nominal PowHEG+PYTHIA response and corrections for each unfolding step. The unfolding result is compared to the nominal parton level distribution of the alternate MC, which can be one of PowHEG+HERWIG, MC@NLO+HERWIG and ALPGEN+HERWIG. The result is shown in Figure 10.2 (a). The largest relative deviation is quoted as *Generator and PS* uncertainty. As anticipated from the comparison of the unfolding corrections given by different MC models in Figure 10.1, the signal model uncertainty is significantly increased with respect to the particle level.

To estimate the *IFSR* uncertainty, corrections derived from the ACERMC with more parton shower and ACERMC with less parton shower samples are used to unfold the nominal PowHEG+PYTHIA to particle and then parton level. The uncertainty is taken as half of the difference between the two parton-level results normalized by the average. The impact of the IFSR uncertainties is shown in blue diamonds in Figure 10.2 (a).

The statistical uncertainties are obtained by running the same set of pseudo-experiments described for the particle level (i.e. smearing the reconstructed spectrum to study data or background statistics and bootstrap in the case of studying the MC

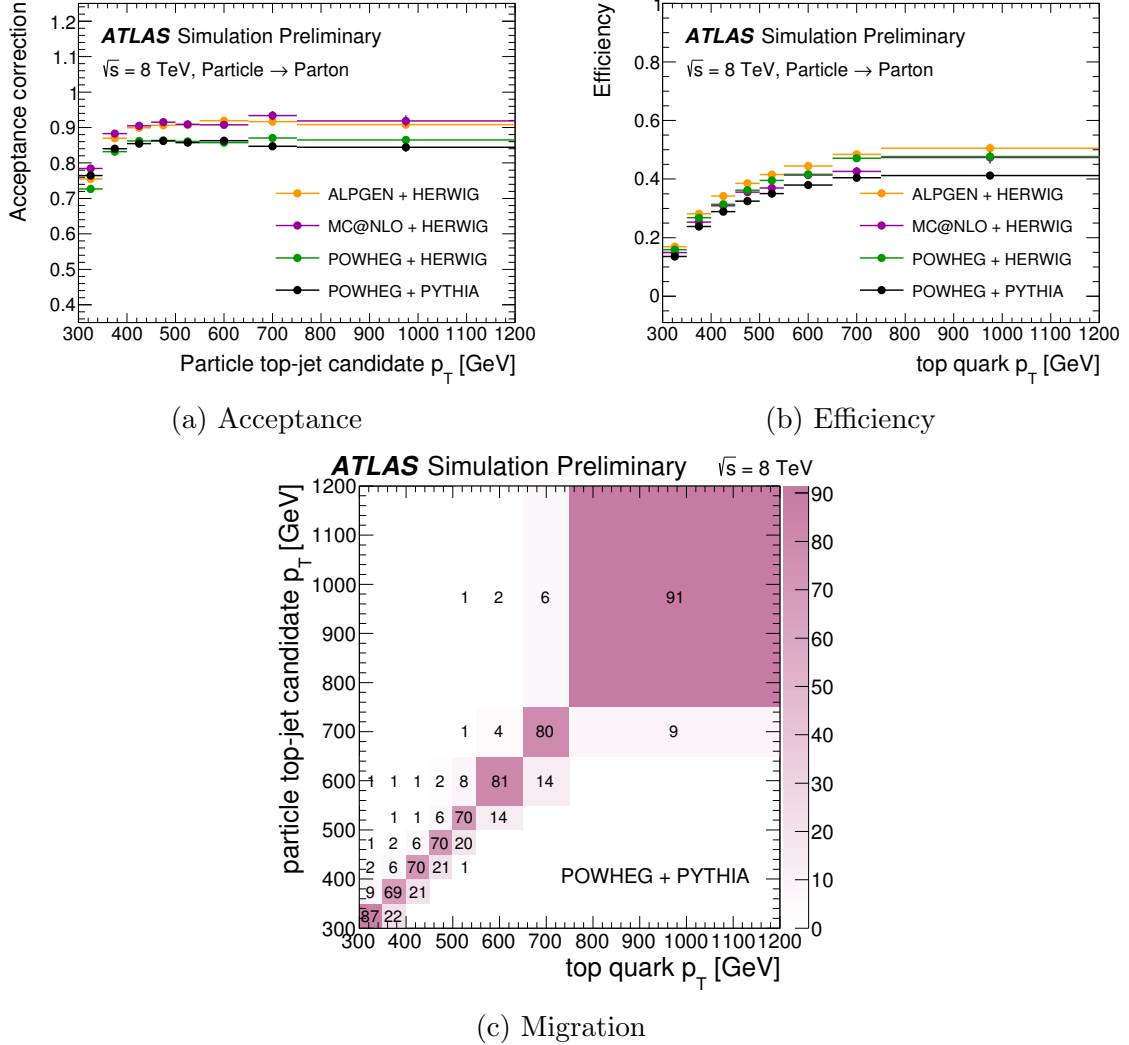


Figure 10.1: (a) Acceptance correction factors, i.e. number of $t\bar{t}$ events passing both particle and parton-level cuts divided the number of events passing only the particle-level cuts as a function of top p_T . (b) Efficiency for $t\bar{t}$ events inside the fiducial region to pass the particle-level event selections as a function of the parton top p_T . (c) PowHEG+PYTHIA migration from parton to particle level (normalized to number of parton level events in each column)

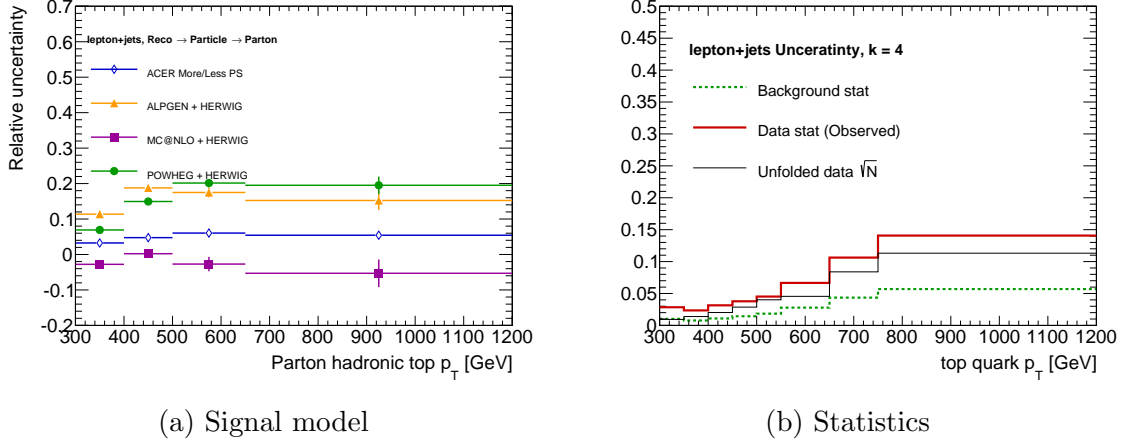


Figure 10.2: (a) Impact of the signal generator uncertainties on the parton spectrum. (b) Statistical uncertainties determined from pseudo experiments.

model statistics). However, instead of stopping the unfolding at the particle level, each pseudo-experiment undergoes a second particle-to-parton unfolding step. The results are used to build the covariance matrices for each uncertainty source. The relative statistical uncertainties are found to be comparable to the these observed at the particle level as shown in Figure 10.2 (b). The parton-level bin-to-bin correlations resulting from the combination of limited data statistics with regularized unfolding undergo a moderate increase with respect to the particle level. This can be seen in Figure 10.3, showing the parton-level correlation matrix.

The size of all uncertainties categorized by source is given in Table 10.1

10.4 Results

The unfolded data is scaled by the inverse of the branching fraction to $\ell+\text{jets}$, 0.438 ± 0.006 [8], to obtain the total $t\bar{t}$ cross-section, which is compared to the parton-level predictions from PowHEG+PYTHIA, PowHEG+HERWIG, MC@NLO+HERWIG and ALPGEN+HERWIG in Figure 10.4. The cross-section values in each bin with the corresponding uncertainties are given in Table 10.2. The total uncertainty increases with the measured p_T from approximately 23% to 37%. Relative to the particle level results, the agreement between the data and the predictions is improved due to both central value shifts and increased uncertainties. In particular, PowHEG+HERWIG and MC@NLO+HERWIG are both consistent with the data across the full p_T range within the quoted uncertainty. Similarly to the particle level, PowHEG+PYTHIA and ALPGEN+HERWIG lie furthest from the data.

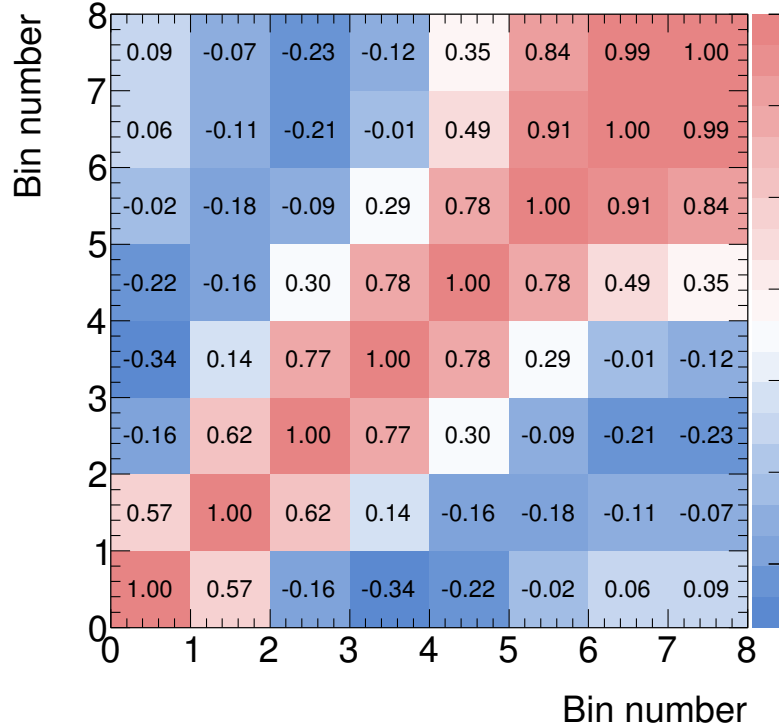


Figure 10.3: Statistical bin-to-bin correlations of the parton level result arising from the combination of limited data statistics and the use of regularized unfolding.

PARTON LEVEL SPECTRUM - $l+jets$ ($e + \mu$)								
Uncertainty[%] / Bins [GeV]	300-350	350-400	400-450	450-500	500-550	550-650	650-750	750-1200
Large- R jet momentum scale	14/-11	12/-10	11/-10	11/-12	12/-15	15/-17	19/-18	21/-20
Large- R jet momentum resolution	1.2/-1.2	0.8/-0.8	1.1/-1.1	0.8/-0.8	0.4/-0.4	0.6/-0.6	1.1/-1.1	1.5/-1.5
Large- R jet mass and $\sqrt{d_{12}}$	4.3/-4.6	3.5/-3.6	2.6/-2.6	2.0/-2.1	1.9/-2.1	2.3/-2.5	2.7/-3.1	3.1/-3.4
Small- R jets	1.1/-1.2	0.9/-1.1	0.8/-1.5	1.0/-2.2	1.5/-2.1	2.0/-1.4	2.6/-1.1	2.9/-1.0
Heavy flavor tagging	2.1/-2.1	2.7/-2.7	3.6/-3.5	4.5/-4.5	5.6/-6.0	7.1/-8.0	9/-10	9/-11
Lepton	1.6/-1.0	1.7/-1.0	2.0/-1.1	2.3/-1.1	2.8/-1.1	3.3/-1.2	3.7/-1.3	4.0/-1.3
Missing transverse energy	0.3/-0.2	0.0/-0.1	0.0/-0.3	0.1/-0.4	0.0/-0.3	0.0/-0.2	0.2/-0.3	0.2/-0.3
MC generator/Fragmentation	17/-17	17/-17	24/-24	24/-24	23/-23	23/-23	23/-23	23/-23
Initial/Final state radiation	3.0/-3.0	3.0/-3.0	4.3/-4.3	4.3/-4.3	5.8/-5.8	5.8/-5.8	5.4/-5.4	5.4/-5.4
Backgrounds	1.3/-1.5	1.1/-1.3	1.5/-1.7	1.9/-2.1	2.6/-2.9	3.8/-4.1	5.4/-5.7	6.6/-7.0
Luminosity	3.3/-3.3	3.3/-3.3	3.3/-3.3	3.4/-3.4	3.5/-3.5	3.6/-3.6	3.8/-3.8	3.9/-3.9
MC statistics	1.0/-1.0	0.7/-0.7	1.1/-1.1	1.3/-1.3	1.5/-1.5	1.7/-1.7	2.4/-2.4	3.0/-3.0
Statistical uncertainty	2.8/-2.8	2.4/-2.4	3.1/-3.1	3.8/-3.8	4.5/-4.5	6.7/-6.7	11/-11	14/-14
Total systematic uncertainty	23/-22	22/-21	27/-27	28/-28	28/-29	30/-31	33/-33	35/-34

Table 10.1: Cross-section uncertainties by category as a function of the top quark p_T .

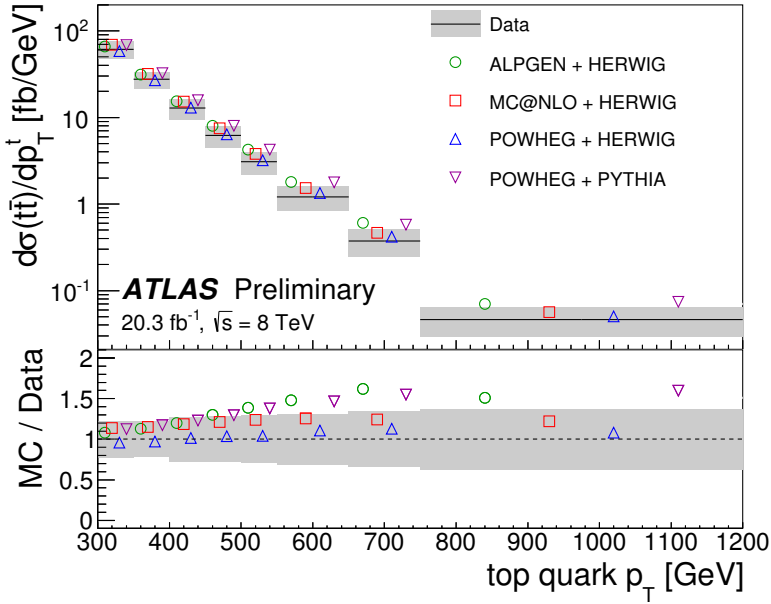


Figure 10.4: Final result for the differential cross-section as a function of the hadronically decaying top quark p_T

p_T^t [GeV]	$d\sigma(t\bar{t})/dp_T^t$ [fb/GeV]	Stat. Unc. [%]	Total Unc. [%]
300 - 350	61	± 2.8	± 23
350 - 400	28	± 2.4	± 22
400 - 450	13	± 3.1	± 27
450 - 500	6.2	± 3.8	± 28
500 - 550	3.1	± 4.5	± 29
550 - 650	1.2	± 6.7	± 31
650 - 750	0.37	± 11	± 35
750 - 1200	0.046	± 14	± 37

Table 10.2: Cross-section values as a function of the hadronically decaying top quark p_T in $l+jets$ decay mode.

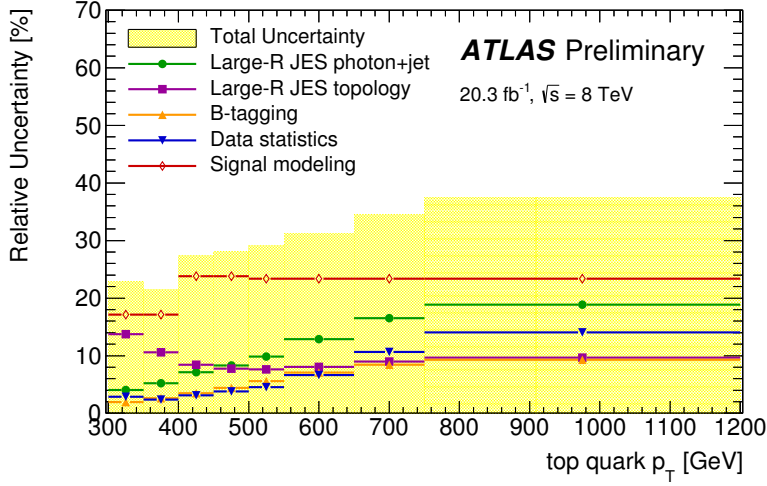


Figure 10.5: Systematic uncertainties on the unfolded spectrum at parton level.

A summary of all the uncertainties at parton level is shown in Figure 10.5. The only significant difference with respect to the particle-level result is the signal model uncertainty, which is the dominant source of uncertainty at the parton-level across the full p_T range. As mentioned earlier, this result is expected for two reasons, the larger reliance on the MC model when extrapolating beyond stable particles and the potential generator dependence of the top quark definition.

As a cross-check to the result obtained in this two step unfolding process, i.e. detector-to-particle followed by particle-to-parton correction, the unfolding is also performed directly from the reconstructed to the parton level. The results from the two approaches agree both in central value and in the associated uncertainty.

Chapter 11

Conclusion

The top quark pair differential cross-section has been measured as a function of the top quark p_T using 20.3 fb^{-1} of $\sqrt{s} = 8 \text{ TeV}$ data. The top quark is reconstructed with large- R jets and identified with jet substructure techniques. The cross-section is measured at the stable particle level in a fiducial region close to the detector level selection to minimize any theoretical input due to extrapolations beyond the detector acceptance. The measurement is reported in the top-jet candidate p_T range of 300 GeV to 1.2 TeV (see Figure 9.8 and Table 9.2). The total uncertainty increases with the measured p_T from approximately 15% to 29%. The prediction overestimates the data by approximately up-to 30% for MC@NLO+HERWIG and PowHEG+HERWIG, 50% for PowHEG+PYTHIA and 70% for ALPGEN+HERWIG. The cross-section is also reported at parton level, extrapolated to the full phase space (see Figure 10.4 and Table 10.2). The predictions still generally overestimate the data for all models except MC@NLO+HERWIG. However, since the uncertainty increases, ranging with p_T from approximately 23% to 37%, due to larger contributions from uncertainty source related to $t\bar{t}$ modeling, the significance of any observations is notably reduced. The difference between the observed and predicted cross-section can be the result of may combined effects, including additional partonic cross-section contributions, the details of the parton shower, PDF mismodeling, or inadequate choice of the values of any of the MC tunable parameters. Further studies would be needed to make definitive conclusions on the relative sizes of such effects.

The results confirm findings from previous measurements [2, 3, 4] indicating that MC predictions of the top p_T spectrum start to exceed the data as the top p_T increases. The present measurement complements these results by extending the top p_T measurement into the TeV scale and confirming the previous observations using entirely different top reconstruction techniques. In addition, the use of a robust top candidate definition based on an infrared and collinear safe observable built from stable particles will allow the result to remain a useful constraint as the phenomenological models used to describe hadron collisions evolve.

Bibliography

- [1] Y. Gershtein, M. Luty, M. Narain, L. T. Wang, D. Whiteson, et al. Working Group Report: New Particles, Forces, and Dimensions. 2013.
- [2] Georges Aad et al. Measurements of normalized differential cross-sections for ttbar production in pp collisions at $\text{sqrt}(s) = 7 \text{ TeV}$ using the ATLAS detector. 2014.
- [3] Measurement of the differential ttbar cross section in the lepton+jets channel at 8 TeV. Technical Report CMS-PAS-TOP-12-027, 2012.
- [4] Measurement of the differential ttbar cross section in the dilepton channel at 8 TeV. Technical Report CMS-PAS-TOP-12-028, 2012.
- [5] Stefan Höche. Developments in Sherpa and BlackHat. <http://indico.cern.ch/event/296900/session/9/contribution/13/material/slides/0.pdf>, 2014.
- [6] John M. Campbell, J.W. Huston, and W.J. Stirling. Hard Interactions of Quarks and Gluons: A Primer for LHC Physics. *Rept. Prog. Phys.*, 70:89, 2007.
- [7] Gavin P. Salam. Elements of QCD for hadron colliders. 2010.
- [8] K.A. Olive et al. Reviews of particle physics. Technical report, Particle Data Group, 2014.
- [9] John M. Campbell, J.W. Huston, and W.J. Stirling. Hard Interactions of Quarks and Gluons: A Primer for LHC Physics. *Rept. Prog. Phys.*, 70:89, 2007.
- [10] Hung-Liang Lai et al. New parton distributions for collider physics. 2010.
- [11] Alan D. Martin, W. James Stirling, Robert S. Thorne, and Graeme Watt. Parton distributions for the LHC. 2009.
- [12] Richard D. Ball et al. Parton distributions with LHC data. 2012.
- [13] T. Gleisberg, Stefan Hoeche, F. Krauss, M. Schonherr, S. Schumann, et al. Event generation with SHERPA 1.1. *JHEP*, 0902:007, 2009.

- [14] Torbjorn Sjostrand, Stephen Mrenna, and Peter Z. Skands. PYTHIA 6.4 Physics and Manual. *JHEP*, 0605:026, 2006.
- [15] G. Corcella, I.G. Knowles, G. Marchesini, S. Moretti, K. Odagiri, et al. HERWIG 6: An Event generator for hadron emission reactions with interfering gluons (including supersymmetric processes). *JHEP*, 0101:010, 2001.
- [16] Johan Alwall, Stefan Hoeche, F. Krauss, N. Lavesson, L. Lonnblad, et al. Comparative study of various algorithms for the merging of parton showers and matrix elements in hadronic collisions. *Eur.Phys.J.*, C53:473–500, 2008.
- [17] Michelangelo L. Mangano, Mauro Moretti, Fulvio Piccinini, Roberto Pittau, and Antonio D. Polosa. ALPGEN, a generator for hard multiparton processes in hadronic collisions. *JHEP*, 0307:001, 2003.
- [18] Stefano Frixione and Bryan R. Webber. Matching NLO QCD computations and parton shower simulations. *JHEP*, 0206:029, 2002.
- [19] Stefano Frixione, Paolo Nason, and Carlo Oleari. Matching NLO QCD computations with Parton Shower simulations: the POWHEG method. *JHEP*, 0711:070, 2007.
- [20] Paolo Torrielli and Stefano Frixione. Matching NLO QCD computations with PYTHIA using MC@NLO. *JHEP*, 1004:110, 2010.
- [21] Matteo Cacciari, Gavin P. Salam, and Gregory Soyez. The Anti-k(t) jet clustering algorithm. *JHEP*, 0804:063, 2008.
- [22] Stephen D. Ellis and Davison E. Soper. Successive combination jet algorithm for hadron collisions. *Phys.Rev.*, D48:3160–3166, 1993.
- [23] Georges Aad et al. Performance of jet substructure techniques for large-R jets in proton-proton collisions at $\sqrt{s} = 7$ TeV using the ATLAS detector. 2013.
- [24] J. Wess and B. Zumino. Supergauge transformations in four dimensions. *Nucl.Phys.*, B:70, 1974.
- [25] Projected Performance of an Upgraded CMS Detector at the LHC and HL-LHC: Contribution to the Snowmass Process. 2013.
- [26] Frank-Peter Schilling. Top Quark Physics at the LHC: A Review of the First Two Years. *Int.J.Mod.Phys.*, A27:1230016, 2012.
- [27] Michal Czakon, Michelangelo L. Mangano, Alexander Mitov, and Juan Rojo. Constraints on the gluon PDF from top quark pair production at hadron colliders. *JHEP*, 1307:167, 2013.

- [28] Georges Aad et al. Measurements of normalized differential cross-sections for ttbar production in pp collisions at $\text{sqrt}(s) = 7 \text{ TeV}$ using the ATLAS detector. *Phys.Rev.*, D90:072004, 2014.
- [29] Georges Aad et al. Improved luminosity determination in pp collisions at $\sqrt{s} = 7 \text{ TeV}$ using the ATLAS detector at the LHC. *Eur.Phys.J.*, C73:2518, 2013.
- [30] G. Aad et al. Expected Performance of the ATLAS Experiment - Detector, Trigger and Physics. 2009.
- [31] T. Cornelissen, M. Elsing, I. Gavrilenco, W. Liebig, E. Moyse, et al. The new ATLAS track reconstruction (NEWT). *J.Phys.Conf.Ser.*, 119:032014, 2008.
- [32] Georges Aad et al. Muon reconstruction efficiency and momentum resolution of the ATLAS experiment in proton-proton collisions at $\sqrt{s}=7 \text{ TeV}$ in 2010. *Eur.Phys.J.*, C74:3034, 2014.
- [33] Georges Aad et al. Measurement of the muon reconstruction performance of the ATLAS detector using 2011 and 2012 LHC proton-proton collision data. 2014.
- [34] Georges Aad et al. Performance of the ATLAS muon trigger in pp collisions at $\sqrt{s} = 8 \text{ TeV}$. 2014.
- [35] Georges Aad et al. Electron reconstruction and identification efficiency measurements with the ATLAS detector using the 2011 LHC proton-proton collision data. *Eur.Phys.J.*, C74:2941, 2014.
- [36] Georges Aad et al. Electron and photon energy calibration with the ATLAS detector using LHC Run 1 data. *Eur.Phys.J.*, C74(10):3071, 2014.
- [37] Performance of the ATLAS Electron and Photon Trigger in p-p Collisions at $\text{sqrt}s = 7 \text{ TeV}$ in 2011. Technical Report ATLAS-CONF-2012-048, CERN, Geneva, May 2012.
- [38] M Wieters, R Mantifel, A Tricoli, and P Bell. Single Electron Trigger Performance Plots. Technical Report ATL-COM-DAQ-2012-146, CERN, Geneva, Jun 2012.
- [39] Georges Aad et al. Jet energy measurement and its systematic uncertainty in proton-proton collisions at $\sqrt{s} = 7 \text{ TeV}$ with the ATLAS detector. 2014.
- [40] Georges Aad et al. Jet mass and substructure of inclusive jets in $\sqrt{s} = 7 \text{ TeV}$ pp collisions with the ATLAS experiment. *JHEP*, 1205:128, 2012.
- [41] Commissioning of the ATLAS high-performance b-tagging algorithms in the 7 TeV collision data. Technical Report ATLAS-CONF-2011-102, CERN, Geneva, Jul 2011.

- [42] Measuring the b-tag efficiency in a top-pair sample with 4.7 fb^{-1} of data from the ATLAS detector. Technical Report ATLAS-CONF-2012-097, CERN, Geneva, Jul 2012.
- [43] Calibration of the performance of b -tagging for c and light-flavour jets in the 2012 ATLAS data. Technical Report ATLAS-CONF-2014-046, CERN, Geneva, Jul 2014.
- [44] Calibrating the b-Tag Efficiency and Mistag Rate in 35 pb^{-1} of Data with the ATLAS Detector. Technical Report ATLAS-CONF-2011-089, CERN, Geneva, Jun 2011.
- [45] Performance of Missing Transverse Momentum Reconstruction in ATLAS studied in Proton-Proton Collisions recorded in 2012 at 8 TeV. Technical Report ATLAS-CONF-2013-082, CERN, Geneva, Aug 2013.
- [46] ATLAS Collaboration. A search for $t\bar{t}$ resonances in the lepton plus jets final state with ATLAS using 14 fb^{-1} of pp collisions at $\sqrt{s} = 8 \text{ TeV}$. Technical Report ATLAS-COM-CONF-2013-052, CERN, Geneva, Apr 2013. original internal draft at: <https://cds.cern.ch/record/1517553/>.
- [47] Keith Rehermann and Brock Tweedie. Efficient Identification of Boosted Semileptonic Top Quarks at the LHC. *JHEP*, 1103:059, 2011.
- [48] Pile-up subtraction and suppression for jets in ATLAS. Technical Report ATLAS-CONF-2013-083, CERN, Geneva, Aug 2013.
- [49] Serguei Chatrchyan et al. Measurement of differential top-quark pair production cross sections in pp colisions at $\sqrt{s} = 7 \text{ TeV}$. *Eur.Phys.J.*, C73:2339, 2013.
- [50] Georges Aad et al. Measurement of the top quark pair production cross-section with ATLAS in the single lepton channel. *Phys.Lett.*, B711:244–263, 2012.
- [51] Johann H. Kuhn, A. Scharf, and P. Uwer. Electroweak corrections to top-quark pair production in quark-antiquark annihilation. *Eur.Phys.J.*, C45:139–150, 2006.
- [52] Johann H. Kuhn, A. Scharf, and P. Uwer. Electroweak effects in top-quark pair production at hadron colliders. *Eur.Phys.J.*, C51:37–53, 2007.
- [53] J.H. Khn, A. Scharf, and P. Uwer. Weak Interactions in Top-Quark Pair Production at Hadron Colliders: An Update. 2013.
- [54] Borut Paul Kersevan and Elzbieta Richter-Was. The Monte Carlo event generator AcerMC version 2.0 with interfaces to PYTHIA 6.2 and HERWIG 6.5. 2004.

- [55] Nikolaos Kidonakis. NNLL resummation for s-channel single top quark production. *Phys. Rev.*, D81:054028, 2010.
- [56] Nikolaos Kidonakis. Next-to-next-to-leading-order collinear and soft gluon corrections for t-channel single top quark production. *Phys. Rev.*, D83:091503, 2011.
- [57] Nikolaos Kidonakis. Two-loop soft anomalous dimensions for single top quark associated production with a W- or H-. *Phys. Rev.*, D82:054018, 2010.
- [58] T. Gleisberg et al. Event generation with SHERPA 1.1. *JHEP*, 02:007, 2009.
- [59] Andreas Hocker and Vakhtang Kartvelishvili. SVD approach to data unfolding. *Nucl.Instrum.Meth.*, A372:469–481, 1996.
- [60] G. Aad et al. ATLAS Collaboration. Measurement of $t\bar{t}$ production with a veto on additional central jet activity in pp collisions at $\sqrt{s} = 7$ TeV using the ATLAS detector. *Eur.Phys.J.*, C72:2043, (2012). arXiv:1203.5015 [hep-ex].
- [61] H1 and ZEUS Collaborations. Combined Measurement and QCD Analysis of the Inclusive ep Scattering Cross Sections at HERA. 2009.
- [62] Comparison of Monte Carlo generator predictions for gap fraction and jet multiplicity observables in top-antitop events. Technical Report ATL-PHYS-PUB-2014-005, CERN, Geneva, May 2014.

Appendix A

Electron-jet overlap removal

As described in Section 5 the overlap between the electron and jet collections is done by first subtracting the electron 4-vector from a nearby jet if the jet is within $\Delta R < 0.4$. If the new jet, hereafter referred to as the e -subtracted jet, satisfies the standard jet cuts, then it is used in the analysis to decide whether to accept the electron (if $\Delta R(e, j) < 0.2$, the electron is rejected). If the e -subtracted jet is also the highest p_T jet within $\Delta R(e, j) < 1.5$, then it becomes the b-jet candidate on the leptonic side and its 4-vector is used in the requirement $\Delta R(\text{leptonic side b-jet candidate, selected large-}R\text{ jet}) > 1.5$. For the purpose of jet cleaning and retrieving b-tagging scale factors, the original jet 4-vector is used. In this analysis, the modified jet p_T is *only* used to decide if the jet passes the default jet p_T cut of 25 GeV.

The impact of adopting this procedure is shown in Figure A.1. The efficiency and acceptance as defined in Chapter 9 are shown for the standard fixed cone overlap removal method¹ and the new version discussed here. In the reference particle-level selection used here the electrons are not clustered in the jets and there is no overlap removal. As expected, the efficiency is improved at high top p_T . The lack of any impact at low p_T in the efficiency and over the full p_T range in the acceptance is evidence that the mini-isolation requirement effectively ensures that the subtracted electron does not originate from a heavy flavor decay.

Since the electron and jet collections use different clustering algorithms and different calibrations, there is a concern that the subtraction procedure may result in a biased e -subtracted jet 4-vector. Several checks have been performed to assess whether there are any significant associated systematic effects.

Firstly, the data-simulation agreement for events affected by the procedure is compared to the agreement in unaffected events. Three distributions are shown in Figure A.2:

- Figure A.2 (a) and (b) show the distance between the lepton and leptonic-side

¹In the standard overlap removal, one jet is removed for each selected electron if its centroid is within $\Delta R(e, \text{jet}) < 0.2$, then any electrons with $\Delta R(e, \text{jet}) < 0.4$ to one of the remaining jets are removed.

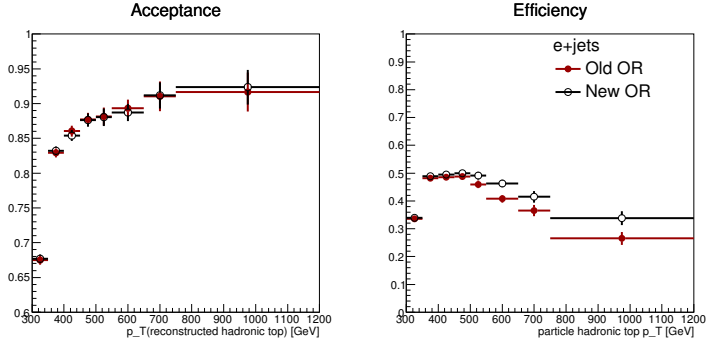


Figure A.1: Comparison between the two versions of electron-jet overlap removal in terms of efficiency and acceptance derived with respect to a particle-level with *no* overlap removal

b-jet candidate. The event selection requires $\Delta R(\text{lepton}, \text{b-jet candidate}) < 1.5$. It can be seen that the e -subtracted jet has a negligible contribution in the vicinity of the cut. Therefore, any bias in the η or ϕ coordinates cannot have a significant impact on the efficiency of this cut.

- Figure A.2 (c) and (d) show the distance between the selected large- R jet and leptonic-side b-jet candidate. Again, any bias in the η or ϕ coordinates cannot have a significant impact on the efficiency of the cut $\Delta R(\text{selected large-}R \text{ jet}, \text{leptonic side b-jet candidate}) > 1.5$.
- Figure A.2 (e) and (f) show the selected large- R jet p_T distribution. A similar agreement is found both categories of events.

In addition, the jet p_T response has been studied in simulation and found to be similar between the e -subtracted and the standard jets. The biggest difference as function of jet p_T is in the 25-50 GeV jet p_T bin where the mean of the response for the e -subtracted jets is lower by $\sim 8\%$ [source unpublished]. The simulation may or may not provide a good description of a similar effect in data and a definitive statement would require an in situ test which is not possible with the presently available statistics. In either case, any effect is limited to the e -subtracted jets that are close to the 25 GeV threshold (p_T is only ever used to decide if a jet is *good*, i.e. above 25 GeV). Such jets form only a small fraction in the boosted top sample as shown in Figure A.3. For example, a 10% shift in p_T may only cause some events in the first bin to fail the 25 GeV cut, i.e. less than 25 events.

To probe the impact of a potential e -subtracted jet p_T mismodeling, the p_T is varied by 2%, 5% and 10%. The relative systematic uncertainty derived from these variations on the reconstructed top p_T spectrum is shown in Figure A.3 and is in all cases within 2%.

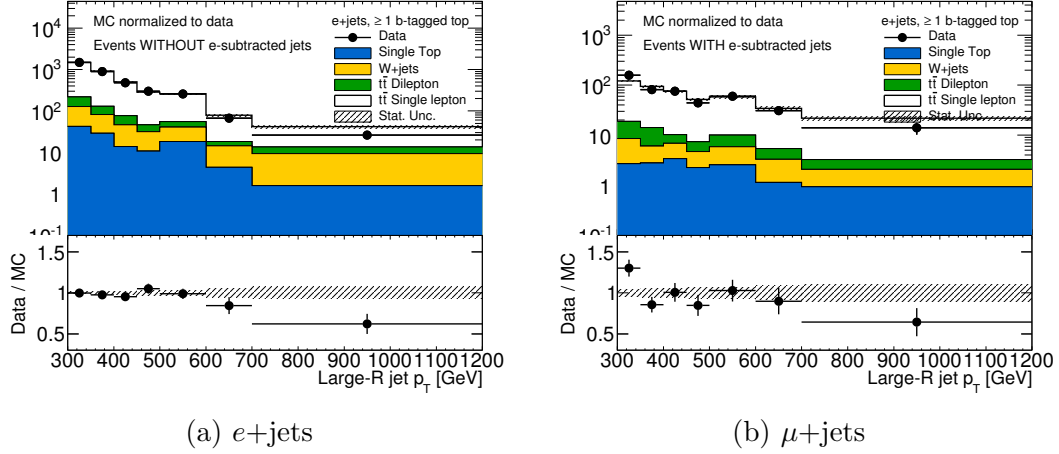


Figure A.2: Comparison between data and simulation for events that are not affected by the subtraction procedure (left) and these that are (right), for the distributions of the distance between the lepton and leptonic-side b -jet candidate (top), the distance between the selected large- R jet and leptonic-side b -jet candidate (middle) and the selected large- R jet p_T (bottom). An overall normalization factor of 0.84 is used in both cases.

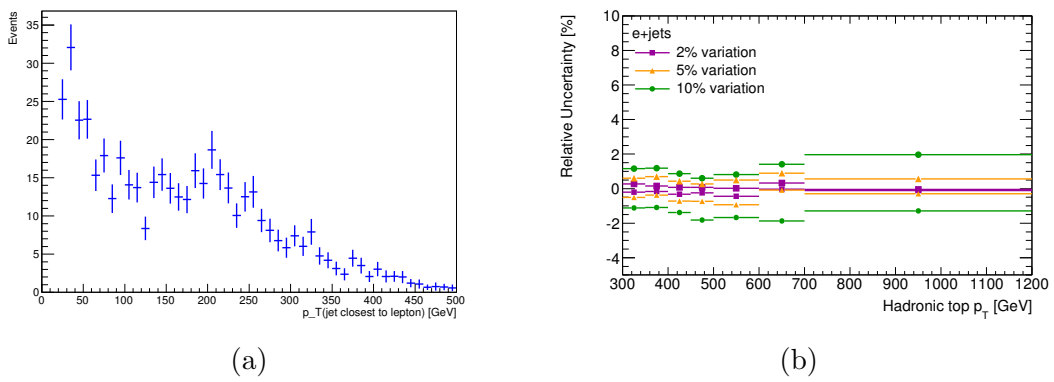


Figure A.3: (a) p_T distribution for the affected jets and (b) relative change in the reconstructed top p_T spectrum corresponding to e -subtracted jet p_T variations of 2%, 5% and 10%.

Variation	MC yield	Data yield	data/MC
- 10%	529	440	0.83
- 5%	543	456	0.84
None	553	464	0.84
+ 5%	570	480	0.84
+ 10%	587	493	0.84

Table A.1: The energy of the e -subtracted is varied simultaneously between data and MC by $\pm 5\%$ and $\pm 10\%$ and the data/MC agreement re-evaluated. Only events affected by the subtraction procedure are considered.

Finally, assuming the e -subtracted jet p_T response is well modeled, it can also be shown that the simulation accurately reflects changes in the selection efficiency due to changes in the jet p_T response. This is done by varying the e -subtracted jet p_T simultaneously in both data and simulation. Table A.1 shows that the yield changes consistently in data and simulation when the jet p_T is varied by 5% and 10%.

In summary, 1) the jet p_T response is found to be similar for the standard and e -subtracted jets, 2) the data-MC agreement for the affected events is similar to that for unaffected events, 3) the relative systematic uncertainty on the top p_T spectrum based on the full difference in jet p_T response between standard and e -subtracted jets (worst case) is flat and within 2% and 4) the 2% would be added to an otherwise $>15\%$ uncertainty. Based on these findings, any potential impact of mismodeling due to the new electron-jet overlap removal is deemed negligible.

Appendix B

Channel-to-channel comparison

The compatibility of the electron and muon channel for several reconstructed-level distributions is tested by plotting the ratios between the e +jets and μ +jets distribution for both data and MC. The ratios are shown for the large- R jet p_T and η , and the lepton p_T in Figure B.1. The error bars include only the statistical uncertainty. The line in the bottom pads is a zeroth degree polynomial with its free parameter fixed at 1 and the statistics box indicates the probability associated with fitting the double ratio with the line.

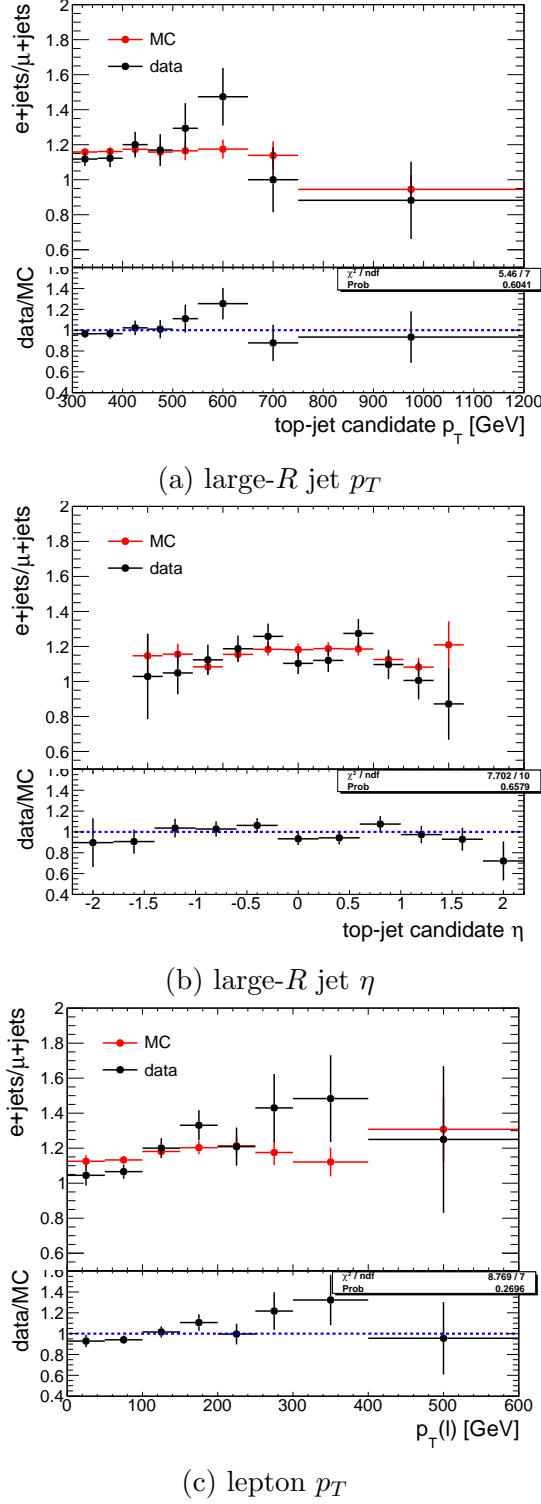


Figure B.1: Ratios between the e +jets and μ +jets reconstructed-level distribution for both data and MC for the large- R jet p_T (a) and η (b), and the lepton p_T (c). Error bars show only statistical uncertainty.